

ABSTRACT

Title of dissertation: CHARACTERIZATION
 OF QUANTUM VORTEX DYNAMICS
 IN SUPERFLUID HELIUM

David P Meichle, Doctor of Philosophy, 2015

Dissertation directed by: Professor Daniel Lathrop
 Department of Physics

Liquid helium obtains superfluid properties when cooled below the Lambda transition temperature of 2.17 K. A superfluid, which is a partial Bose Einstein condensate, has many exotic properties including free flow without friction, and ballistic instead of diffusive heat transport. A superfluid is also uniquely characterized by the presence of quantized vortices, dynamical line-like topological phase defects around which all circulation in the flow is constrained. Two vortices can undergo a violent process called reconnection when they approach, cross, and retract having exchanged tails.

With a numerical examination of a local, linearized solution near reconnection we discovered a dynamically unstable stationary solution to the Gross-Pitaevskii equation, which was relaxed to a fully non-linear solution using imaginary time propagation. This investigation explored vortex reconnection in the context of the changing topology of the order parameter, a complex field governing the superfluid dynamics at zero temperature.

The dynamics of the vortices can be studied experimentally by dispersing tracer particles into a superfluid flow and recording their motions with movie cameras. The pioneering work of Bewley *et al.* provided the first visualization technique using frozen gases to create tracer particles. Using this technique, we experimentally observed for the first time the excitation of helical traveling waves on a vortex core called Kelvin waves. Kelvin waves are thought to be a central mechanism for dissipation in this inviscid fluid, as they provide an efficient cascade mechanism for transferring energy from large to microscopic length scales. We examined the Kelvin waves in detail, and compared their dynamics in fully self-similar non-dimensional coordinates to theoretical predictions.

Additionally, two experimental advances are presented. A newly invented technique for reliably dispersing robust, nanometer-scale fluorescent tracer particles directly into the superfluid is described. A detailed numerical investigation of the particle-vortex interactions provides novel calculations of the force trapping particles on vortices, and a scaling was found suggesting that smaller particles may remain bound to the vortices at much higher speeds than larger particles. Lastly, a new stereographic imaging system has been developed, allowing for the world-first three-dimensional reconstruction of individual particles and vortex filament trajectories. Preliminary data, including the first three-dimensional observation of a vortex reconnection are presented.

CHARACTERIZATION OF QUANTUM VORTEX DYNAMICS IN
SUPERFLUID HELIUM

by

David P Meichle

Dissertation submitted to the Faculty of the Graduate School of the
University of Maryland, College Park in partial fulfillment
of the requirements for the degree of
Doctor of Philosophy
2015

Advisory Committee:
Daniel Lathrop, Chair/Advisor
Christopher Jarzynski
Timothy Koeth
Rajarshi Roy
Stephen Anlage

© Copyright by
David P Meichle
2015

Acknowledgments

First and foremost I would like to thank my adviser Professor Daniel Lathrop. Dan has been a generous, friendly and enthusiastic mentor in so many ways. Dan patiently supported me as I struggled to get through the Quals and first course work, trusting that I would succeed even when I wasn't sure. His "Bricolage Cowboy" attitude has deeply affected me and my thought process in many ways scientifically and otherwise, and I am grateful and honored for the opportunity to be part of his crew.

Dan "Axl" Zimmerman, a dear friend and critical technical and scientific mentor also stands out for his tremendous support and guidance. Axl has glued me together again countless times in all ways scientifically, technically, and personally, and has been a generous and selfless help in everything from debugging electronics to proofreading job applications.

Without the immense technical and administrative support of the staff at IREAP none of this research would be possible. Nolan Ballew played an out-sized role teaching me in the shop and helping design and construct many things for our experiment. Nolan has stayed late and taken efforts beyond the call of duty to help when things were in a crunch and I am sure this project would not have succeeded to any degree it has without his assistance. Don Martin likewise has served generously in all things technical, and helped me move downtown and fix my car. Don graciously brings his new 'grand-fatherhood' to the entire IREAP community. Jay Pyle was always quick to find a tool or offer an idea on how to make or fix something, and

I enjoyed frequently going ice skating with him during lunch hour. Ed Condon was always quick to drop whatever he was doing to help when we had computer or network troubles, and I could not have made progress without his expert and creative computer support. Kathryn Tracey has been a huge assistance, especially when I was running the IREAP Graduate Student Seminar and she reliably took care of all the pizza orders, thank you for that! Dorothea Brosius has been a significant help with my thesis formatting and ran the GSS website, a thankless and important effort. I would like to thank Nancy Boone, whose superhuman efficiency made sure all equipment and supply orders were placed and secured within *minutes*, a service behind the scenes that keeps the wheels rolling for the entire institute. Barbara Brawn-Cinani's administrative, editorial and scientific assistance played a huge part in my graduate career, and she served an essential interface role between Dan and I during some very busy times. After her we are lucky to have Daniel Serrano on board, he has provided excellent editing advice on my thesis and defense talk.

While self-evident, we would not be where we are without my predecessors on the experiment, including Greg Bewley, Matt Paoletti, Kristy Gaff and Enrico Fonda. These 'older siblings' of mine have always been supportive, and have frequently answered questions I had even years after they graduated. It has been an honor to join their line, and fun to get to know them at various conferences though the years. In particular I would like to recognize my close friend Enrico, who initially trained me on the experiment and procedure when I started, and who worked patiently with me in my first hectic semesters of graduate school.

The rest of the Lathrop Lab team have also been extremely gracious in their

help and support. My lab-mate Freja Nordsiek has always been an enthusiastic member of the team who generously would always provide assistance, expert programming and mathematical advice, and is unparalleled in her detailed responses to inquiry on literally any topic. I'd like to thank Santiago Triana, Matt Adams, Doug Stone, Myung Park, Onur Kara, Qin Lui who complete the rest of the team, and whose constant collaboration and expert advice was always helpful and generous.

Peter Megson assumes the role of leading the Helium experiments after my departure; it is a great relief to see the experiment landing in such competent and earnest hands. My mentorship was inconsistent and scattered, falling during a hectic time in my life and a rapidly evolving state of the experiment; Peter is in my debt for not just surviving but thriving during this otherwise turbulent time.

The remaining people from the IREAP community I'd like to thank in particular are Nihal Jhajj and Eric Rosenthal; their continuous and extensive guidance, as well as gracious lending of optics and equipment has been essential for the success of this whole project.

Professor Nick Ouellette was an essential organizing force for the Kelvin wave analysis and preparing that for publication, we were lucky to have him around for a yearlong visit and it was great to get to know him. In addition, Nick and Professor Greg Voth's detailed advice and guidance about designing, aligning, and calibrating stereographic microscopes was instrumental in the success of the project, thank you Nick and Greg for sharing your experience and getting us off on the right track.

I am grateful for the experience to work with and share authorship with Professor Michael E. Fisher on the fixed-point paper. Professor Fisher taught me the

intricacies of properly making figures and refined my scientific writing skills immensely.

Working on the fixed point paper introduced me to Cecilia Rorai, who I enjoyed collaborating with and becoming close friends. I will never forget performing the Beethoven Sonata for Horn and Piano with her both on campus and at a fluid dynamics workshop!

Raffi Schwartz, a close friend helped me immensely getting through the stresses of the final years, and unbeknownst to anyone else ran as co-pilot on an important data run right before Christmas when everyone else was gone and I was too exhausted to run solo. Thank you, Raffi, for all your help and friendship during these years.

Whether a blessing or a curse, I come from a family of scientists: my mother, father, and grandfather are all Ph.D. Physicists, my grandmother is a microbiologist and my other grandfather is a nuclear engineer. It is truly an honor to carry the scientific touch into the third generation. To my father I am grateful that he taught me to constantly ‘think like a physicist’ about all things around me in the world since I was a small child. He also encouraged me to take on projects in model building, hobby electronics and computer programming even as a young kid, and I draw from these practical skills he taught me to this day when working in a lab. My father also was keen to take anything and everything apart, and instilled in me the curiosity to figure out ‘how things work,’ which has been instrumental to my successful lab work.

My gracious grandfather, Dr. Mark Q. Barton, has been hugely influential in

my life. His endless support, and his unspoken yet fair expectation of excellence has been a guiding light for me. Grandpa Barton is a role model who I seek to emulate in all manners of my life.

Lastly, my mother, Professor Linda Barton is truly a keystone in my graduate career success. Whether practical advice on vacuum and pumping systems, sometimes conducted mid-day with back and forth exchange of pictures, or her unwavering emotional support through the difficulties of the Quals and the endless and draining minutia of conducting experiments, I could always count on her to cheer me up and re-instill confidence. Her love and support was complimented and enhanced by her expert technical advice and deep knowledge of the process of research in a truly unique and profoundly important way.

Table of Contents

List of Figures	x
List of Abbreviations	xii
1 Introduction	1
1.1 Background	1
1.1.1 Lambda Transition & Two Fluid Model	1
1.2 Microscopic Model	3
1.2.1 Gross-Pitaevskii Equation	3
1.2.2 Vortex Cores and Circulation Quantization	5
1.2.3 Vortex Reconnection	7
1.3 Macroscopic Model	10
1.3.1 Bio-Savart Filament Model	10
1.3.2 Local Induction Approximation	14
1.4 Motivation for this Thesis	15
2 Gross-Pitaevskii Equation Fixed Point	19
2.1 Introduction	19
2.2 Reconnection & Topology	20
2.3 Initial Condition Preparation	21
2.4 Stationary Solutions	25
2.4.1 Exponential Dynamics Around Reconnection	26
2.5 Higher-Order Stationary Solutions	27
2.6 Conclusion	28
3 Nanoparticle Dispersion	30
3.1 Motivation	30
3.2 Nanoparticle Dispersion	31
3.2.1 Apparatus	31
3.2.2 Experimental Procedure	33
3.3 Nanoparticle Results	37
3.4 Summary	41

4	Particle Vortex Interaction	42
4.1	Introduction	42
4.2	Forces	42
4.3	Particle Trapping in Near Field	44
4.3.1	Maximal Trapping Force	50
4.4	Particle Size Effects	50
4.4.1	Maximal Speed	50
4.4.2	Particle Capture Distance	52
4.4.3	Binding Energy	54
4.4.4	Effect of Gravity	54
5	Kelvin Waves	56
5.1	Introduction	56
5.2	Kelvin Wave Observation	58
5.2.1	Experimental Details	61
5.3	Vortex Filament Models in Similarity Coordinates	62
5.4	Data Compared to Filament Model in Similarity Coordinates	64
5.5	Conclusion	65
6	3D Stereographic Microscope	68
6.1	Introduction & Motivation	68
6.2	Physical Setup	69
6.3	Camera Alignment Procedure	74
6.4	Stereomatching	77
6.4.1	Stereomatching Algorithm	78
6.4.2	Post Processing Track Alignment	80
6.5	Preliminary 3D Results	81
6.5.1	First 3D Reconnection Observation	84
7	Future Objectives	90
7.1	Future Nanoparticle Work	90
7.1.1	Tracer Particle Density	91
7.1.2	Particle Size & Clumping	93
7.1.3	Lifetime in Field of View	94
7.1.4	Comparison to Particle Vortex Calculations	94
7.2	Future 3D Work	95
A	2D Particle Tracking Tutorial	97
A.1	MATLAB Example	105
B	Standard Operation Procedure	106
B.1	Initial Setup	106
B.2	LN2 Pre-cool	106
B.3	Day of Run Preparations	107
B.4	Pre Cool TS with LN2	107

B.5	Liquid Helium Transfer	108
B.6	Cool to Below T_λ	109
B.7	Shutdown Procedure	109
C	Experiment Control Software	111
C.1	Arduino Code	111
C.2	TimeStamp Logger	115
C.3	Temperature Logger	116
C.4	CounterFlow Controller	119
C.5	Bath Temperature	124
D	Circuit Diagrams	125
	Bibliography	127

List of Figures

1.1	Specific heat of liquid Helium near Lambda transition	2
1.2	Superfluid and normal fluid fractions versus temperature	3
1.3	Vortex core in GPE simulation	7
1.4	Order parameter phase around vortex core	8
1.5	Vortex reconnection schematic	9
1.6	Vortex filament-model geometry	12
2.1	Approximate superfluid densities near a vortex core	22
2.2	Sound emission from Fetter approximant	23
2.3	Vortex reconnection fixed point in the GPE	24
2.4	Reconnection eigenvalue versus computational box size	25
2.5	Higher order fixed points of the GPE	29
3.1	Nanoparticle dispersal apparatus	32
3.2	Experimental setup with nanoparticle dispersal apparatus	34
3.3	AFM image of 20 nm fluorospheres on steel	36
3.4	Comparison of frozen gas and fluorescent particles in-situ	39
3.5	Example nanoparticle trajectories	40
4.1	Schematic of particle-vortex calculation configuration	46
4.2	Schematic of trapping force integral setup	46
4.3	Calculated particle trapping force versus distance	49
4.4	Maximal particle trapping force versus particle radius	51
4.5	Capture distance versus normal fluid flow velocity	53
5.1	Kelvin wave emission schematic	57
5.2	Raw image and trajectories following reconnection	59
5.3	Wave-like displacement of particles following reconnection	60
5.4	Collapse of particle trajectories in self-similar coordinates	66
5.5	Evidence of other wave-like trajectories in superfluid	67
6.1	Diagram of 3D camera setup	70
6.2	Technical diagram of 3D setup, side view	72

6.3	Technical diagram of 3D setup, top-down view	73
6.4	Alignment target schematic	74
6.5	Example image of alignment target	75
6.6	Shared particle coordinates versus time between Camera A and Camera C	78
6.7	Track alignment cost function example	81
6.8	Forest of several thousand 3D particle tracks	82
6.9	Example vortex line reconstructed in 3D	83
6.10	Schematic of the first observation of 3D vortex reconnection	85
6.11	3D vortex reconnection, first view	86
6.12	3D vortex reconnection, second view	87
6.13	Separation distance δ versus time for 3D reconnection	88
6.14	Separation distance δ on log-log plot with power-law fit	89
A.1	Pixel value histogram for peakfinding threshold selection	99
A.2	Example of peak-picking for finding approximate particle locations	100
A.3	Example center-of-mass calculation for sub-pixel accurate particle localization	101
A.4	Untracked particle locations throughout movie	104
A.5	Example of tracked particles	104
D.1	Solenoid valve circuit diagram	125
D.2	Control electronics overview	126

List of Abbreviations

AFM	Atomic-Force Microscope
BEC	Bose-Einstein Condensate
GPE	Gross-Pitaevskii Equation
N ₂	Nitrogen Gas
LN ₂	Liquid Nitrogen
OVC	Outer vacuum chamber
TS	Test section
v_s	Superfluid velocity or superflow in m/s
ρ_n	Normal fluid density
ρ_s	Superfluid density
ϕ	Superfluid phase
$\Psi = \sqrt{\rho_s}e^{i\phi}$	Superfluid order parameter
Γ	Circulation in m ² /s
κ	Quantum of Circulation, 9.97×10^{-8} m ² /s in ⁴ He
a_0	Vortex core size (healing length) $\approx .9$ Å
m_{He}	Mass of a Helium-4 Atom
α	Temperature-dependent mutual friction coefficient

Chapter 1: Introduction

1.1 Background

1.1.1 Lambda Transition & Two Fluid Model

Liquid Helium boils at a temperature of about 4.2 Kelvin when at the saturated vapor pressure. Albeit being very cold, and with a very low kinematic viscosity, this liquid is not fundamentally any different than familiar Newtonian liquids including water and air. However, when Helium is cooled below about 2.17 Kelvin it undergoes a second-order phase transition. The transition temperature is called the Lambda point; it is named this way after the observation that the specific heat capacity, shown in Figure 1.1, resembles the shape of the Greek letter Lambda. Surprisingly, the specific heat retains this characteristic shape even when zoomed in by a factor of a million in temperature.

Below the Lambda transition, the Helium can be described as a temperature-dependent mixture of two inter-penetrating components, a normal fluid which resembles a familiar viscous liquid, and a fraction in the superfluid state. The superfluid state is a consequence of the fact that some fraction of the Helium atoms form a Bose-Einstein Condensate (BEC). As shown in Figure 1.2, the relative fraction of

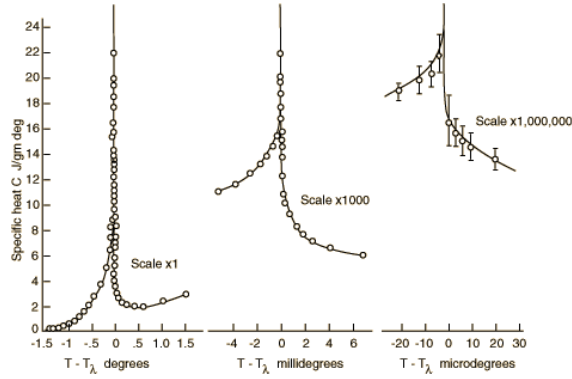


Figure 1.1: Specific heat of liquid Helium near Lambda transition

The onset of superfluidity occurs when liquid Helium is cooled below $T_\lambda = 2.172$ K. At this temperature, the Helium undergoes a second order phase transition, becoming a partial Bose-Einstein condensate. The transition temperature is called the Lambda point, a name given in reference to the shape of the specific heat capacity which resembles the Greek letter Lambda across a wide range of temperature scales. Figure courtesy [2].

Helium in the superfluid state increases as the temperature is lowered toward 0 K.

A superfluid has many interesting and unique properties including flow without friction (viscosity) and ballistic instead of diffusive heat transport. Furthermore, in the superfluid, vorticity in the flow is constrained to line-like mobile vortices, which will be described in more detail in section 1.2.2. These vortices can be nucleated when flow along a boundary exceeds a temperature-dependent critical velocity, or to conserve angular momentum when Helium is rotated. Indeed, the classical fluid analog of solid body rotation in superfluid is a regular lattice of vortices. Vortices may also be nucleated when going through the Lambda transition, as angular momentum is conserved through the phase transition. Various theoretical frameworks for the vortex nucleation and their creation through the Lambda transition, includ-

ing the Kibble-Zurek mechanism [1], are open areas of theoretical and experimental work.

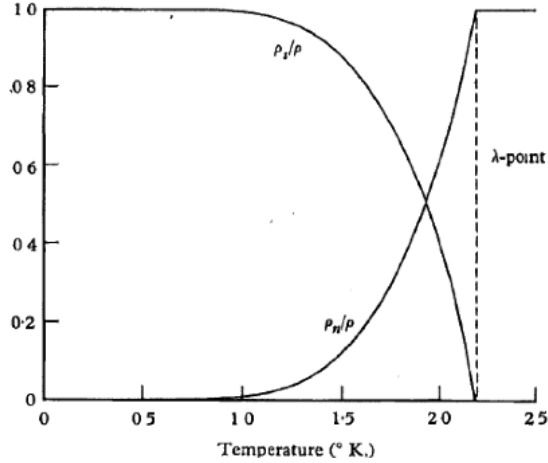


Figure 1.2: Superfluid and normal fluid fractions versus temperature

Below the Lambda transition, the Helium is characterized as a temperature dependent mixture of two inter-penetrating components. The ‘normal fluid’ behaves as a familiar viscous Newtonian liquid, but the superfluid fraction exhibits interesting and unique macroscopic properties. The fraction of the Helium in the superfluid state increases as the Helium is cooled to 0 K. Figure courtesy [3].

1.2 Microscopic Model

1.2.1 Gross-Pitaevskii Equation

A microscopic model is derived from the many-particle Schrödinger equation.

The N-body Schrödinger equation can be written in generic form as

$$i\hbar \frac{\partial}{\partial t} \Psi(\vec{r}, t) = -\frac{\hbar^2}{2m} \nabla^2 \Psi(\vec{r}, t) + \Psi(\vec{r}, t) \int |\Psi(\vec{r}', t)|^2 V(|\vec{r}' - \vec{r}|) d^3\vec{r}', \quad (1.1)$$

where \hbar is the reduced Planck's constant, m is the mass of a ^4He atom, and Ψ is the N-body product wavefunction. We model the repulsive, weakly-interacting inter-boson potential V as a delta-function with strength γ , namely

$$V(\vec{r}' - \vec{r}) = \gamma\delta(\vec{r}' - \vec{r}), \quad (1.2)$$

and a positive chemical potential is given by μ . Together these assumptions let us write a non-linear Schrödinger equation, hereby referred to as the Gross-Pitaevskii equation (GPE), as

$$i\hbar\frac{\partial\Psi}{\partial t} = \left(\frac{-\hbar^2}{2m}\nabla^2 - \mu + \gamma|\Psi|^2 \right) \Psi. \quad (1.3)$$

This equation is characterized by the natural time and space units $\tau_0 = \hbar/\mu \approx .5$ ps and $a_0 = \hbar/\sqrt{2m\mu} \approx .9$ Å. The length a_0 is referred to as the vortex core size, or healing length. Furthermore, taking the substitutions $\partial/\partial\bar{t} = (\hbar/\mu)\partial/\partial t$, $\bar{\nabla} = \hbar/\sqrt{2m\mu}\nabla$, and $\bar{\Psi} = \Psi/\sqrt{m\mu}$, a dimensionless GPE (omitting the overbars for clarity) can be written as

$$i\frac{\partial\Psi}{\partial t} = \left(-\nabla^2 - 1 + |\Psi|^2 \right) \Psi. \quad (1.4)$$

The GPE is widely used as a zero-temperature model of superfluid. It also describes Bose-Einstein condensates, and, more broadly, this complex PDE is found in a variety of pattern formation systems. The GPE governs the time and space evolution of Ψ which is referred to as the order parameter. The magnitude squared of Ψ gives the number density of Helium atoms. The total number of particles is conserved, and given by $N = \int d^3\vec{r} |\Psi(\vec{r})|^2$. This conservative Hamiltonian equation

conserves mass, energy and momentum, and is time-reversal symmetric up to an overall phase shift.

1.2.2 Vortex Cores and Circulation Quantization

In the bulk of the superfluid, the flow is purely irrotational; i.e. the superfluid velocity field, \vec{v}_s , has no vorticity and satisfies $\nabla \times \vec{v}_s = 0$. This is a consequence of the fact that the quantum mechanical probability current \vec{j} is given by

$$\vec{j} = \frac{\hbar}{2mi} (\Psi^* \nabla \Psi - \Psi \nabla \Psi^*), \quad (1.5)$$

where m is the particle mass, \hbar is the reduced Planck constant, and i is the imaginary unit. Inserting the Mandelung transform $\Psi = \sqrt{\rho_s} e^{i\phi}$, where ρ_s is the number density of the superfluid helium component (for density in kg/m^3 we must multiply by the mass of a Helium-4 atom m_{He}), and ϕ is the order parameter's phase. The probability current can be expressed as

$$\vec{j} = \frac{\hbar \rho_s}{m} \nabla \phi. \quad (1.6)$$

This probability current (units of $\text{kg}/(\text{s}\cdot\text{m}^2)$) is the mass flux per unit area. We divide by the superfluid density to obtain the superfluid velocity field (units of m/s), giving

$$\vec{v}_s = \frac{\hbar}{m} \nabla \phi. \quad (1.7)$$

Finally, we can see that the vorticity of the superflow is zero everywhere because the curl of the gradient of any scalar vanishes, i.e.

$$\nabla \times \vec{v}_s = \nabla \times \left(\frac{\hbar}{m} \nabla \phi \right) = 0. \quad (1.8)$$

However, despite the vorticity vanishing in the bulk, the superfluid can have circulation. The following discussion describes how the circulation is quantized and constrained to defects of the order parameter's phase.

In a fluid, the circulation is defined as a closed-path integral of the velocity field, i.e.

$$\Gamma = \oint_C \vec{v} \cdot d\vec{l}. \quad (1.9)$$

We insert the above expression for the superfluid velocity, and also require that the complex field Ψ remain single valued, such that the phase ϕ changes either by zero, or an integer n times 2π when completing a closed path. These conditions require that the circulation is either zero or quantized, which we can see employing the fundamental theorem of calculus

$$\Gamma = \oint_C \vec{v}_s \cdot d\vec{l} = \oint_C \left(\frac{\hbar}{m} \nabla \phi \right) \cdot d\vec{l} = \frac{\hbar}{m} (2\pi)n, \quad n = 0, 1, 2, \dots \quad (1.10)$$

For the case of $n = 1$, we call this feature a *quantum vortex*, and it has uniform circulation of $\kappa := h/m = 9.97 \times 10^{-8} \text{ m}^2/\text{s}$ in ^4He . The circulation κ is referred to as the *quantum of circulation*. The vortices are line-like three dimensional mobile objects; a segment of a vortex filament extracted from a numerical simulation of the GPE is shown in Figure 1.3, and a slice of the order parameter's phase ϕ around a vortex core is shown in Figure 1.4.

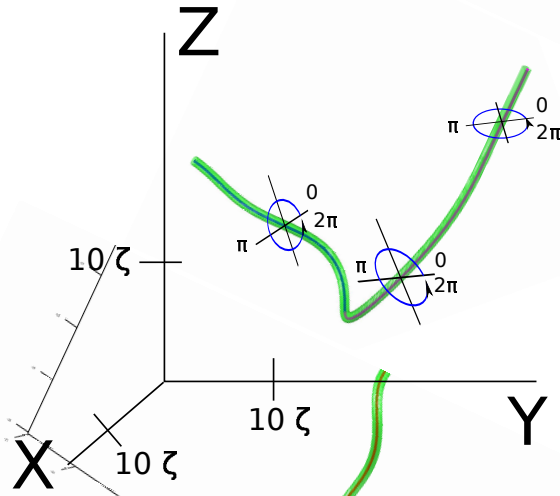


Figure 1.3: Vortex core in GPE simulation

Vortex core filament extracted from a numerical GP simulation. The 2π phase windings are illustrated around the vortex core. GP simulation data courtesy of Cecilia Rorai.

Higher windings (for $n > 1$) are possible and have been observed in BEC systems [4]. However, higher order vortices are energetically unfavorable and unstable to breaking into multiple singly quantized vortices [5]; we expect all our experimental observations are of only singly quantized vortices, and past observations support that assumption.

1.2.3 Vortex Reconnection

A particularly interesting and important event can occur when two vortices approach each other. In many situations, the mutual advection of two vortices will pull them together, as shown schematically in Figure 1.5. They will then intersect and cross, and proceed to violently retract having exchanged tails in a process called

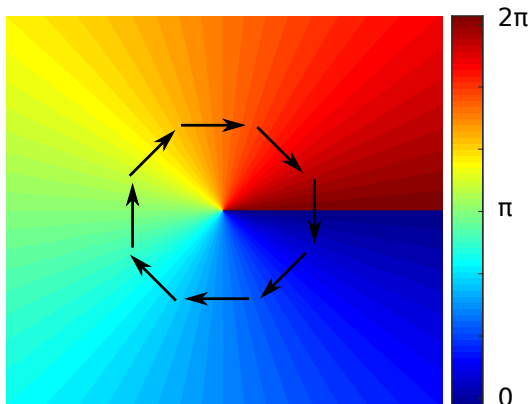


Figure 1.4: Order parameter phase around vortex core

Phase of the order parameter $\Psi = \sqrt{\rho}e^{i\phi}$ around a vortex core, extending out of the page. The arrows indicate qualitatively the superfluid velocity field, given by the gradient of the phase of Ψ . The condition that the phase be single valued enforces a quantization of the circulation around a vortex core. The circulation is $\Gamma = \frac{\hbar}{m}(2\pi n) = \kappa n$ for $n = 0, 1, 2, \dots$. Shown above is the singly quantized case, where $n = 1$. This circulation corresponds to the quantum of circulation $\kappa = 9.97 \times 10^{-8} \text{ m}^2/\text{s}$ for ${}^4\text{He}$.

vortex reconnection. Vortex reconnection also happens in classical fluids (see [7] for a recent 3D visualization of knotted reconnecting vortices in water), but has only recently been directly observed in quantum fluids with the pioneering work of Greg Bewley and Matt Paoletti [8], previously in our group.

Vortex reconnection has important consequences for the dynamics of quantum fluid flows. Reconnection accelerates vortex cores to high speeds and is thought to be responsible for the highly non-Gaussian distribution of velocities measured in driven superflows [9]. The non-Gaussian velocity statistics of superflows constitute a quantitative difference between turbulence in classical fluids of fundamental importance; indeed oral tradition reports that Richard Feynman referred to the

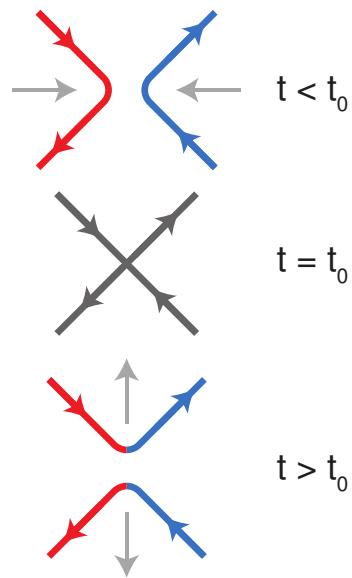


Figure 1.5: Vortex reconnection schematic

Schematic of Vortex Reconnection, courtesy of [6]. Two vortices approach for $t < t_0$ when configured as shown here. The arrows along the vortex core indicate their circulation by the right hand rule. At $t = t_0$ the vortices intersect, after which they retract having exchanged tails. This process, called *vortex reconnection* is of fundamental importance to the dynamics of superfluid flows.

(then only theorized) reconnection of vortices as the ‘defining signature of quantum turbulence.’

Furthermore, vortex reconnection is thought to play a central role in the dissipation of turbulence in quantum fluids. A fundamental question in quantum turbulence is the nature of dissipation in the zero-temperature limit [10] where the effects of friction vanish. The relaxation of a collection of vortices (analogous in some ways to the viscous decay of turbulence in a classical fluid) is observed experimentally even for $T < 0.1\text{K}$ [11]. This relaxation requires a different dissipation mechanism from the viscous classical case; candidates include at least the emission of sound generated by reconnection [12], and the excitation of helical Kelvin waves on the vortex cores [13–18]. Chapter 2 provides a detailed analysis of vortex reconnection in the GPE framework, and Chapter 5 provides the first experimental observation of vortex reconnection exciting Kelvin waves.

1.3 Macroscopic Model

1.3.1 Bio-Savart Filament Model

The quantized circulation around vortex cores can be most easily understood in the quantum-mechanical description, using the complex order parameter Ψ . However, this theory is only relevant to the superfluid component, and the Gross-Pitaevskii equation becomes unmanageable to study numerically at the macroscopic length and time scales accessible by (our) experiment. The numerical difficulty comes from the huge separation of length and time scales of the system; accurate

numerics would require resolving features on the Angstrom-sized vortex core all the way to the several hundred cubic centimeter-sized volume of our cryogenic vessel, along with time resolution from picoseconds all the way to many seconds.

In this section we describe macroscopic filament models for the dynamics of the quantized vortex lines. These phenomenological models include finite-temperature effects, including viscous damping with the normal fluid as a mechanism for the decay of driven superflows and quantum turbulence. However, the filament models do not include the effect of sound emission, kinetic heat transport and thermally driven flows, nor do they naturally exhibit vortex reconnection. Nonetheless, the dynamics of single and interacting forests of vortex lines are often studied with these filament models. We proceed by summarizing the filament theory as described by the pioneering work of Schwarz [19], detailed in the case of vortex reconnection by Lipniacki [20], and presented in the framework of the Frenet-Serret geometry of curves by Guitierrez, Rivas and Vega [21].

The basis for the filament models is the solenoidal nature of the velocity field around a vortex core, analogous to the magnetic field around a current carrying wire. We parametrize the location of the vortex filament in space by $\vec{s}(\xi, t)$, where ξ and t parametrize the curve along arc-length and time, respectively. The velocity field around the vortex core is then given by a Bio-Savart integral,

$$\vec{v}_s(\vec{r}, t) = \frac{\kappa}{4\pi} \int_{\mathcal{L}} \frac{(\vec{s}_1 - \vec{r}) \times d\vec{s}_1}{|\vec{s}_1 - \vec{r}|^3}, \quad (1.11)$$

where \vec{r} is the observation point at time t , and \vec{s}_1 is a specific point along

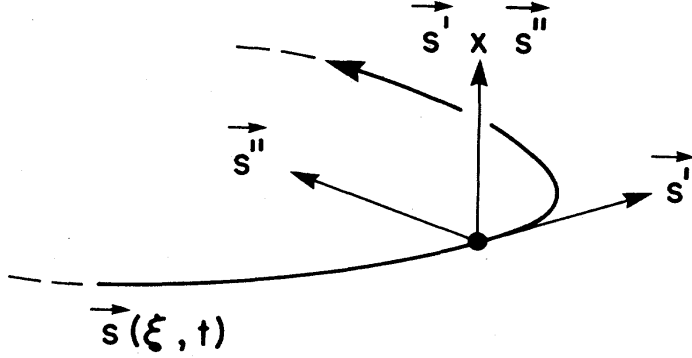


Figure 1.6: Vortex filament-model geometry

The location of a vortex filament is described by the vector $\vec{s}(\xi, t)$, which is parametrized by the arc length ξ at time t . The tangent, normal, and bi-normal vectors are shown, indicated by \vec{s}' , \vec{s}'' , and $\vec{s}' \times \vec{s}''$, respectively, where the prime indicates a vector derivative along the arc-length ξ . This geometry, which is based on the Frenet-Serret frame, is used to describe the superfluid velocity field around a vortex core in a dynamical but phenomenological description of the vortex core dynamics. Figure from [19].

the vortex core confined to the path \mathcal{L} . Note, this integral diverges un-physically as the observation point approaches the vortex line, so it is only valid in the limit $|\vec{s}_1 - \vec{r}| \gg a_0$, where a_0 is the vortex core size of order 1 Å.

As detailed in the above references, this velocity field can be broken into two two terms which dynamically act as a force on a vortex core: a local term related to the self-advection of a vortex line based on its shape and local curvature, and a non-local term which incorporates the effects from other vortices in the vicinity. These two terms combine, as in [19], to describe the time-evolution of a vortex filament by

$$\dot{\vec{s}}_0 = \frac{\kappa}{4\pi} \vec{s}' \times \vec{s}'' \ln \left(\frac{2l}{e^{1/4} a_0} \right) + \frac{\kappa}{4\pi} \int_{\mathcal{L}'} \frac{(\vec{s}_1 - \vec{r}) \times d\vec{s}_1}{|\vec{s}_1 - \vec{r}|^3}. \quad (1.12)$$

Overdots represent time derivatives, primes represent arc-length derivatives

along ξ , and the 0 underscore indicates that we have not yet included viscous damping from the normal fluid. The local radius of curvature is given by l , and the vortex core size is a_0 . The set of lines \mathcal{L}' represent the positions of all other vortices, excluding the local line. We identify \vec{s}' and \vec{s}'' as the normal and binormal vectors in the Frenet-Serret frame, as depicted in the schematic shown in Figure 1.6.

In addition to the local and non-local effects, the filament models include a phenomenological description of the viscous effect provided by the normal fluid component. As stressed in Schwarz [19], the nature of the viscous coupling between the super and normal fluids is not well understood theoretically, however it has been measured in great detail by Hall and Vinen in 1956 with a rotating superfluid experiment [22]. Following the momentum-conservation arguments provided by Schwarz, we add an additional, temperature-dependent kinematic term $\dot{\vec{v}}_f$ to the equation of motion for a vortex line $\dot{\vec{v}}_f$. This term results from a viscous drag force provided by the normal fluid on the core of a vortex, taking the form

$$\dot{\vec{v}}_f = \alpha_1 \vec{s}' \times (\vec{v}_n - \dot{\vec{s}}_0) + \alpha_2 \vec{s}' \times [\vec{s}' \times (\vec{v}_n - \dot{\vec{s}}_0)]. \quad (1.13)$$

The magnitude of the coupling is described by the temperature dependent terms α_1 and α_2 . The local velocity of the normal fluid is given by \vec{v}_n . This additional term $\dot{\vec{v}}_f$ agrees both with historical experimental measurements, and our new experimental work presented in Chapter 5 very well. The magnitude of α_2 has been measured to be approximately three orders of magnitude smaller than α_1 [19], so it is usually set to zero and ignored; we will do the same in the following analysis.

Combining the local and nonlocal terms with the mutual friction term, we have a set of equations to describe the instantaneous motion of a vortex filament given by

$$\dot{\vec{s}} = \dot{\vec{s}}_0 + \alpha_1 \vec{s}' \times (\vec{v} - \dot{\vec{s}}_0) \quad (1.14)$$

$$\dot{\vec{s}}_0 = \frac{\kappa}{4\pi} \vec{s}' \times \vec{s}'' \ln \left(\frac{2l}{e^{1/4} a_0} \right) + \frac{\kappa}{4\pi} \int_{\mathcal{L}'} \frac{(\vec{s}_1 - \vec{r}) \times d\vec{s}_1}{|\vec{s}_1 - \vec{r}|^3}. \quad (1.15)$$

This system of equations constitutes a complete, albeit phenomenological, description of the motion of one or more vortex lines at finite temperature.

1.3.2 Local Induction Approximation

Many studies consider a simplified version of the system of Equations 1.15 referred to as the Local Induction Approximation (LIA), described by Schwarz [19]. The simplification, which allows much more complex, large scale simulations of the physics, comes from the argument that the ratio of the nonlinear terms to the local terms is often very small. When the inter-vortex spacing is much larger than the local radius of curvature, the non-local term can be ignored. Furthermore, the prefactor $\ln \left(\frac{2l}{e^{1/4} a_0} \right)$, can be regarded as a constant of order 10. Here l is the local radius of curvature, which is assumed to be much larger than the Angstrom-scale vortex core size a_0 ; in practice this prefactor term is replaced with a constant, β , which is approximately equal to κ [6, 19, 20].

With these simplifications, the LIA form of the filament model can be written as

$$\dot{\vec{s}} = \beta \vec{s}' \times \vec{s}'' + \alpha_1 \vec{s}'' \quad (1.16)$$

for the case of a locally stationary normal fluid.

Solutions of this model in with dimensionless similarity coordinates are compared to our experimental observations in Chapter 5. Section 5.3 will provide a derivation of LIA expressed in dimensionless self-similar coordinates. Additionally, the newly constructed apparatus described in Chapter 6 is capable of directly comparing the motion of vortex line filaments dynamically in 3D with the LIA and full Bio-Savart models.

1.4 Motivation for this Thesis

This chapter has so far presented a background of superfluid, including a basic development of a microscopic quantum-mechanical model and a macroscopic phenomenological model. Table 1.1 summarizes the differences between the two frameworks.

As we can see, the two frameworks constitute a somewhat scrambled mixture of what relevant physics are contained or omitted. Direct experimental (and numerical) observations are now imperative to vet and constrain the often incomplete and sometimes contradictory predictions made by the theories.

The pioneering work of Greg Bewley, Matt Paoletti and Enrico Fonda in our group provided a method to disperse frozen gas particles into the liquid helium for use as optical tracer particles. This allowed for optical, time-resolved dynamical

Microscopic (GPE)	Macroscopic (LIA)
Quantum Mechanical	Heuristic / Phenomenological
Zero Temperature Only	Finite-Temperature with Mutual Friction
Captures Reconnection Intrinsically	Ad-Hoc Reconnection Only
Time Reversal Symmetric & Conservative	Allows Dissipation
Includes Sound Propagation	Sound Excluded

Table 1.1: Comparison of micro and macroscopic models

Comparison of the microscopic quantum-mechanical model presented in Section 1.2, and the macroscopic model presented in Section 1.3. The two theoretical frameworks separately capture or omit certain aspects of the physics governing the properties of superfluid and the dynamics of the vortices. Development of the new numerical and experimental capabilities presented in this thesis were motivated in large part to test and constrain the various theoretical predictions of these two frameworks.

measurements of the superfluid flow, and for tracking of the vortex cores. This technique allowed for the first direct, unambiguous observations of vortex reconnection, thermally driven counterflow, and measurements of the statistical nature of quantum turbulence.

However, two specific problems remained, which the efforts presented in this thesis address. Firstly, the gas particle technique was notoriously troublesome and finicky. It could not inject particles below the Lambda transition, so experimenters needed to quickly cool before the particles segregated out of the flow which restricted the accessible temperature range. Additionally, the poly-disperse frozen particles were imaged with 90-degree Mie scattered light, a process which is inefficient and leaves only particles larger than about 120 nm visible.

Chapter 3 describes a newly invented apparatus and method for dispersing commercially available, robust and bright fluorescent nanoparticles directly into the superfluid. This technique is also described in our publication [23]. These particles are also very small, which has important consequences for the interaction between the particles and vortices described in Chapter 4.

The second specific problem which this Thesis work addresses is the fact that the dynamics of the vortex lines, reconnection, and the propagation of Kelvin waves are fundamentally three dimensional. Previously, all optical measurements were made in a two dimensional projection. Chapter 5 provides an analysis of experimentally observed Kelvin waves, but in a two dimensional projection. The analysis was confounded by ambiguities due to projection effects. Furthermore, many open questions exist about the three dimensional structure of vortex reconnection, including the distribution of angles between the vortex lines before and after reconnection which would be confounded in two dimensional experimental observations.

Chapter 6 describes a stereographic imaging system which has recently been designed, constructed and debugged. We present the first experimentally measured single-particle trajectories and dynamical reconstructions of the motion of single vortex filaments fully in three dimensions. Additionally, the first observation of vortex reconnection in 3D is presented and characterized in section 6.5.1.

Chapter 7 presents detailed suggestions for future work, both for increasing the utility of the nanoparticle dispersion, and suggestions for interesting experiments to conduct with the new 3D capabilities.

Some of the material in this thesis is derived directly from our publications,

which are referenced throughout the text where appropriate:

- E. Fonda, D.P. Meichle, N.T. Ouellette, S. Hormoz, and D.P. Lathrop. Direct observation of Kelvin waves excited by quantized vortex reconnection. *Proc. Natl. Acad. of Sci. USA*, 111 (Supplement 1):4707-4710, 2014.
- D.P. Meichle, and D.P. Lathrop. Nanoparticle Dispersion in Superfluid Helium. *Rev. Sci. Inst.*, 85:073705, 2014.
- D.P. Meichle, C. Rorai, M.E. Fisher, and D.P. Lathrop. Quantized Vortex Reconnection: Fixed points and initial conditions. *Phys. Rev. B*, 86, 2012.

Chapter 2: Gross-Pitaevskii Equation Fixed Point

2.1 Introduction

This chapter reports a family of fully nonlinear stationary solutions that capture reconnection in the microscopic GPE model of superfluids. This chapter is derived largely from our publication [24], work which was done in close collaboration with Cecilia Rorai, and Professors Daniel Lathrop and Michael E. Fisher.

These stationary solutions (i.e. fixed-points) are in contrast to previous published suggestions of pyramidal structures presented in the context of vortex filament models [25, 26]. They are obtained using imaginary time propagation [27, 28], a well known systematic method for generating low-energy relaxed initial conditions for complex partial differential equations. Many interesting and significant numerical studies have investigated quantized vortex evolution and reconnection [26, 29–36], but have not often explored in detail the role of the initial data. Given the Hamiltonian structure of GPE evolution, and that the 3D equation conserves total energy, momentum, and mass, it is not surprising that initial data are central to the dynamics. This chapter presents evidence of the important role of initial data on vortex evolution. Recent analytical work on the topology of complex fields with connections to the results of previous work on linear models of reconnection [37, 38] and

our fixed points is also discussed.

2.2 Reconnection & Topology

Theoretical studies of complex fields [39, 40] provide generic descriptions and a classification of phase singularities and topology-changing events of which vortex reconnection is but one example. Indeed, distinct categories have been established which have direct analogues in the context of superfluids with a single straight vortex, the reconnection of vortices, and ring propagation, generation, and decay. Specifically, Dennis and Berry [38, 39] have precisely defined the conditions required in a complex field for a topology-changing event to occur. They provide a general Taylor expansion of a complex field Ψ near a topology-changing event, namely

$$\Psi(x, y, z; t) = t + i(az) + \frac{1}{2}\mathbf{r} \cdot \mathbf{A} \cdot \mathbf{r} + O(r^4), \quad (2.1)$$

with a bifurcation on a real time parameter which unfolds the singularity. Here a is a scalar, $\mathbf{r} = (x, y, z)$, and \mathbf{A} is a complex, symmetric 3×3 matrix. They show that if $\det\{\text{Re } \mathbf{A}\} > 0$ the process is elliptical, and analogous to a vortex ring which shrinks and vanishes. If $\det\{\text{Re } \mathbf{A}\} < 0$ the process is hyperbolic, and analogous to a pair of vortices that reconnect. These are the only two stable topology-changing events in complex fields [38, 39], and their analogous physical processes in superfluid ⁴He have both been observed in experiment [41, 42]. This supports the idea that topology-changing events are deeply involved with quantum turbulence decay.

It is worth noting that Equation 2.1 encapsulates our analytic work presented below and the linear aspects of the well-known study of Nazarenko and West [37] on

vortex reconnection. The analysis by Dennis and Berry was executed in the context of optical vortices but is generally applicable to all systems with an evolving complex field; it can be helpful in understanding quantized vortices. Here we focus on the hyperbolic case associated with vortex reconnection.

2.3 Initial Condition Preparation

To prepare minimal-energy initial conditions and to re-examine the straight vortex solution, we employ the diffusive GPE equation (DGPE), with a real diffusivity, written in dimensionless form as

$$\frac{\partial \Psi}{\partial t} = \left(\nabla^2 + 1 - |\Psi|^2 \right) \Psi. \quad (2.2)$$

Notice that a stationary solution of the DGPE is simultaneously a *fixed point* for the GPE. This fact can be exploited to find fixed points of the GPE numerically, and to generate relaxed, minimal-energy initial conditions for dynamical GPE simulations with a specified initial phase profile. The procedure is analogous to the imaginary time propagation method [27, 28] used in Bose-Einstein condensate theory and simulations to study the ground states.

To perform any vortex calculation using the GPE, a vortical initial condition must be specified. An infinite straight vortex is an axisymmetric stationary solution of the GPE that is expressible in cylindrical spatial coordinates as

$$\Psi(r, \phi, z) = f(r)e^{i\phi}, \quad (2.3)$$

where the density profile satisfies $f(r) \rightarrow 0$ when $r \rightarrow 0$, and $f(r) \rightarrow 1$ when $r \rightarrow \infty$. Since there are no exact analytical forms for $f(r)$, it must be found

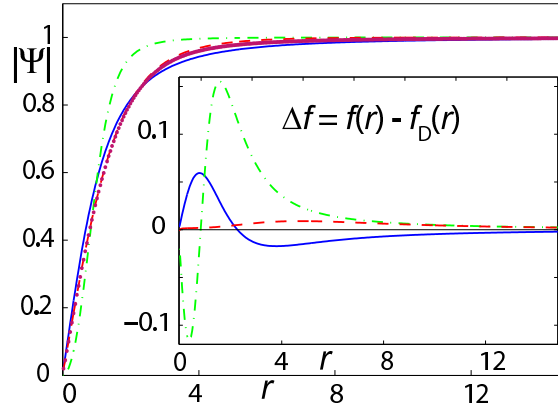


Figure 2.1: Approximate superfluid densities near a vortex core

Comparison of approximate density profiles, $|\Psi| = f(r)$, as introduced by Kerr [36] $f_K^2 = r^4/(2 + r^4)$ (green, dot-dashed), proposed by Fetter [36] $f_F^2 = r^2/(2 + r^2)$ (blue, solid), and developed by Berloff [35] $f_B^2 = 11r^2(12 + r^2)/(384 + 182r^2 + 11r^4)$ (red, dashed), with the diffused and exact profile $f_D(r)$ (pink, dotted). The inset displays the differences, $f_B(r)$ being closest to the exact stationary solution with lowest energy per unit mass. Relative to f_D the excess energies are about 6%, 2%, and 1%, resp.

numerically; but this is not practical when a wavefunction for multiple vortices is required as an initial condition. In previous work, it has been customary to use some convenient analytic but approximate density profile [31, 33, 34, 36], and to multiply such wavefunctions together, one for each vortex, to construct a $\Psi_0 \equiv \Psi(\mathbf{r}, t = 0)$.

We propose a systematic method for generating an initial condition of minimal energy by using the DGPE. First, one generates an approximate *phase profile* $\phi_0(\mathbf{r})$, defined throughout the computational domain, that qualitatively describes the desired initial vortex configuration. Then a corresponding initial wavefunction Ψ_0 with phase factor $e^{i\phi_0(\mathbf{r})}$ is constructed. This is evolved via the DGPE, (Equation 2.2), allowing the magnitude $|\Psi(\mathbf{r}, t)|$ to diffuse, but actively maintaining the same, fixed phase profile, i.e. $\phi_0(t) = \tan^{-1}(\text{Re}\{\Psi_0\}/\text{Im}\{\Psi_0\})$. This process converges to

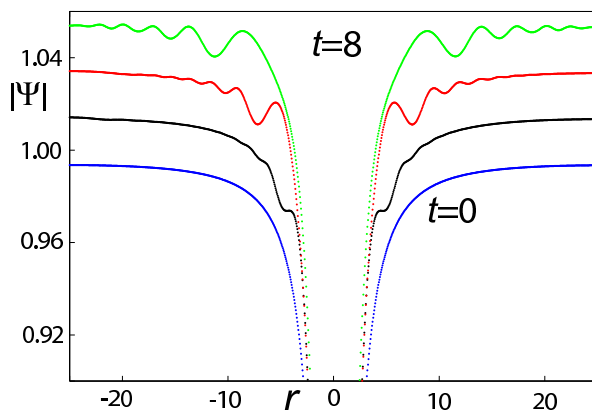


Figure 2.2: Sound emission from Fetter approximant

Time evolution of the Fetter approximant for a single straight stationary vortex according to the GPE integrated in a periodic domain: $f_F = |\Psi|$ is plotted at times $t = 0, 2, 4, 8$ along a midplane section. To reveal the time evolution, successive profiles have been shifted. Evidently, the density profile f_F is not a minimal-energy condition and immediately launches erroneous acoustic waves.

a relaxed solution with minimal energy, and provides reproducible low-energy initial data for a GPE calculation. Note that the Lyapunov functional of the DGPE, which can only decrease or become stationary, is identical to the Hamiltonian for the GPE model. For a single straight vortex along the z -axis, $\Psi_0 = (x + iy)/\sqrt{x^2 + y^2}$ is a sufficient input and converges to the minimal-energy relaxed core density profile. Multiple-vortex initial conditions can be generated by parameterizing the single-vortex phase factors for each desired vortex, multiplying these together, and diffusing as above.

The consequences of using conventional approximate density profiles are dramatic. Figure 2.1 compares three of these analytical forms, namely the Kerr [36], Fetter [36], and Berloff [35] approximants, showing how they differ, some substantially, from the relaxed numerical solution found by first evolving with the DGPE

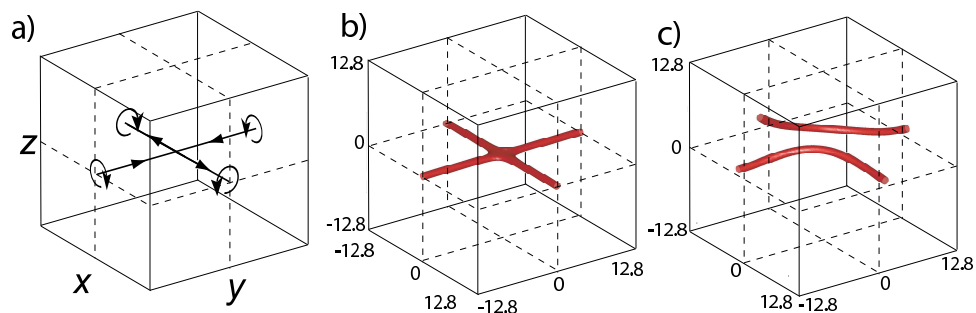


Figure 2.3: Vortex reconnection fixed point in the GPE

The Ψ_4 reconnection fixed point is shown schematically in (a). It consists of four half-infinite coplanar vortices meeting at right angles. Iso-surfaces of the fixed point at $|\Psi_4| = 0.3$ are shown in (b), as obtained via the diffusive GPE. The fixed point is, dynamically, an exponentially unstable saddle that, after a minimal white-noise perturbation in a time-dependent GPE solver, develops with time in a box of size $L = 24.6$ as shown in part (c).

or, equivalently, by numerically solving the relevant radial ODE for $f(r)$ [29]. The Kerr and Fetter approximants launch strong radial waves when imposed as initial conditions for a single straight vortex and evolved in a GPE computation. The emission arises as the inner core region evolves towards the relaxed density profile while the excess energy propagates outwards as waves: see Figure 2.2. This is clearly a mistaken consequence of not specifying minimal-energy initial conditions. (Of course, an interesting feature of the reconnection of vortices is the generation of acoustic waves, etc. [35]) Any of the three approximate profiles can be relaxed to a stable, minimal-energy solution, by first using the DGPE technique.

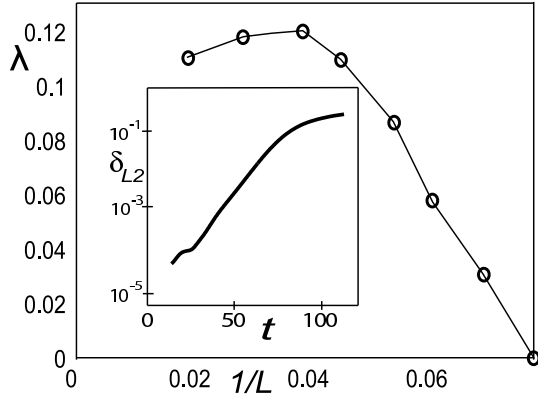


Figure 2.4: Reconnection eigenvalue versus computational box size

The eigenvalue λ of the fixed point Ψ_4 varies with the size of the computational box L . The inset illustrates an exponential L_2 growth after a small perturbation of the fixed point Ψ_4 in a box of size $L = 24.6$.

2.4 Stationary Solutions

Using these same techniques we can find fixed points of the GPE capturing the specific moment of reconnection. The simplest of which we call Ψ_4 , shown schematically in Figure 2.3a. This vortex configuration is poised to reconnect into the 1st and 3rd (x, y) quadrants as in Figure 2.3c or the 2nd and 4th. This bi-stability underlies the saddle nature of the time dynamics near the fixed point.

The local linear structure of this reconnection fixed point is, using an auxiliary length parameter η ,

$$\Psi_4(x, y, z) \approx xy + i(\eta z). \quad (2.4)$$

This determines the phase profile for the four half-infinite vortices shown in Figure 2.3a. We extend this lowest order Taylor series model (a fixed point of the linearized GPE) to a full nonlinear GPE solution by using the DGPE as above. The phase profile implied by Equation 2.4 was held constant in a DGPE solver

until the fully converged fixed-point solution in Figure 2.3b emerges. This was done in an $L \times L \times L$ Cartesian box, using 4th order Runge-Kutta time integration and 2nd order centered finite-differences for the Laplacian operator. The length parameter η was set to $L/2$ which served to produce circular vortex cores. With \hat{n} taken as a unit vector normal to a box wall, we set $(\nabla\Psi) \cdot \hat{n} = 0$ for each wall to enforce no-flux boundary conditions. When relaxing the initial $\Psi(\mathbf{r})$ it proved necessary to enforce all symmetries: thus the functional form in Equation 2.4 satisfies $\text{Re}\{\Psi(x, y, z)\} = -\text{Re}\{\Psi(-x, y, z)\} = \text{Re}\{(-x, -y, z)\}$, etc. To protect from symmetry-breaking instabilities fed by round-off, corresponding values were averaged and reassigned in the box at each time step.

The resulting Ψ_4 fixed point, shown in Figure 2.3b, constitutes a counterexample to a suggested universal reconnection with a fixed 3D pyramidal form [25]; see also [26]. Note Equation 2.4 is a specific example of a hyperbolic phase singularity in a complex field as discussed by Berry and Dennis, where $\det\{\text{Re } \mathbf{A}\} = 0$ [38, 39]. Nazarenko and West [37] also discussed reconnection in hyperbolic configurations: their analysis includes Equation 2.4 as a special case of a family of linear solutions, parametrized by the opening angle between the four half-vortices. Indeed, their perpendicular linearized configuration is likewise stationary.

2.4.1 Exponential Dynamics Around Reconnection

To study the dynamics about our Ψ_4 fixed point, the final DGPE solution was perturbed by white noise of order 10^{-4} at each grid point in the GPE solver,

and evolved in time, yielding configurations as illustrated in Figure 2.3c. The fixed point proves exponentially unstable with a unique, positive, real eigenvalue λ . The L_2 deviation from the fixed point, namely, $\delta_{L_2}(t) = V^{-1} \int_V d^3r |\Psi(t) - \Psi_4|^2$, grows exponentially as $e^{\lambda t}$: see the log-linear inset in Figure 2.4. The eigenvalue λ depends quite strongly on the box size L , measured in terms of the healing length ξ_0 , as seen in Figure 2.4; indeed, quantitatively reliable dynamics requires computational box sizes with $L > 25$.

2.5 Higher-Order Stationary Solutions

Fixed points of the GPE involving straight half-vortices meeting at a point can also be regarded as satisfying a geometric “advection analysis.” Each vortex core generates a solenoidal velocity field, with direction given by the vortex sign, either “inwards” or “outwards.” For a fixed point, the mutual advection of each half-vortex on every other half-vortex must sum to zero. Contemplating these criteria, we have found several other fixed point geometries. Because these higher-order fixed points involve many vortices meeting at a point, they are improbable in real flows of a quantum fluid, unless symmetry constraints are imposed. However, the fixed points are of some interest for small physical systems and, furthermore, they demonstrate the ability to find fixed points of higher order.

We have confirmed numerically that eight coplanar vortices, meeting at an angle of $\pi/4$ with alternating polarities in a cylindrical octagonal computational

box, form a fixed point with a local structure

$$\Psi_8(x, y, z) \approx yx^3 - xy^3 + i(\zeta^3 z). \quad (2.5)$$

The relaxed fixed point found by the DGPE process is shown in Figure 2.5a. Note that Equation 2.4 and Equation 2.5 are members of a likely family of 4, 6, 8, etc., coplanar half-vortices joining at the origin. This family can easily be computed in the linearized version.

Further, as shown in Figure 2.5b, we have found a 3D fixed point that satisfies the advection analysis in a body centered cubic geometry. The local linear structure of this fixed point is

$$\Psi_{8\text{BCC}}(x, y, z) \approx x^2 + y^2 - 2z^2 + i(x^2 + z^2 - 2y^2). \quad (2.6)$$

2.6 Conclusion

We present the identification of a family of phase singularities and topology-changing events permitted in complex fields with direct relevance to vortex reconnection in the GPE. Quantum turbulence decay may be more deeply understood as a relaxation of the topology of the complex order parameter, permitted only through ring decay and vortex reconnection. A method for finding appropriate initial conditions is outlined, with an application to find fixed points of the GPE. A host of reconnection fixed points have been identified numerically, one of which directly counters previous claims of pyramidal vortex reconnection geometry [25, 26].

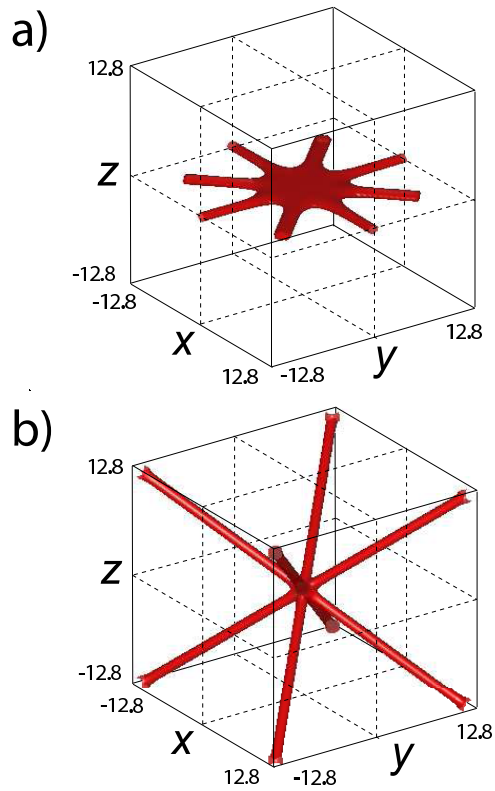


Figure 2.5: Higher order fixed points of the GPE

Two higher-order fixed points found numerically: (a) the planar eight half-vortex form (Equation 2.5) and (b) the three-dimensional body centered cubic form (Equation 2.6). The $|\Psi| = 0.3$ isosurfaces are shown.

Chapter 3: Nanoparticle Dispersion

3.1 Motivation

Experimental techniques to directly observe cryogenic fluid flows open rich new opportunities for scientific exploration. The pioneering work of Bewley et al. [41, 43] provided a method to produce micron-sized frozen (e.g. hydrogen ice) tracer particles in cryogenic liquids allowing for direct, optical measurements of liquid nitrogen and superfluid helium flows. Some fraction of the frozen ice particles become trapped on the quantized vortices in superfluid helium by a Bernoulli pressure gradient, enabling direct study of the vortex dynamics. This technique allowed for the experimental characterization of vortex reconnection [8, 9, 44] predicted by Feynman in 1955 [45]. The two-fluid model of Landau was directly confirmed and the highly non-Gaussian velocity statistics of quantum turbulence were measured in a thermal counterflow [9]. Frozen particle accelerations have also been measured in a thermal counterflow [46, 47]. Recently, we have made the first direct observations of Kelvin waves, helical deformations of a vortex core, observed on a quantized vortex following reconnection [6]. Details of this observation will be presented in Chapter 5. Frozen hydrogen particles have also been used to measure the flow of superfluid helium around a cylinder [48].

While the frozen seed gas technique for creating particles has been scientifically fruitful, there was a need for a more reliable method for dispersing tracer particles in cryogenic fluids, as well as the capability to use fluorescent particles. Very bright fluorescent nanoparticles of a wide range of sizes, emission and absorption wavelengths, and materials are now readily available commercially as they are common in scientific biological, pharmaceutical and medical microscopy applications. Section 3.2 presents a new method for loading and dispersing commercially available fluorescent nanoparticles into cryogenic fluids using ultrasound, section 3.3 discusses results obtained using this apparatus. These two sections are derived largely from our publication [23]. Additionally, section 7.1 discusses some important future directions and summarizes otherwise unpublished attempts already made for further improving the utility of this technique.

3.2 Nanoparticle Dispersion

3.2.1 Apparatus

A schematic of the nanoparticle dispersal apparatus is shown in Figure 3.1, and it is shown attached to a typical optical-access cryostat in Figure 3.2. An ultrasound transducer is attached to an aluminum cone using metal epoxy. The narrow end of the cone is threaded to receive a quarter-inch thin-walled (.010 or .020 in thick) stainless steel tube compatible with standard commercial cryostat vacuum feedthroughs, such as the Swagelock Ultratorr fittings. A stainless steel rod is threaded on one end, and the other is turned down to fit tightly inside the tube

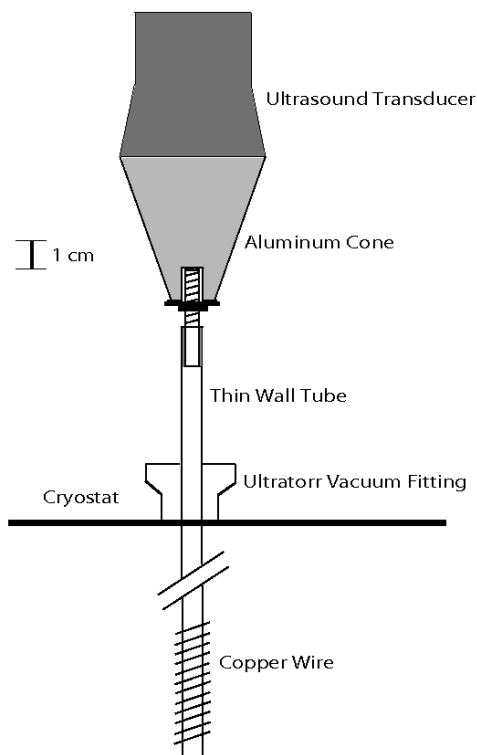


Figure 3.1: Nanoparticle dispersal apparatus

Detailed schematic of a particle dispersal apparatus. An ultrasound transducer is attached to an aluminum cone which receives a thin-walled stainless steel tube compatible with a standard vacuum port feedthrough. A spiral of copper wire is silver soldered to the bottom of the thin-walled tube. Nanoparticles dissolved in de-ionized water are painted onto the bottom of the tube, and the water is evaporated at room temperature. After the sample section of the cryostat is cooled and filled with a cryogenic liquid, activating the transducer for less than one second disperses particles into the sample volume, including directly into the superfluid state of liquid helium.

and silver-soldered inside. The ultrasound transducer is electrically driven with 1.5 kV signal at 45 kHz, with a transducer power of 500 W, only a tiny fraction of which is mechanically transmitted to the cryogen. Both the ultrasound transducer and drive electronics were taken from a commercially available bench-top ultrasound cleaner (McMaster-Carr #32695K38). A copper wire is wound and soldered to the end of tube. This wound wire increases the number of nanoparticles that can be loaded, and assists in applying the nanoparticle solution. This process is described in the section below.

3.2.2 Experimental Procedure

To prepare a sample, the desired quantity of nanoparticles are dissolved into de-ionized water. Acetone should not be used as it was found to destroy the nanoparticles, and solvents such as Isopropyl alcohol are known to bleed the fluorescent dye out of polystyrene particles according to the manufacturer. Applying the nanoparticle solution to the bottom of the tube using a syringe leaves the nanoparticles coated on the tube after the water is allowed to evaporate at room temperature. Acceptable and repeatable particle densities for a 350 mL liquid helium volume were obtained by mixing between 10 μL to 1 mL of the stock 20 nm and 100 nm fluorosphere 2% aqueous solution into 1 mL of de-ionized water. In some experiments, the polystyrene nanoparticles were extracted from the stock aqueous solution (containing surfactants and anti-bacterial agents) by centrifuging at 13k rpm for 10 minutes and extracting the supernatant with a micro-pipette, after which an equiv-

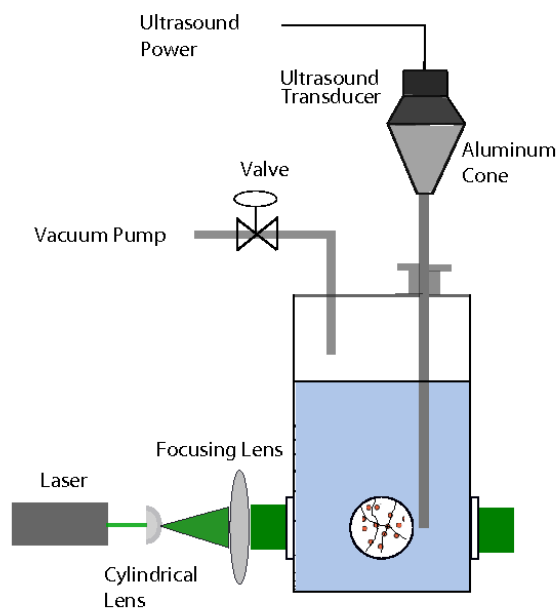


Figure 3.2: Experimental setup with nanoparticle dispersal apparatus
 The particle dispersal apparatus shown connected to a optical-access cryostat. A laser illuminates the cryogenic liquid sample section, in which fluorescent nanoparticles are dispersed allowing for flow visualization.

alent volume of de-ionized water was added. Two to three repeated cycles were necessary to completely remove the unwanted supernatant, which often contained a significant amount of the purple colored fluorescent dye which had leaked out of the polystyrene particles. An initial loading of 200 μL of stock solution produced particle concentrations of order 20 particles per mm^3 in the helium.

Figure 3.3 shows an atomic force microscope image of the 20 nm Life Technologies fluorospheres dispersed on a flat stainless steel surface at room temperature, prepared in the same manner as the dispersal tube is for helium experiments. However, in Figure 3.3 the density of particles per area is about 10 times higher than what is used for helium experiments.

Slowly coating the bottom of the tube over about 20 minutes in several passes allows the excess water to evaporate without dripping off the tube. The tube is then inserted into the cryostat and the transducer is fastened onto the tube outside the cryostat. After these preparation steps, one proceeds to load the cryogenic liquid. Once the end of the tube is submerged in the cryogenic liquid, activating the ultrasound transducer for less than one second is sufficient to disperse the nanoparticles into the sample volume. Precise timing, recording of time stamps, and control of the duration of the sonication are achieved by a Arduino controlled solid state relay which engages the ultrasound amplifier. The Arduino software is in Appendix C, and details of the ultrasound amplifier controller are in Appendix D.

Repeated sonications are effective in both releasing more particles, and stirring settled particles back into the flow. As needed, additional short sonications will redistribute particles into the flow, counteracting the decrease in particle concen-

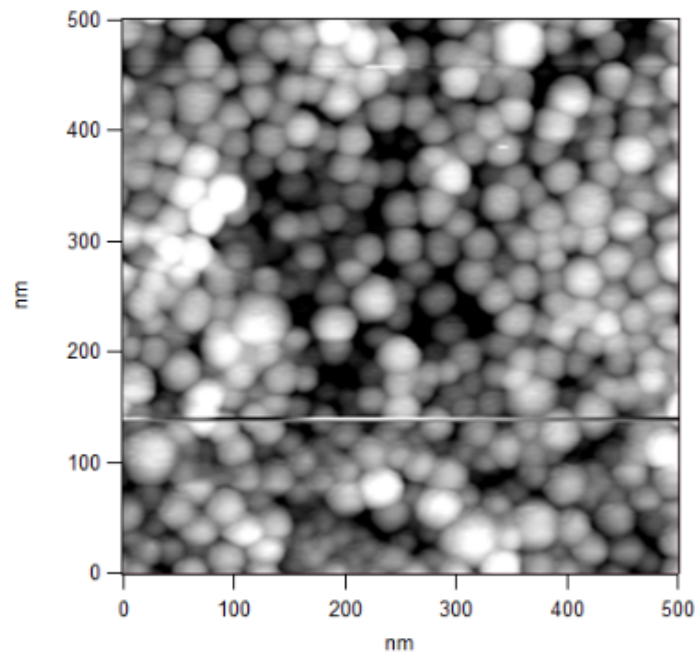


Figure 3.3: AFM image of 20 nm fluorospheres on steel

Atomic force microscope image of 20 nm Life Technologies fluorospheres loaded onto a steel surface. The standard loading procedure for helium experiments was followed, except that the density of particles per area is about 10 times what is normally used. Image courtesy of Joe Garret at IREAP.

tration due to sinking or adsorbing onto the sides of the container. In both liquid nitrogen and superfluid helium, it was possible to take movies for several hours with repeated short sonications (even below the Lambda transition) every five to ten minutes. When sonicating to re-disperse particles, disturbances to the flow can be minimized by attenuating the ultrasound power by inserting a 10 k Ω high-voltage resistor in parallel with the transducer. Without attenuating the power, short sonications lasting about a quarter of a second were found to raise temperature of the helium sample section of order 10 mK, which we estimate corresponds to a heat input of order 5 J.

3.3 Nanoparticle Results

Commercially available semiconductor quantum dots, surface-plasmon resonant gold nanorods, and three sizes of polystyrene plastic beads loaded with fluorescent dyes were tested and successfully imaged in both liquid nitrogen and liquid helium. Table 3.1 lists details about the particles used. A 40 mW 532 nm laser illuminates a thin 10 mm x 10 mm x 175 μm volume through the cryostat windows. Fluorescent light from the particles is passed through a 532 nm notch filter and collected by a 105 mm Nikkor macro-lens with a numerical aperture of about 10 degrees. Movies are recorded with a Princeton Instruments ProEM cooled-CCD camera with 16 μm square pixels, or a low noise high speed VGA CCD camera (ThorLabs part# 340M-GE) with 7.4 μm square pixels.

Figure 3.4a shows 20 nm Life fluorospheres dispersed in superfluid helium at

Particle type	Manufacturer	Part #	Form	Size (nm)	Ex & Em (nm)
Quantum Dots	Ocean Nanotech	QSP600	Pd	5	532 / 602
Gold Nanorods	Nanopartz	E16-532	OS	25x35	533 / 556
FluoroSpheres	Life Technologies	F8784	Aq	20	532 / 575
FluoroSpheres	Life Technologies	F8800	Aq	100	540 / 560
FluoroSpheres	Life Technologies	F8819	Aq	1000	535 / 575

Table 3.1: Particles dispersed in liquid nitrogen and helium
 Details of all particle types successfully dispersed in both liquid helium and nitrogen. Pd, OS and Aq abbreviate powder, organic solvent, and aqueous, respectively, and Ex and Em abbreviate excitation and emission wavelength.

2.094 K. For comparison, a typical image of frozen particles used in the seminal experiments of Bewley and Paoletti is shown in Figure 3.4b. The nanoparticles provide several optical advantages, including a more uniform size and brightness distribution, and better signal to noise as a result of their efficient fluorescence and the ability to filter out the excitation light with a 532 nm optical notch filter. The notch filter allows the imaging optics to isolate the particle’s fluorescent light, removing the excitation light and stray lab light. Filtering could allow for previously difficult optical configurations, where, for example, particles could be imaged flowing around structures in the liquid which would otherwise scatter too much of the illumination/excitation light and saturate the camera.

The frozen particles in Figure 3.4b were illuminated with a 6 W argon continuous laser, whereas the nanoparticles in Figure 3.4a were illuminated with 40 mW from a diode laser. The nanoparticles are relatively brighter, requiring substantially less illumination light. This is important as higher laser powers heat the cryostat windows and generate a thermal counterflow which disturbs the flow.

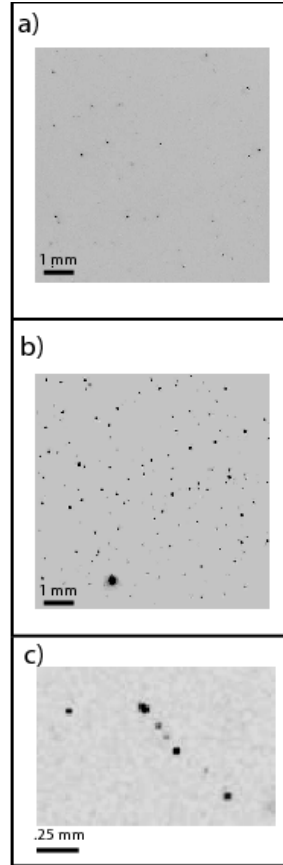


Figure 3.4: Comparison of frozen gas and fluorescent particles in-situ
 a) Contrast enhanced inverted sample image of 20 nm fluorospheres at 1.758 K in liquid helium, with a 30 ms exposure. b) Typical frozen hydrogen particle image from Bewley and Paoletti [9] with a 16 ms exposure. The frozen particle image was taken with a 6 W continuous-wave Argon laser illuminating the particles, whereas the nanoparticle image was taken with a 40 mW 532 nm diode laser. The nanoparticle image shows a more uniform particle brightness distribution, filtering the excitation light significantly reduces the background light level, and there are no large frozen agglomerates which were often present in frozen particle movies. c) A vortex segment decorated with 100 nm fluorospheres at 1.790 K in liquid helium with a 10 ms exposure, demonstrating that the nanoparticles can be trapped on the quantized vortex cores.

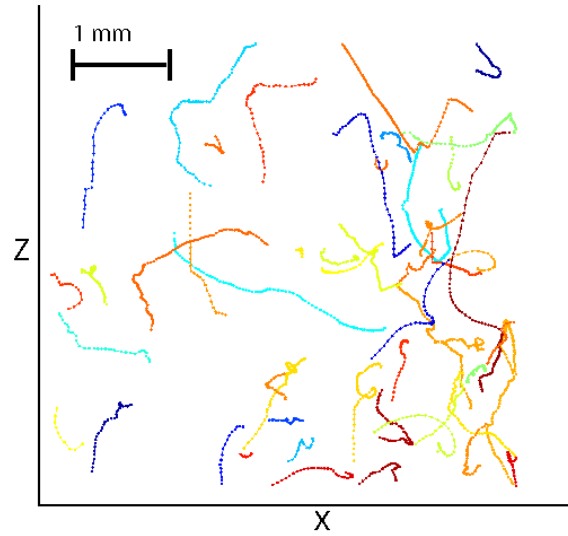


Figure 3.5: Example nanoparticle trajectories

Trajectories of 20 nm fluorospheres at 1.840 K in liquid helium. Each point is separated by 30 ms. Individual particle trajectories are assembled with a particle tracking package [49]. Sudden accelerations and oscillatory motions, likely from vortex core trapping and un-trapping events as well as vortex reconnections are present.

Avoiding the injection of a seed gas prevents the formation of large nonuniform aggregates, which affect the helium and vortex dynamics, and can saturate the imaging system.

Sample particle trajectories of 20 nm Life Technologies fluorospheres in liquid helium at a mean temperature of 1.840 K are shown in Figure 3.5. Each dot represents a nanoparticle location separated by the 30 ms exposure time. These particle locations are assembled into tracks using a standard particle tracking routine [49].

Considering the size and brightness of the particles, and well as the toxicity and special handling required for gold nanoparticles and CdSe, we found the 20 nm and 100 nm Life Technologies fluorospheres to be optimal for superfluid helium

experiments. Safe handling procedures for all nanoparticles and the high voltage ultrasound electronics must be observed.

3.4 Summary

Fluid flows can be measured optically by dispersing faithful tracer particles and recording their motions. However, creating and dispersing robust fluid tracer particles in cryogenic fluids has been notoriously difficult. In this chapter, we have described the apparatus and procedures by which nanometer scale tracer particles can be reliably dispersed into cryogenic fluids and which can readily be applied in measurements with traditional liquid-helium-cooled cryostats. As commercial fluorescent nanoparticles have become widely available, this apparatus opens new possibilities for cryogenic fluid flow metrology, including the techniques of particle image velocimetry or particle tracking.

Chapter 4: Particle Vortex Interaction

4.1 Introduction

The introduction of nanometer scale tracer particles motivated a re-examination of the forces acting on the particles, and a more careful analysis of the effects of particle size on the dynamics relevant to the (new) experimental capabilities. Section 4.2 discusses the relevant forces acting on the particles. A novel and detailed discussion of the particle trapping force in the near-field is presented in section 4.3, where it is found that smaller particles theoretically can be held on vortices moving through a viscous normal fluid at much higher velocities than larger particles. Section 4.4 gives details of how the forces scale with particle size.

4.2 Forces

It is convenient to examine the scaling of the relevant forces and parameters in dimensionless variables. We define the following dimensionless parameters: $\lambda = a/\zeta$ and $\sigma = s/\zeta$, where ζ is the vortex core size, s is the particle's distance from the vortex center, and a is the particle's radius. The core size, near our working temperature of ≈ 1.7 K is $\zeta = \hbar/\sqrt{2m\mu} \approx 1$ Å, where \hbar is the reduced Planck's

constant, m is the mass of a helium atom, and μ is the temperature-dependent chemical potential [24].

The force attracting the nanoparticle to the vortex core is assumed to be the force associated with the gradient of the Bernoulli pressure [43, 50–52]. The Bernoulli pressure outside the vortex core is given by

$$P = -\frac{\rho_s(s; T)\kappa^2}{8\pi^2} \frac{1}{s^2}, \quad (4.1)$$

where ρ_s is the superfluid density, κ is the quantum of circulation, T is the temperature, and s is the radial distance away from the vortex center.

The force acting on the particle is given by the integral over the particle of the gradient of the pressure, or, equivalently, the surface integral of the pressure times the (negative) surface normal component,

$$\mathbf{F}_{\text{trap}} = -\int \nabla P \, d^3V = -\int_{dA} P \hat{\mathbf{n}} \, d^2A. \quad (4.2)$$

The integration domain dA is over the surface of the particle.

The magnitude of \mathbf{F}_{trap} can be approximated in the far-field, for distances far from the vortex core where the gradient of the pressure and the superfluid density are nearly constant. The familiar far-field approximation [43, 50–52] for the magnitude of the attractive force is given by the product of the volume of the particle and the far-field pressure force:

$$F_{\text{trap}} \approx \left(\frac{4}{3}\pi a^3\right) \frac{\rho_s \kappa^2}{8\pi^2} \nabla(1/s^2) = -\left(\frac{\lambda}{\sigma}\right)^3 \frac{\rho_s \kappa^2}{3\pi}. \quad (4.3)$$

However, near the vortex core this approximation is not valid as the vortex may curve [51] and the superfluid density is not constant [24]. A detailed calculation of the trapping force in the near-field will be presented in section 4.3.

In addition to the Bernoulli pressure gradient attracting the particles to the vortex core, we assume that the normal fluid exerts a viscous force (Stokes drag) on the particles [43, 50–52]. The force from Stokes drag is given by

$$\mathbf{F}_{\text{stokes}} = 6\pi a\nu\rho_n(\mathbf{v}_n - \mathbf{v}_p). \quad (4.4)$$

Here a is the nanoparticle’s radius, ρ_n is the normal fluid density, ν is the kinematic viscosity, and $(\mathbf{v}_n - \mathbf{v}_p)$ is the velocity difference between the normal fluid and the particle.

4.3 Particle Trapping in Near Field

As mentioned above, trapping of the particles on the vortex core does not occur in the far-field where the approximation given by Equation 4.3 is valid. Following are novel numerical calculations of the surface integral in Equation 4.2.

An approximate expression for the superfluid density [36] in terms of the dimensionless distance from the core σ is given by

$$\rho_s(\sigma) = \bar{\rho}_s(T) \frac{\sigma}{\sqrt{\sigma^2 + 2}}, \quad (4.5)$$

where $\bar{\rho}_s$ is the temperature-dependent, dimensional density of the superfluid helium component far from the vortex core. This profile approximation is within

a few percent everywhere of an exact numerical calculation we presented in our publication [24], and in Chapter 2. We consider the case of a long straight vortex, its core centered along the z axis and a spherical particle of radius a a distance d away from the vortex core. Figure 4.1 shows a schematic of the physical system, with dimensional variables in part a), and the corresponding dimensionless variables in part b).

We put the trapping force integral in dimensionless form using the dimensionless coordinates λ and σ defined above, and the following substitutions:

$$\begin{aligned}
z/a &\rightarrow \eta & (4.6) \\
R(z) = a \cos\left(\frac{z}{a}\frac{\pi}{2}\right) &\rightarrow r(\eta) = \lambda\zeta \cos\left(\eta\frac{\pi}{2}\right) \\
dz &\rightarrow \lambda\zeta d\eta \\
R(z)d\alpha &\rightarrow \lambda\zeta \cos\left(\eta\frac{\pi}{2}\right)d\alpha \\
1/s^2 &\rightarrow 1/(\sigma\zeta)^2.
\end{aligned}$$

Using Equations 4.1, 4.2, 4.5, and the substitutions in Equation 4.6, the vector trapping force is now given by

$$\begin{aligned}
\mathbf{F}_{\text{trap}} &= - \int_{dA} P \hat{\mathbf{n}} d^2A & (4.7) \\
&= - \frac{\kappa^2 \bar{\rho}_s}{8\pi^2 \zeta^2} \int_{-1}^1 d\eta \lambda \eta \cos\left(\eta\frac{\pi}{2}\right) \int_0^{2\pi} d\alpha R(z) \frac{\sigma}{\sqrt{\sigma^2 + 2}} \frac{1}{\sigma^2} \hat{\mathbf{n}}.
\end{aligned}$$

The angle α indicates the position around the surface of the particle, and s is the scalar distance away from the vortex core of the integration point. We perform

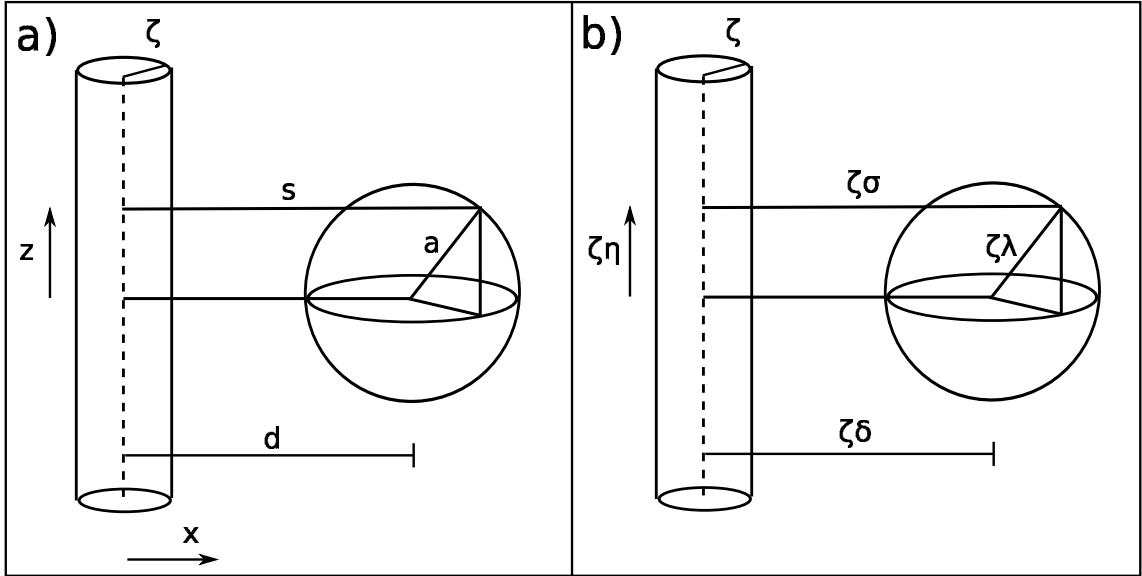


Figure 4.1: Schematic of particle-vortex calculation configuration

Schematic of the physical setup, with a long straight vortex and a spherical particle attracted to the core by a Bernoulli pressure. Part a) shows the dimensional variables used, where ζ is the vortex core size in m. Part b) shows the corresponding dimensionless variables σ , λ , η , and δ .

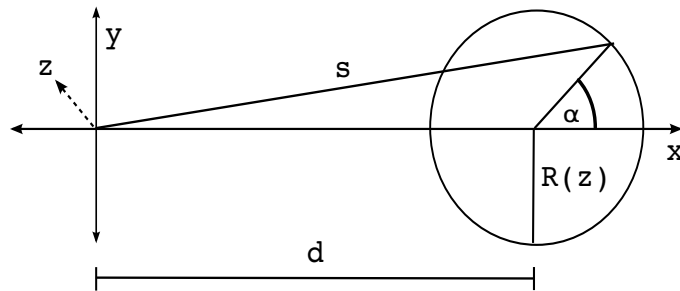


Figure 4.2: Schematic of trapping force integral setup

Schematic of trapping force integral setup, for one infinitesimal slice in z . The particle is treated as a stack of 2D disks with a z -dependent radius. The vortex is assumed to be long and straight, centered at the origin with its core extending in and out of the page along the z axis.

the integral on z last, and consider the particle as a stack of infinitesimal 2D disks with an effective radius of $R(z) = \cos(\pi z/2a)$. The geometry of the integral's setup is shown in Figure 4.2.

Furthermore, we only need to consider the component of the trapping force in the direction pointing toward the vortex core along $-\hat{x}$, as all other components will cancel out. Note that $\hat{n} \cdot \hat{-x} = -\cos(\sin^{-1}(\eta)) \cos \alpha = -\sqrt{1-\eta^2} \cos \alpha$. We can write the x-component of the trapping force in dimensionless variables now as

$$F_x/(\kappa^2 \bar{\rho}_s) = -\frac{\lambda^2}{8\pi^2} \int_{-1}^1 d\eta \cos\left(\frac{\eta\pi}{2}\right) \sqrt{1-\eta^2} \int_0^{2\pi} d\alpha \frac{\cos \alpha}{\sigma \sqrt{\sigma^2 + 2}}. \quad (4.8)$$

Next σ must be expressed in terms of α and η . To do so, consider Cartesian coordinates (x, y, z) centered at the vortex core. For a particle displaced distance d along the x axis away from the vortex core, we have

$$\begin{aligned} x &= R(z) \cos(\alpha) + d \\ y &= R(z) \sin(\alpha). \end{aligned}$$

This allows us to express

$$\begin{aligned} s^2 &= x^2 + y^2 \\ s^2 &= (d + R(z) \cos \alpha)^2 + (R(z) \sin \alpha)^2 \\ s^2 &= R(z)^2 + 2dR(z) \cos \alpha + d^2. \end{aligned}$$

Define $\delta = d/\zeta$ as the dimensionless distance from the center of the particle to the vortex core. Now we can express

$$s = \zeta \sqrt{(\lambda\sigma)^2 \cos^2(\eta\frac{\pi}{2}) + 2\delta\lambda \cos(\eta\frac{\pi}{2}) \cos\alpha + \delta^2} \quad (4.9)$$

$$\sigma = s/\zeta = \sqrt{(\lambda\sigma)^2 \cos^2(\eta\frac{\pi}{2}) + 2\delta\lambda \cos(\eta\frac{\pi}{2}) \cos\alpha + \delta^2}. \quad (4.10)$$

The trapping force integral is now

$$F_x/(\kappa^2 \bar{\rho}_s) = -\frac{\lambda^2}{8\pi^2} \int_{-1}^1 d\eta \int_0^{2\pi} d\alpha \cos\left(\frac{\eta\pi}{2}\right) \sqrt{1-\eta^2} \cos\alpha \left(\sqrt{a(\eta) + b(\eta) \cos\alpha} \sqrt{2 + a(\eta) + b(\eta) \cos\alpha} \right)^{-1}, \quad (4.11)$$

where $a(\eta) = \lambda^2 \cos^2(\eta\frac{\pi}{2}) + \delta^2$ and $b(\eta) = 2\delta\lambda \cos(\eta\frac{\pi}{2})$. While this elliptic integral is intractable analytically - except for $\delta \gg 1$ where the familiar far-field approximation is valid - the force can be computed numerically. Figure 4.3 shows the magnitude of the trapping force computed for a range of particle sizes ranging from about 10 nm to 2 μm . This integral was evaluated using a simple 1st-order Euler integration scheme with 2^{32} points. Sufficient numerical convergence was obtained by doubling the number of grid points until the solution changed by less than .1% at $\delta/\lambda = 1$.

The trapping force agrees, as expected, quantitatively with the far-field approximation for large δ/λ . However, in the near-field, we see a large enhancement of the trapping force. The maximal trapping force occurs when the particle is displaced by its radius away from the vortex core. The large increase in the maximal trapping force has significant consequences for experimental studies, as will be discussed in the next section.

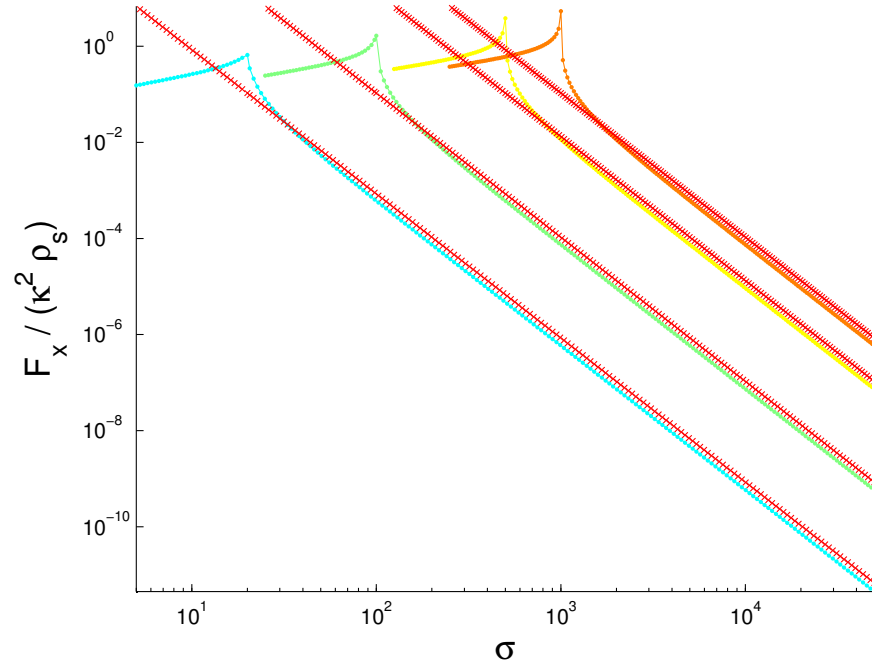


Figure 4.3: Calculated particle trapping force versus distance

Numerical calculation of the particle trapping force on a spherical particle for a long, straight vortex as a function of the dimensionless distance away from the vortex core. Calculations for particles of radius $\lambda = 50, 100, 500, 2500, 5000, 10000$ are shown from left to right. The far-field approximation of Equation 4.3 is shown with the red crosses. Agreement is found between the far-field approximation and numerical calculation for distances far from the vortex core. However, in the near-field where particle trapping actually occurs, the far-field approximation is inaccurate.

4.3.1 Maximal Trapping Force

We expect the maximal trapping force to occur when the particle is displaced one radius from the vortex center, i.e. where $\delta/\lambda \rightarrow 1$. The far-field approximation is constant in the dimensionless particle radius λ when evaluated at $\delta/\lambda = 1$, and invalid because the assumptions made are not true in the particle-trapping regime.

Figure 4.4 shows numerical calculations of the trapping force evaluated at $\delta/\lambda = 1$ where the maximum occurs, for a range of particle radii $\lambda = 20$ to $\lambda = 20000$. This log-log plot appears nearly straight, suggesting that the maximal trapping force is approximated well by a power law of the dimensionless particle radius given by

$$F_x(\lambda; \frac{\delta}{\lambda} = 1)/(\kappa^2 \bar{\rho}_s) = c\lambda^\tau. \quad (4.12)$$

We have fit our numerical calculation to this form and obtained the following values for the dimensionless parameters: $\tau \approx .53$ and $c \approx .14$.

4.4 Particle Size Effects

4.4.1 Maximal Speed

The particle may be dislodged from the vortex when viscous drag from the normal fluid overcomes the force from the attractive Bernoulli pressure gradient. The maximal velocity that a particle can be dragged through the normal fluid while remaining trapped on the vortex core is found by equating the maximal trapping

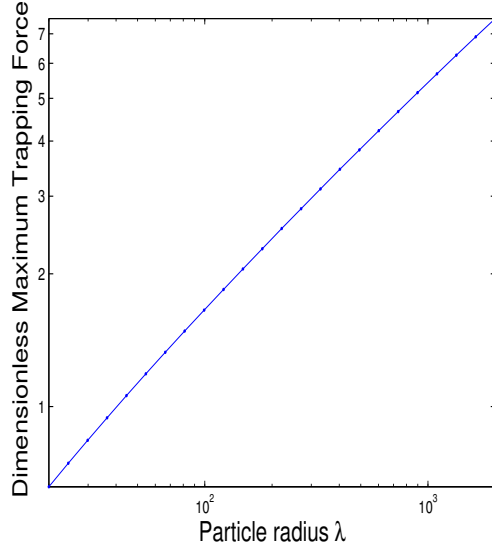


Figure 4.4: Maximal particle trapping force versus particle radius
Dimensionless trapping force $F_x/(\kappa^2 \bar{\rho}_s)$ evaluated at the maximal value where the particle is displaced by its radius from the vortex core, where $\delta/\lambda = 1$.

force and Stokes drag, then solving for the velocity difference between the super and normal fluids. The magnitude of Stokes drag, from Equation 4.4, can be written as

$$F_{\text{stokes}} = 6\pi\zeta\lambda\nu\rho_n v_d, \quad (4.13)$$

using the dimensionless variables stated above and defining the magnitude of the velocity difference between the normal and superfluids $|\mathbf{v}_n - \mathbf{v}_p|$ as v_d . Establishing force balance between the maximal trapping force and Stokes drag we have

$$6\pi\zeta\lambda\nu\rho_n v_d = \kappa^2 \rho_s c \lambda^\tau, \quad (4.14)$$

which we solve for the maximal velocity to find

$$v_d = \frac{\kappa^2}{\nu \zeta} \frac{\rho_s}{\rho_n} \frac{c}{6\pi} \lambda^{(\tau-1)}. \quad (4.15)$$

Note that v_d is approximately proportional to $\lambda^{-1/2}$, which means that the maximum velocity particles can remain trapped is much higher for smaller particles. This result was a primary scientific motivation for the introduction of nanometer scale tracer particles.

The velocity statistics of thermally driven flow in superfluid was measured by Bewley and Paoletti. It was found that the statistics are highly non-Gaussian, establishing a difference between classical and quantum turbulence of fundamental significance. However, with the introduction of nanometer scale particles which can remain trapped at much higher speeds before becoming dislodged from the vortex cores, there is now a new capacity to study the tail of the velocity distributions in more detail. This capacity could also allow for novel studies of vortex reconnection dynamics, as the vortex velocities diverge (limited by the speed of sound) in individual vortex reconnections.

4.4.2 Particle Capture Distance

Since the trapping force is short range, it is important to consider what density of particles per volume is needed to decorate the vortices sufficiently to track their motions. We solve for a capture distance where the pressure field attracting the particle overcomes Stokes drag from the normal component by equating Stokes drag and the far-field attractive force, given by Equation 4.3 and Equation 4.4 and then

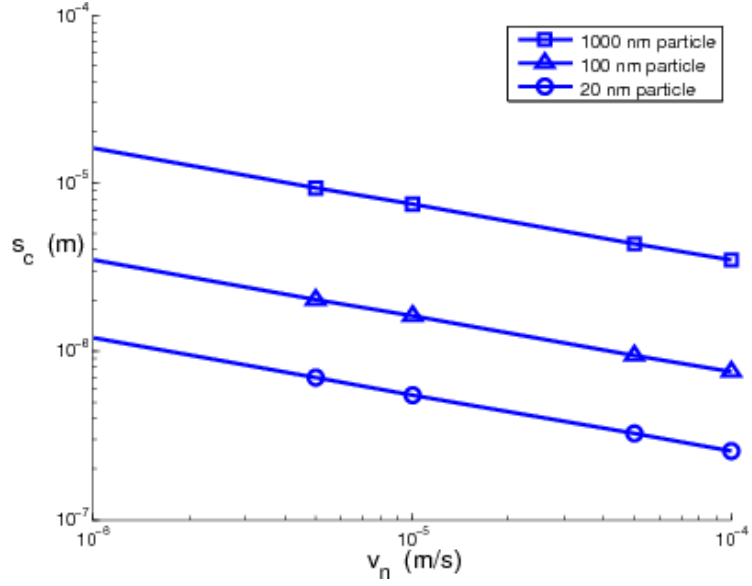


Figure 4.5: Capture distance versus normal fluid flow velocity. Calculated distance s_c below which the trapping force becomes greater than Stokes drag from the normal fluid, as a function of the normal fluid velocity. Three different particle sizes are shown.

solving for s . This gives a capture distance s_c , given by

$$s_c = \left(\frac{\zeta^2 \lambda^2 \rho_s \kappa^2}{18\pi^2 \rho_n \nu} \right)^{1/3}. \quad (4.16)$$

For a 100 nm particle at 1.85 K and a normal fluid velocity of $5 \mu\text{m/s}$, as was measured in [6], this crossover distance is about $20 \mu\text{m}$. Figure 4.5 shows this distance versus normal fluid velocity for three particle sizes. This capture distance is reduced for smaller particles, scaling as $\lambda^{2/3}$, so we expect higher seeding densities (particles per volume) are required to decorate vortices than with frozen particles. Figure 4.5 shows the capture distance as a function of typical background normal fluid velocities for three particle sizes.

4.4.3 Binding Energy

We estimate the binding energy of a nanoparticle by computing the excluded superfluid kinetic energy, as in Parks and Donnelly [55] and Bewley [56]. For a 100 nm particle at 1.85 K, the binding energy is estimated to be about 5×10^{-20} J, which is 1.5×10^3 times $k_b T$, where k_b is Boltzmann's constant and T is the temperature. The binding energy calculated by Parks and Donnelly scales approximately linearly in particle radius for $\lambda > 1$, which is true for the particles used in our experiments. Since the binding energy is many times $k_b T$ even for the smallest particles, we expect particles to remain trapped and not removed due to purely thermal motions. For an detailed calculation of the particle binding and vortex core size see the recent work by Williams [57].

4.4.4 Effect of Gravity

The tracer particles have a greater density than Helium, so gravity and buoyancy effects are also present. The downward gravitational force for a spherical particle with buoyancy is given by

$$F_g = (\rho_p - \rho_s)g\frac{4}{3}\pi a^3, \quad (4.17)$$

where ρ_p is the density of the particle, and ρ_f is the total (super and normal fluid needed to account for mass displacement) density of helium, and g is the gravitational acceleration $g \approx 9.81$ m²/s. For helium in our working temperature range of 1.6 to 2.17 K, the total density is about 150 kg/m³, and the density of

polystyrene is about 1000 kg/m^3 . A free-fall speed can be found by balancing the gravitational force with Stokes drag from the normal fluid [58]. The free-fall speed is

$$v_f = \frac{2(\rho_p - \rho_f)ga^2}{9\rho_n\nu}. \quad (4.18)$$

For a 100 nm polystyrene sphere, the terminal free fall speed is about $1 \text{ }\mu\text{m/s}$, and for a 20 nm sphere the free fall speed is about 50 nm/s ; these free fall speeds are insignificant for current vortex dynamics studies, but could become relevant for larger particles especially at lower temperatures.

Chapter 5: Kelvin Waves

5.1 Introduction

The reconnection of quantized vortices and subsequent emission of Kelvin waves along the vortices are thought to be central to dissipation in such systems. By visualizing the motion of sub-micron particles dispersed in superfluid helium, we have directly observed for the first time the emission of Kelvin waves from quantized vortex reconnection. We characterize one event in detail, using dimensionless similarity coordinates, and compare with several theories. Finally, we give evidence for other examples of wavelike behavior in our system.

The contents of this chapter are derived in large part from our publication [6]. This work was done in close collaboration with Enrico Fonda, and under the additional guidance of visiting professor Nick Ouellette. We are grateful for the calculation of the Biot-Savart model in similarity coordinates provided by Sahand Hormoz, shown in Figure 5.4.

In his pioneering work [59], Kelvin showed that a helical deformation of a line vortex propagates as a wave. Kelvin waves have long been used to understand a wide range of flow problems, such as airplane wakes [60], tornadoes [61], and the dynamics of neutron stars [62]. Kelvin waves are also conceptually related to whistler waves

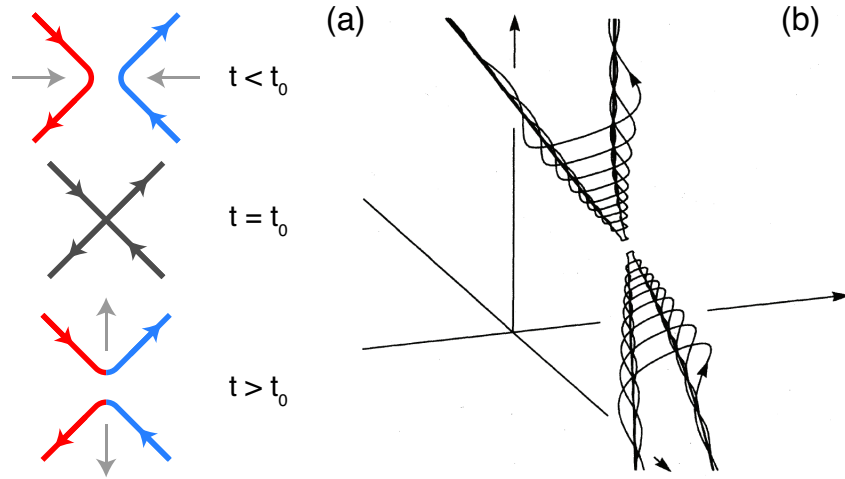


Figure 5.1: Kelvin wave emission schematic

(a) Schematic diagram of two vortices reconnecting and exchanging tails, where the red and blue arrows represent the direction of vorticity. (b) After reconnection, the relaxation of the vortex excites Kelvin waves thought to propagate in a self-similar manner. Part a) courtesy [6], part b) from Figure 18 in [19].

in plasmas [63].

Theory and simulations indicate that a cascade of Kelvin waves transfers energy from large length scales (the inter-vortex spacing) to small scales (the vortex-core size) [13–15], where energy is removed from the system via phonon emission [16–18]. This transfer of energy across length scales is an important mechanism involved in the dissipation of turbulence in quantum fluids.

Kelvin waves have only been visualized in classical fluids on thin line vortices [64,65] and on knotted vortex rings [66]. Here we present the first direct observation of Kelvin waves on quantized vortices, and give the first experimental evidence of the emission of Kelvin waves after vortex reconnection. Since our fluid is inviscid and the amplitude H of the waves we observe is much larger than the vortex core

size a_0 (we have $H/a_0 > 10^5$), our system satisfies most of the assumptions originally made by Kelvin for his eponymous waves.

Kelvin waves on quantized vortices were first detected indirectly using torsional oscillators [67, 68], beginning with the work of Hall in 1958 [69]. However, the interpretation of such experiments has been criticized [70]; additional evidence is therefore needed [67]. Ashton and Glaberson [71] measured the velocity of ions passing through the superfluid as a function of an applied electric field, and found an anomaly that they associated with the resonant generation of vortex waves. A recent experiment [72] inferred the presence of Kelvin modes in a Bose-Einstein condensate by the examining the damping. However, to our knowledge, no direct observation has shown the existence of Kelvin waves on quantized vortices, and no experimental evidence has shown Kelvin waves launched from vortex reconnection.

5.2 Kelvin Wave Observation

Using a technique pioneered by Bewley *et al.* [73] to create sub-micron frozen tracer particles, at a mean temperature of 1.981 K we slowly cooled at a rate of 0.2 mK/s, and observed a long, clearly decorated vortex. In contrast to the technique of Bewley, these particles were frozen atmospheric ice, not pure hydrogen.

In Figure 5.2a, we show several snapshots in a 2.08×0.4 mm² sub-region of our measurement area, with the tracer particles used for further analysis indicated. In multiple frames, captured at 54.3 Hz, several sections of the vortex were visible over a length of about 3 mm, appearing initially straight and nearly horizontal. The

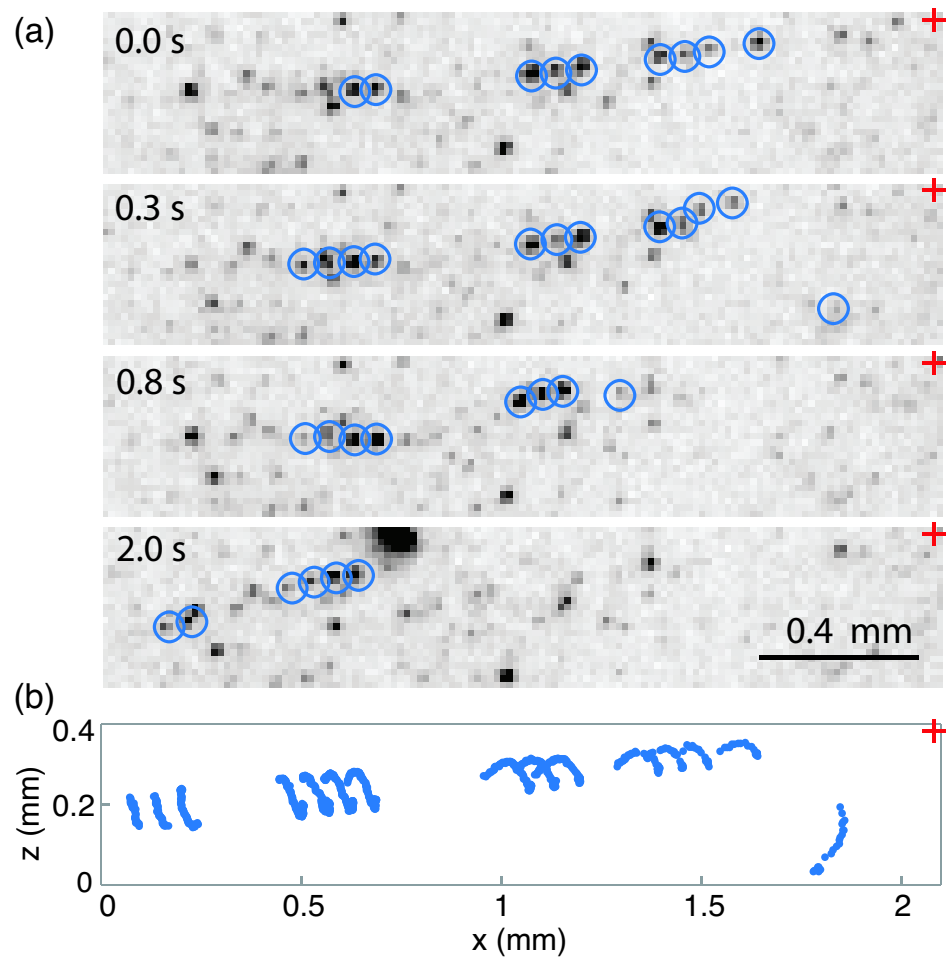


Figure 5.2: Raw image and trajectories following reconnection

(a) Four frames of our movie sequence along with circled particles used in the tracking analysis. (b) The positions of the particle tracks on the upper branch show oscillatory behavior after the reconnection event. The cross indicates the estimated location of the reconnection event.

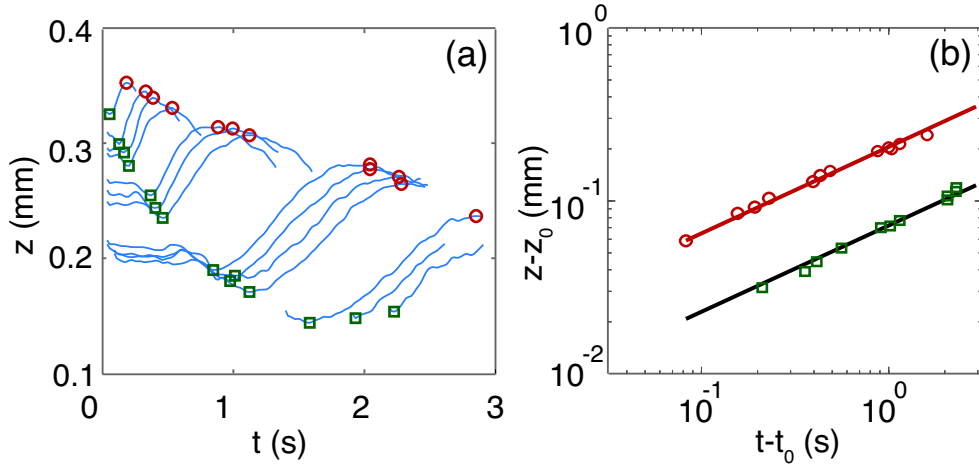


Figure 5.3: Wave-like displacement of particles following reconnection
(a) The vertical position of the particle tracks on the upper branch show marked oscillatory behavior just after the observed reconnection. (b) The observed maxima and minima of the vertical positions from (a). These are consistent with the expected behavior for spatial scales close to a reconnection event $(z - z_0) \sim (t - t_0)^{1/2}$.

normal component of the Helium was almost stationary, with particles dragged in different directions at a maximum velocity of $6 \mu\text{m/s}$.

The vortices we observed are longer (up to several millimeters) and straighter than those from previous studies, because the system was in the superfluid state for about half an hour before measuring. In contrast, the system studied by Paoletti *et al.* [9, 74] was driven strongly out of equilibrium by a thermal counterflow and had a dense tangle of vortices in a larger 5 cm diameter volume.

Shortly before the snapshots in Figure 5.2a, the vortex shown reconnected with another vortex to the right of the field of view. Immediately after the reconnection, we observed a wave propagating down the vortex.

5.2.1 Experimental Details

Our experimental setup consists of an Oxford Instruments STX cryostat with five optical windows. The helium sample section has a $1\text{ cm} \times 1\text{ cm} \times 7.5\text{ cm}$ rectangular glass cell with 1 mm thick walls, immersed in a 5 cm diameter cylindrical bath. The system is illuminated with a 3 mW 532 nm laser, which is focused into a sheet about $175\text{ }\mu\text{m}$ wide and 5 mm tall. The square area is imaged using a 105 mm Micro-Nikkor lens. A Princeton Instrument Pro-EM CCD movie camera provides single-photon sensitivity with a 512×512 pixel resolution.

To study the wave motion quantitatively, we track the position of the particles on the vortex, see Figure 5.3b. The wave-like motion of the vortex is clearly visible in the time evolution of the vertical positions of the particles, plotted in Figure 5.3a. A movie is available in the supplementary materials of our publication [6]. The first peak and trough are clearly visible in most of the tracks, with secondary peaks only in some. We fit the time evolution of the maximum and minimum z values of each particle, indicated respectively by circles and squares in Figure 5.3a, and found $(t - t_0)^{1/2}$ scaling for both, as shown in Figure 5.3b. This is consistent with previous theoretical and experimental studies of reconnection [9, 25, 37, 75, 76], with the assumption that the quantum of circulation $\kappa = h/m_{He} \simeq 9.97 \times 10^{-8}\text{ m}^2/\text{s}$ is the only relevant dimensional parameter, and with the dispersion relation $\omega(k) \propto \kappa k^2$ for Kelvin waves of frequency ω and wavenumber k [77].

5.3 Vortex Filament Models in Similarity Coordinates

In theoretical vortex-filament models, the velocity of the superfluid is calculated from the position of the vortices $\mathbf{s}(\sigma, t)$, where σ is the arc length along the vortex, using the Biot–Savart integral. Schwarz [19] laid the foundation for studying vortices after reconnection, using the so-called local induction approximation (LIA) [78]. This approximation truncates the Biot–Savart integral by neglecting nonlocal terms, reducing it to a much more tractable form¹. We recall from Section 1.3.2 that the local induction approximation (LIA) implies

$$\frac{\partial \mathbf{s}}{\partial t} \simeq \beta \frac{\partial \mathbf{s}}{\partial \sigma} \times \frac{\partial^2 \mathbf{s}}{\partial \sigma^2}, \quad (5.1)$$

where $\beta \simeq \kappa$. We neglect logarithmic corrections that depend on the radius of curvature of the vortex and the core size, absorbing them into the constant parameter β . This equation has self-similar solutions for the evolution of the vortex shapes after reconnection [21, 75] and predicts emission of Kelvin waves² as an inevitable consequence of the relaxation of any angle-like configuration [10].

Define the dimensionless similarity coordinate $\eta = \sigma/\sqrt{\beta t}$. Substituting a self-similar solution of the form $s(\sigma, t) = \sqrt{\beta t} \mathbf{G}(\eta)$ into the LIA gives

$$\frac{1}{2} \mathbf{G} - \frac{1}{2} \eta \mathbf{G}' = \mathbf{G}' \times \mathbf{G}'', \quad (5.2)$$

¹ We note that this approximation has in fact been rediscovered several times [79] since the original work of Da Rios in 1906 [80].

² Note that waves excited by the relaxation of a cusp are localized and polychromatic unlike, for example, the periodic waves artificially excited on straight vortices in recent numerical studies of the Kelvin wave cascade [81, 82].

where the primes denote differentiation with respect to η . However, solutions to this simple equation cannot exactly describe our system, which is at finite temperature. Coupling between the superfluid and the residual normal component via the mutual friction must be included. Therefore, we consider a modified LIA equation with a phenomenological temperature-dependent damping term $\alpha(T)\partial^2\mathbf{s}/\partial\sigma^2$, as done by Schwarz [19] and Lipniacki [75]. After the substitution used to obtain Equation 5.2, the addition of this damping term results in

$$\frac{1}{2}\mathbf{G} - \frac{1}{2}\eta\mathbf{G}' = \mathbf{G}' \times \mathbf{G}'' + \alpha(T)\mathbf{G}''.$$
 (5.3)

Solutions to Equation 5.3 are a two-parameter family of curves that can be completely specified by the temperature-dependent damping term $\alpha(T)$ and the initial curvature c_0 , which determines, via integration of Equation 5.3, the opening angle between the two tails of the retracting vortex line (see Figure 5.1b for an illustration). Note that $c_0 = A/4$, where A is the dimensionless pre-factor of the scaling law of the inter-filament separation distance, that we experimentally estimate to be $A \simeq 3.3$ from fitting $(z - z_0) = A(t - t_0)^{1/2}$; this estimate provides a lower bound for A . Based on our temperature and previous measurements of the mutual friction coefficient [83], we estimate $\alpha = 0.27$.

In addition to the LIA model, we consider novel similarity solutions of a Biot–Savart model similar to that described by Hormoz and Brenner [84] but modified to include the damping term, which leads to an equation analogous to Equation 5.3:

$$\frac{1}{2}\mathbf{G} - \frac{1}{2}\eta\mathbf{G}' = \mathbf{G}' \times \mathbf{G}'' + \alpha\mathbf{G}'' + F[\mathbf{G}]. \quad (5.4)$$

The additional term $F[\mathbf{G}]$ approximates non-local contributions to the velocity of the filament. We solve Equation 5.4 using coupled-delay differential equations to incorporate the non-local interactions (numerical calculation courtesy of Sahand Hormoz). As with LIA, the solutions are a two-parameter family of curves characterized by the pre-factor A and the temperature dependent constant α .

5.4 Data Compared to Filament Model in Similarity Coordinates

Following the theoretical prediction that the evolution of the vortex shape is self-similar, we define the similarity coordinates $\zeta = (z - z_0)/\sqrt{\kappa(t - t_0)}$ and $\eta = (x - x_0)/\sqrt{\kappa(t - t_0)}$. This self-similar assumption is reasonable given the $(t - t_0)^{1/2}$ scaling of the wave peak, as shown in Figure 5.3. We estimate the spatiotemporal coordinates of the reconnection event (x_0, z_0, t_0) ; those values are adjusted to collapse the tracks. As shown in Figure 5.4, the trajectories of the individual particles on the vortex collapse well when rescaled into these similarity coordinates.

Figure 5.4 shows a comparison of the Biot–Savart and LIA curves, with our data rescaled in the dimensionless similarity coordinates η and ζ . These numerically integrated curves were computed in 3D and rotated to optimize the fit of their projection onto the 2D data. For a dense tangle, the results of LIA are distinctively different from the full Biot-Savart [85] calculation. However, for the vortex density in our system and the resolution of our particle tracks, the two models compare

equally well to our similarity-collapsed experimental data.

Although we have focused here on one event, we observed many other tracks with wave-like motions. Some tracks of particles moving in wavy and quasi-circular motion are reported in Figure 5.5. Note that a particle trapped on a vortex would appear to move in a circle if observed in a plane normal to the axis of propagation for a helical Kelvin wave. In general, however, care must be taken in interpreting the motion of the particles on a vortex, as the particles are not locked to a specific point along the vortex core.

5.5 Conclusion

Using sub-micron ice particles, we have observed the emission and propagation of Kelvin waves on quantized vortices in superfluid helium following vortex reconnection. The resulting waveforms are in general agreement with theoretical similarity theories. These waves carry energy away from the reconnection event, and enhance dissipation through mutual friction. Future studies could examine a broader collection of events to characterize the distribution of amplitudes and phase velocities present in quantum turbulence.

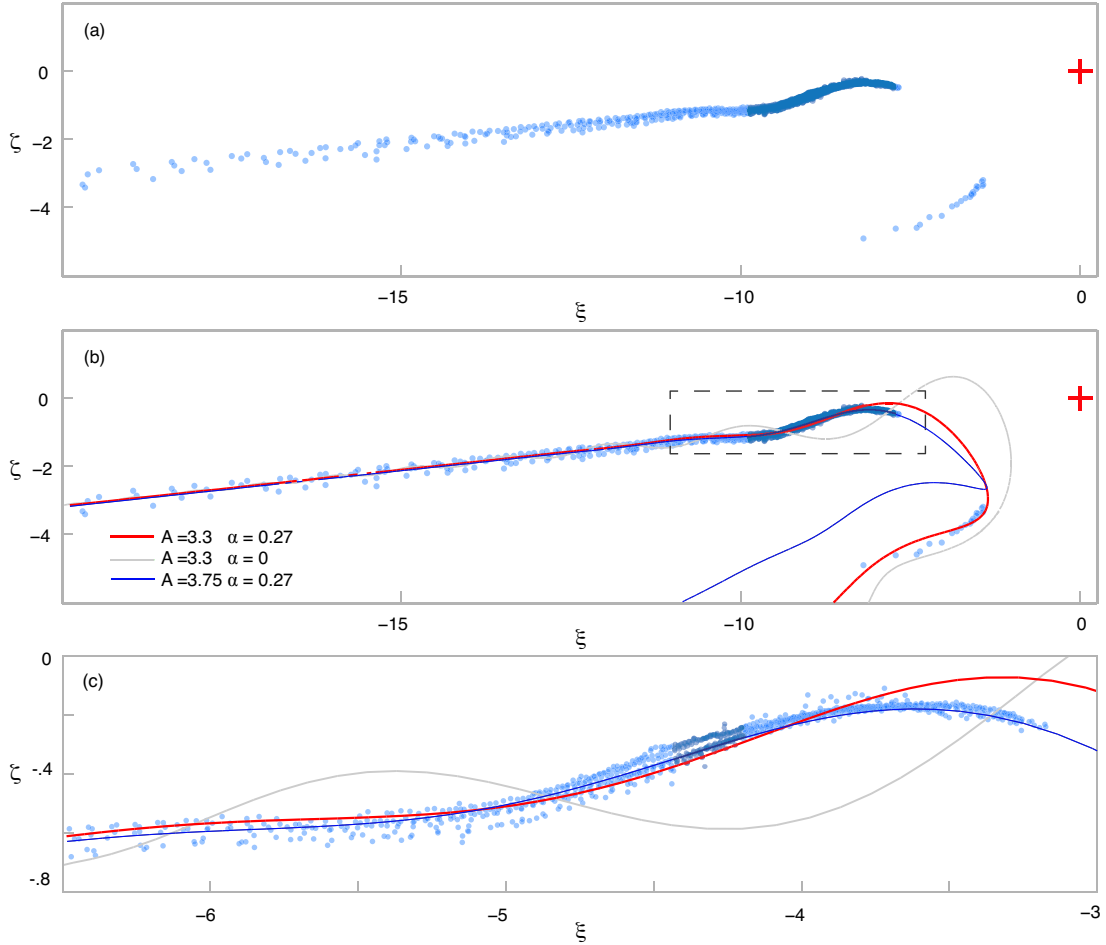


Figure 5.4: Collapse of particle trajectories in self-similar coordinates

The overlap of the curves described by similarity solutions of LIA and Biot–Savart models (colored curves) to the experimental data in similarity coordinates (blue circles). We report just the B-S curves as the LIA curves are almost indistinguishable. We show two different curves which are both in qualitative agreement with the observation: the red curve for the lower-bound value $A=3.3$, obtained by fitting the maxima to the $(z - z_0) = A(t - t_0)^{1/2}$ power law, and the blue curve for the upper-bound value $A=3.75$, obtained from this particular fit to maximize the overlap of the B-S curves (for different values of $A > 3.3$) with the upper branch of the collapsed data. These values of A correspond respectively to an inter-vortex angle of 40° and 29° . In both cases the angles that set the three-dimensional orientation are free parameters selected by hand. We also show a LIA curve without any damping (thin gray line), to demonstrate the necessity of including the mutual friction. Section (a) shows most of the collapsed data, while section (b) shows in detail the area close to the first peak of the wave marked by the dashed region in (a). The red cross represents the reconnection origin.

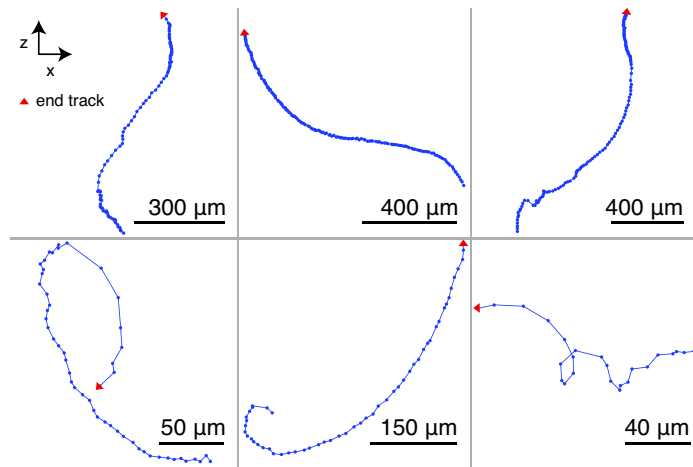


Figure 5.5: Evidence of other wave-like trajectories in superfluid

Particle tracks representing other examples that may be Kelvin waves. Each point corresponds to the particle position in one frame, and is separated from the next one by 29 ms. The red triangle represents the end of the track, to clarify the direction of motion.

Chapter 6: 3D Stereographic Microscope

6.1 Introduction & Motivation

The first direct observation of Kelvin waves excited along vortex cores following reconnection, described in Chapter 5, has generated significant interest in the superfluid community. However, the observation was in a 2D projection, and this greatly confounded the analysis. Kelvin waves are naturally three-dimensional transverse helical waves, therefore detailed, unambiguous characterization of their dynamics requires tracking their motions fully in three dimensions and time. This was the primary motivation for the development of the three dimensional stereographic imaging system, which is currently fully operational. This chapter will describe in detail the design, construction, alignment procedure and data analysis for this new apparatus. Some preliminary results are presented in section 6.5.

In addition to studying Kelvin waves, this system could also be used to revisit in 3D some of the historical measurements of thermally driven counterflow turbulence velocity statistics, completed in 2D by my predecessors Matt Paoletti and Greg Bewley [9, 42]. It would be particularly interesting to investigate whether the distribution of the pre-factor for the inter-vortex separation distance remains the same, changes, or can be constrained by knowledge of the three dimensional

geometry of the vortex lines before reconnection. The prediction based on dimensional arguments that the separation scales as $\sqrt{\kappa t}$ was confirmed experimentally in 2D [42] and for the first time in 3D in section 6.5.1.

Another interesting experiment would be to compare the motion of a single vortex line with the predictions of the Local Induction Approximation [19], including finite temperature effects. In principle, measurement of an isolated vortex line's motion in three dimensions could provide the first *local* measurement of mutual friction, which is a phenomenological description of the viscous damping between the normal fluid and superfluid vortex cores.

6.2 Physical Setup

The final design for the 3D imaging system arrived after several iterations using one or more cameras. We are grateful for the advice from our colleagues, including Nick Ouellette, Greg Voth, Stefan Kramel, Michael Schaetz, Daniel Borerro, and Greg Bewley who shared their experience designing multi-camera stereographic imaging systems for highly turbulent classical fluid flow metrology. We concluded that the reconstruction of 3D trajectories would be most straightforward if the number of free parameters needed to describe the camera geometry was minimized by the physical apparatus. For this reason, a custom camera mount was designed and constructed to precise tolerances, with the objective to minimize the number of parameters needed to describe each camera's relative position, orientation, and magnification. This is in contrast to the 3D stereographic setup of the collaborators

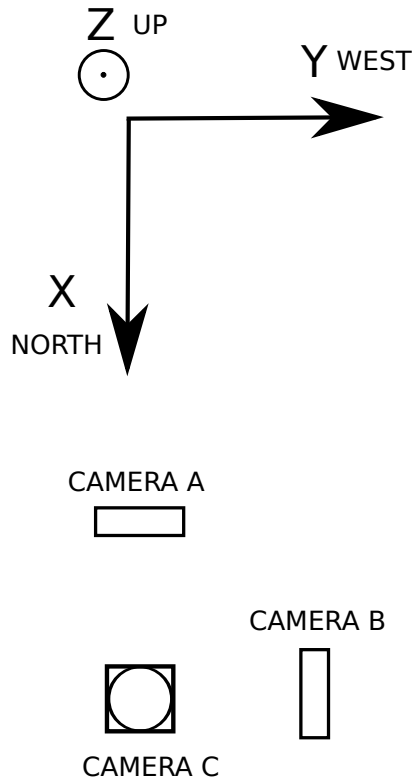


Figure 6.1: Diagram of 3D camera setup

Diagram of the right-handed coordinate system used in the 3D camera setup. The x-y plane is level and parallel to the floor, the positive X direction is due North along the length of the lab, and the positive Y direction is due West. Camera C is looking straight up and sees the x-y plane from below. Camera A and Camera B are looking parallel to the lab floor and see the z-y and z-x planes respectively.

listed above, all of whom fit all free parameters of their camera geometry in two stages: a preliminary step using a calibration target, and in post processing using a dynamical calibration obtained from the tracer particle trajectories.

The stereographic imaging system consists of three cameras, positioned perpendicularly to each other around the cryostat as shown in Figure 6.1. The cryostat and cameras are mounted on a two-deck table, to allow one camera to sit below the cryostat looking up into it. All efforts were made to place each camera perpendicular

to the others, so that the normal directions on the camera's CCD chips define a set of three orthogonal directions. The cameras sit on precision 3-axis linear micrometer-adjustable translation stages. Machined, precision flat ninety degree angle brackets attach the cameras to the stages. These allow for translation of the cameras in the alignment procedure described below as well as very fine adjustment of the focus, while preserving the mutual orthogonality of the cameras. All cameras are ThorLabs GE340-M high speed scientific grade CCD cameras capable of up to 200 frames per second. The cameras have with 640 x 480 square pixels, each of which are 7.4 μm on a side. Each camera is fitted with a 105 mm Nikkor Macro lens, set in close-focus with unity magnification. The macro lens aperture is adjustable, with the $F/\#$ set between 4 and 11 for most experiments to control the depth of field and amount of light received.

Figure 6.2 shows a side-view schematic of the 3D setup. The upper and lower decks are standard eight inch thick optical tables, and the supports between the lower and upper decks are precision machined to keep the tables level and flat relative to each other. The superfluid Helium chamber is in the tail piece of the cryostat, which extends down into an 8 inch diameter hole through the upper deck.

Figure 6.3 shows a top-down view of the apparatus, with a diagram of the illumination laser optics. Several low-pass infrared filters absorb the unwanted light at both 808 nm and 1064 nm. These unwanted wavelengths constitute a significant fraction of the total power emitted from the diode laser. The illumination laser beam is collimated with a 5 cm focal length lens, and passed through a beam expander which expands the beam by a factor of about four. The final illumination beam is

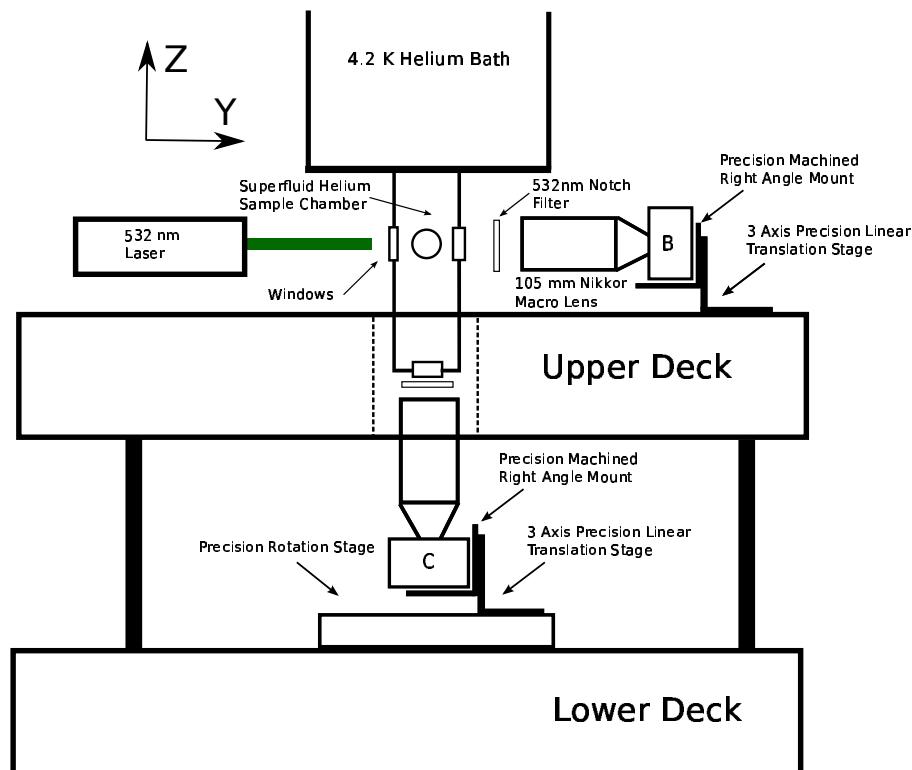


Figure 6.2: Technical diagram of 3D setup, side view

Side view of 3D camera setup. The upper and lower decks are standard optical tables. The cameras (Thorlabs 340M-GE) are held in precision, machined right angle brackets to keep the axes as perpendicular as possible. The right angle brackets are held in precision 3-axis translation stages with 1 inch travel in all directions. The superfluid Helium sample chamber of the cryostat has four vertical windows (3 shown) and one horizontal window above camera C. The tail of the cryostat extends into a 8 inch outer diameter hole drilled through the upper deck. Camera C is also mounted on a precision rotation stage, with the axis aligned closely to the center of the cryostat. All cameras are fitted with 105 mm Nikkor macro lenses with an adjustable aperture, and are set in close focus at unity magnification. Between the helium sample and all cameras are 532 nm \pm 17 nm notch filters to block the illumination light while allowing the fluorescent light to be imaged. Camera A is not shown, it is directly behind the center of the tail piece in this view.

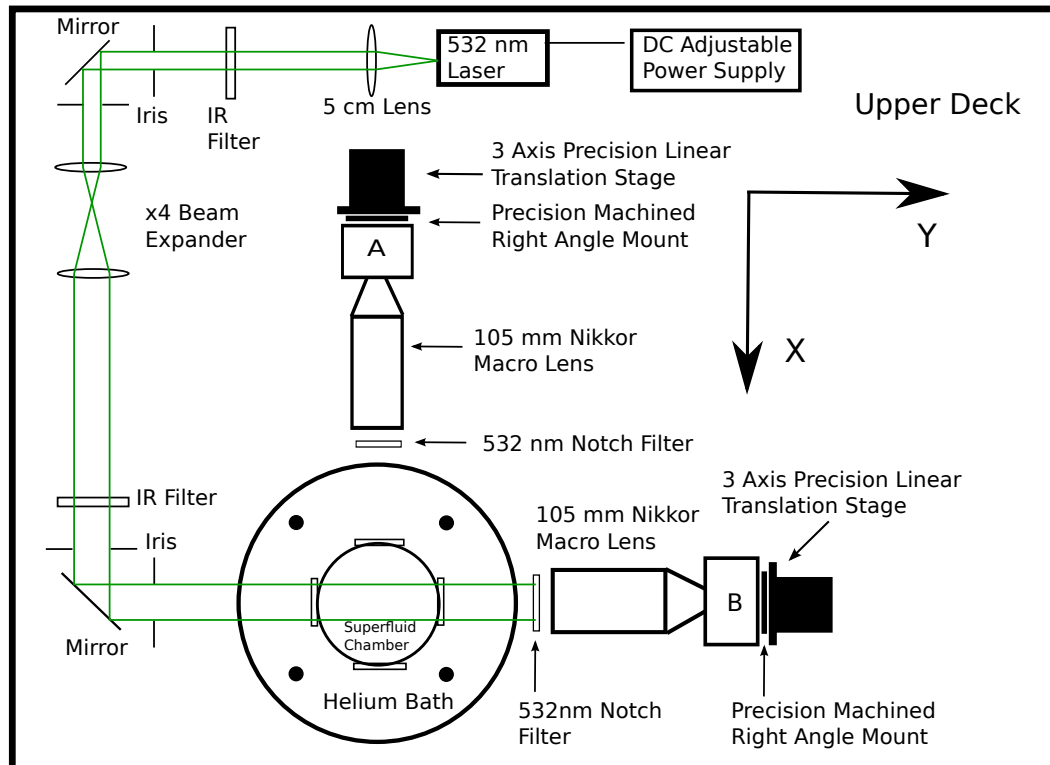


Figure 6.3: Technical diagram of 3D setup, top-down view

Top down view of the 3D camera setup. Camera C and the lower deck are not shown, they are below the cryostat. The illumination laser is shown with the attached DC power supply. At a maximum supply voltage of 3.7 VDC, this laser produces about a quarter watt of continuous-wave 532 nm light. A 5 cm lens collimates the beam, low-pass infrared filters absorb the unwanted 808 nm and 1064 nm light produced by this frequency-doubled diode laser, a beam expander dilates the beam to cover the 3D field of view, and 532 nm notch filters block the illumination light from the cameras. A ray diagram of the illumination beam is shown as the green lines above.

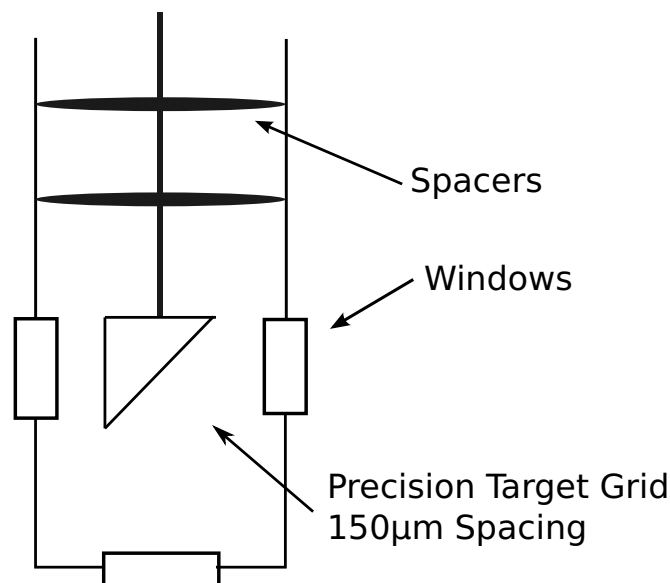


Figure 6.4: Alignment target schematic

Schematic of alignment target suspended in the tail piece of the cryostat. A support post holds a triangular aluminum brick in the middle of the sample section. A precision glass calibration grid with a $65 \mu\text{m}$ spaced pattern of dots each $125 \mu\text{m}$ apart (Thorlabs part #R2L2S3P1) is affixed over a printed cross, centered on the aluminum wedge. This dot pattern and printed cross define a 3D origin in space on which the cameras are centered during the alignment procedure. An image of the calibration target made with Camera A is shown in Figure 6.5.

about 5 mm in diameter which is suitable to illuminate the entire volume seen by all three cameras. Optical notch filters which block 532 nm light are installed in front of all macro lenses to remove the excitation light, but allow the fluorescence to be imaged.

6.3 Camera Alignment Procedure

The cameras must be aligned prior to each experiment. This procedure is made possible with the alignment target shown schematically in Figure 6.4. A

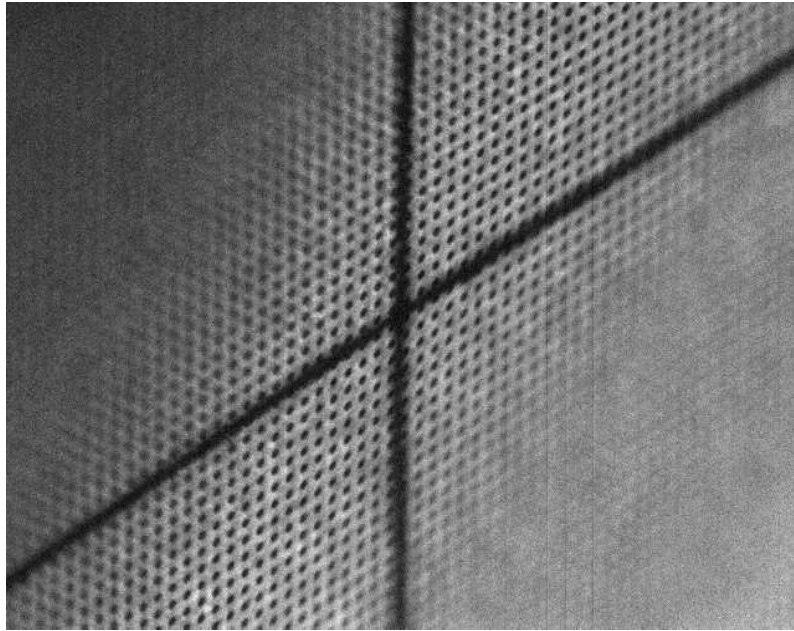


Figure 6.5: Example image of alignment target

Sample image from Camera A of the alignment target. A laser printed cross is laid under a precision glass microscope calibration target with $125 \mu\text{m}$ spaced dots each sized $62.5 \mu\text{m}$ in diameter. Note that the alignment target is turned to a 45 degree angle relative to the face of the CCD chip on Camera A, so that a line equidistant from the camera is diagonal across the image, and can be seen where the dot pattern is in best focus. This alignment target is used to define an origin in space. The experimenter translates all three cameras to center their field of view on this center, and to adjust the focus to center the focal plane through the origin.

triangular aluminum wedge is suspended inside the test section at the center, with its height adjusted to be centered at the middle of the cryostat windows. A precision microscope calibration grid with $65\ \mu\text{m}$ dots spaced in rows $125\ \mu\text{m}$ apart is overlaid on a 1200 dpi laser printed cross centered on the wedge. The height of the support post must be adjusted by hand to place the center of the target in the center of the window and illumination beam. The center of the cross defines the 3 dimensional origin in space which becomes the center of the viewing volume and coordinate system. The dot pattern provides a reference for setting the proper focus of the cameras. The wedge should be rotated so that its surface normal is approximately 45 degrees to both Camera A and B, so that the grid is equally visible in all cameras. All cameras are mounted on 3 (perpendicular) axis translation stages, and the mounts for them are machined with enough precision that the relative axes can be considered orthogonal to within the tolerances needed for stereomatching (the stages are aligned physically to within .001 inches and .25 degrees). This allows for the alignment to be completed simply by translating the cameras with the 3 axis micrometers until the alignment target is centered in their field of view, and the optimal focus is at the origin of the target.

Camera C is installed on a precision rotation stage so that it can be spun around the z-axis during the alignment procedure. This allows for the experimenter to compensate for any misalignment between the two decks. As described in the following section, a robust post processing step can account for any error in this rotation, but it is helpful during the alignment procedure to turn Camera C so that it views the target along the perpendicular lab X and lab Y axes defined by Cameras

A and B. Adjustment of this rotation to within approximately one degree or less can be achieved by hand while viewing the alignment target, which is more than sufficient as an initial condition for the post processing step.

Figure 6.5 shows an image of the alignment target taken with Camera A after the Camera is translated to the proper position. After aligning the cameras, it is necessary to ensure that the 532 nm excitation laser is also centered on the cryostat windows, passing through the origin set by the center of the alignment target.

6.4 Stereomatching

Three dimensional tracks can be reconstructed from the perpendicular views once individual particles are identified between one camera and another, a process we refer to as stereomatching. For sake of example, we will discuss the case of stereomatching between Camera A and Camera C. This is generally the most robust two-camera configuration, and the development of software to reconstruct the tracks using all cameras is still in development.

Stereomatching with two cameras is simplified by the physical alignment of the cameras relative to each other. Since they are very nearly perpendicular, each camera shares an axis with one other camera. For example, Camera A sees the lab coordinates $(Z, -Y)$ and Camera C sees the lab coordinates $(-Y, X)$. Stereomatching can be accomplished by matching the individual particle's Y coordinates.

A graphical example of this is shown in Figure 6.6, which shows the shared Lab-Y coordinate vs. time for both Camera A (blue dots) and Camera C (red

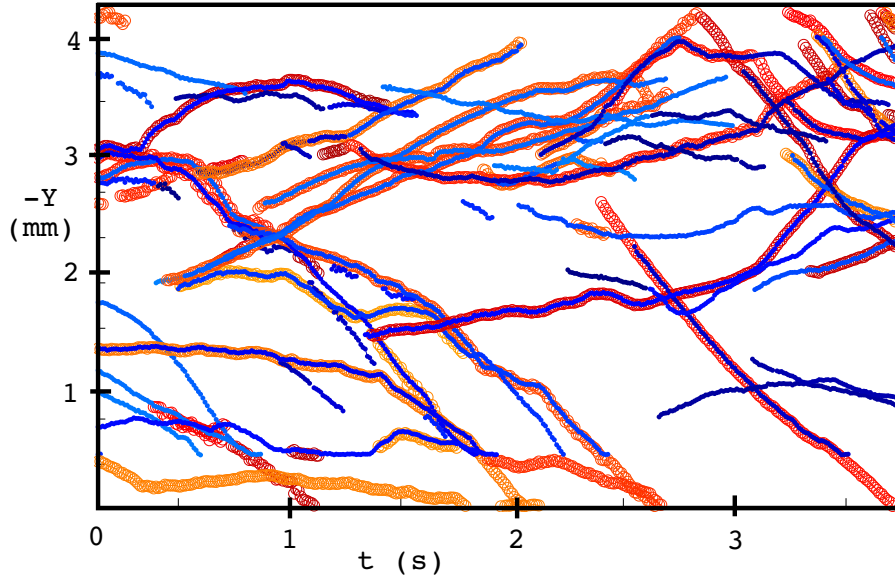


Figure 6.6: Shared particle coordinates versus time between Camera A and Camera C

Red circles show the lab Y coordinate from 2D tracks in Camera C and the blue dots show the Lab Y coordinates from 2D tracks in Camera A vs time. The track coordinates from Camera C have been rotated and translated by the parameters at the global minimum of the cost function shown in Figure 6.7. These trajectories are from 20 nm fluorescent particles dispersed in liquid helium at a mean temperature of 1.8 K.

circles). Segments of tracks from both cameras can easily be matched from Camera A and Camera C. Robust and automatic stereomatching proceeds according to the following algorithm.

6.4.1 Stereomatching Algorithm

Consider a collection of 2D tracks in two cameras. Define a_t^i to be the shared (ie Lab Y) coordinate for the i th individual track at time t from Camera A, and c_t^j to be shared coordinate of the j th individual track at time t from Camera C. We define t_{\min}^{ij} and t_{\max}^{ij} to record the first and last frame index in which tracks i in

Camera A and j in Camera C are simultaneous.

Now, we compute the cost function,

$$J^{ij} = (t_{\max}^{ij} - t_{\min}^{ij})^\alpha \sum_{t=t_{\min}^{ij}}^{t_{\max}^{ij}} |a_t^i - c_t^j|, \quad (6.1)$$

for all particle track ID's i and j in from Camera A and C respectively. For $\alpha = -1$, this function is simply the average distance between track i and j in the shared coordinate. However, we found empirically that setting $\alpha = -2$ was more robust as this choice preferentially weighs tracks which are simultaneous for longer periods of time. This helps mitigate false matching between short, erroneous or intermittent track segments. Stereomatching can now be accomplished by searching for the minima of J^{ij} , and matching the simultaneous sections of track i from Camera A and track j from Camera C. Repeatedly, matches are assigned between different track pairs (ij) until all elements of J are above some cutoff value, set by the user.

For a two camera stereographic system, care must be taken to account for the physical situation when two particles cross in front or behind each other in the volume. In the 1D projection along the shared coordinate, crossing particles will appear to intersect and hit. However, the above approach corrects well for this, as information throughout the entire track in time is used to match the best track to each other, not simply individual points.

However, there is an additional complication that sometimes a particle will be visible only intermittently in one camera, but continuously in the other. Currently, segments of tracks can be stitched together in an ad-hoc manner by hand, and indeed this was required for reconstructing vortex line filaments. Development is ongoing of

a more sophisticated algorithm which matches multiple, separate segments of tracks together, and that uses all three cameras.

6.4.2 Post Processing Track Alignment

The final stereomatching occurs after a post processing step more precisely orients the perpendicular views between any two cameras. This step involves evaluating a cost function $G(\theta, \eta)$, where (θ, η) are a rotation and translation of the 2D trajectories from Camera C relative to Camera A. The cost function is calculated as follows:

Using a_t^i and c_t^j as defined above in the previous section, we next define $\bar{c}_t^j(\theta, \eta)$, which is the shared coordinate c_t^j , subject to first a translation of η and then a rotation about the center of the image by θ . We now compute the linear distance between the shared coordinates of all stereomatched coordinates, $\delta_t^{ij}(\theta, \eta) = |a_t^i - \bar{c}_t^j(\theta, \eta)|$, for all stereomatched pairs (ij) . The cost function for the translation and rotation of the tracks from Camera C relative to Camera A is given by

$$G(\theta, \eta) = \frac{1}{N} \sum_{ijt} \delta_t^{ij}(\theta, \eta), \quad (6.2)$$

where the sum over (ij) pairs only includes stereomatched particles, and N is the total number of nonzero entries summed over. An example of a cost function is shown in Figure 6.7, which displays a clear minimum.

The optimal translation and rotation of 2D tracks in Camera C for stereomatching with Camera A is now given by

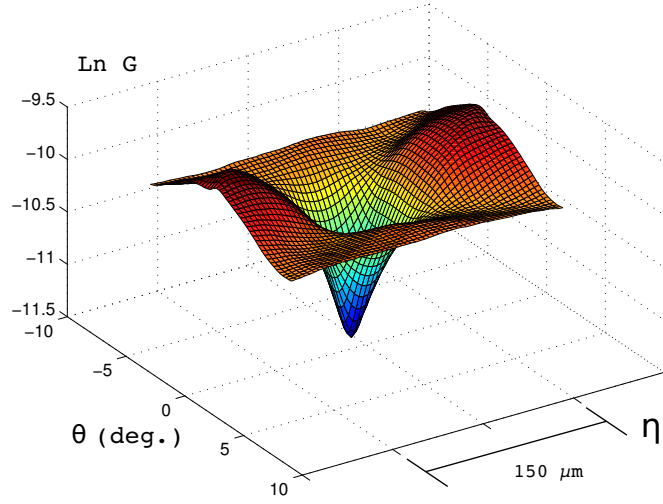


Figure 6.7: Track alignment cost function example

Example track alignment cost function. The log of the cost function (arbitrary units) described below is evaluated over a range of rotations and displacements of Camera C relative to Camera A. The cost function is smooth and convex around the global minimum. The global minimum gives the best alignment and rotation for 3D stereo matching between the two cameras.

$$(\theta^*, \eta^*) = \arg \min \{G(\theta, \eta)\}. \quad (6.3)$$

The final step in the 3D reconstruction of the particle trajectories is to repeat the stereomatching procedure as described in section 6.4, with the 2D tracks adjusted according to (θ^*, η^*) .

6.5 Preliminary 3D Results

The following sections present some of the first 3D data. We demonstrate that the technique described above works for tracking up to about one hundred particles

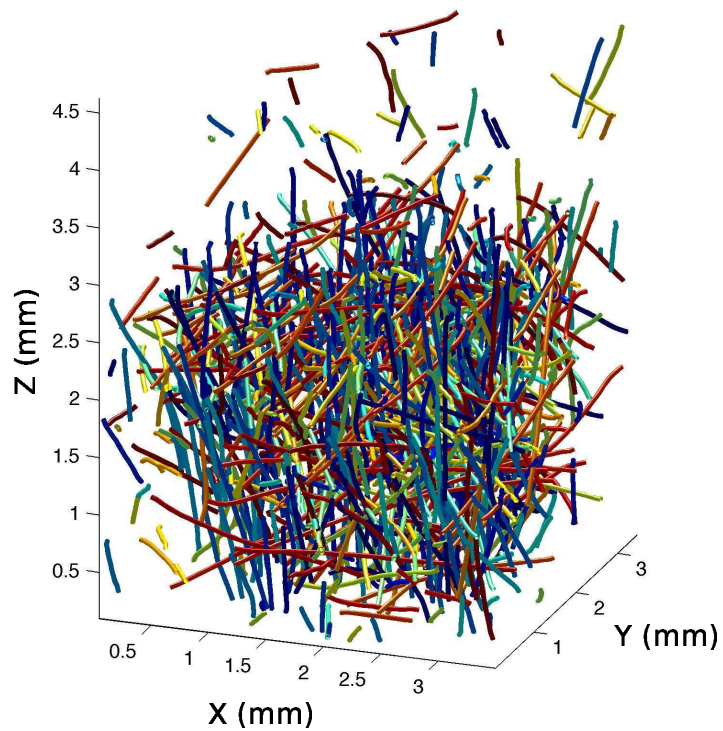


Figure 6.8: Forest of several thousand 3D particle tracks

Collection of several thousand 3D single-particle trajectories. The particles are 20 nm fluorescent particles dispersed in Liquid Helium at a mean temperature of about 1.8 Kelvin. All stereomatched trajectories from a twenty second movie are shown. Rendering in MATLAB courtesy of Nick T. Ouellette.

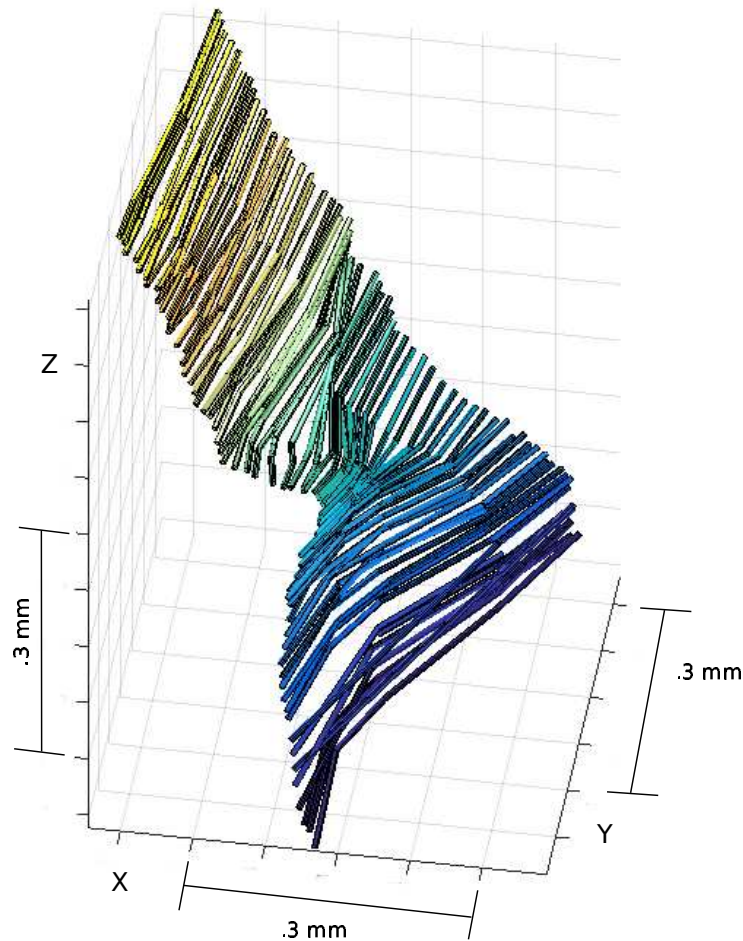


Figure 6.9: Example vortex line reconstructed in 3D

3D reconstruction of a vortex line. Time is indicated by color from yellow to blue, and each segment is separated in time by 30 ms. This vortex line was in the vicinity of a reconnection event, which caused the ripple seen in the middle.

simultaneously, as shown in the individual particle trajectories in Figure 6.8. Furthermore, individual vortex lines can also be tracked. Once a collection of particle which appear trapped on a vortex line are identified, fitting a spline to their coordinates infers the vortex core location continually along its arclength. An example of the first 3D reconstructed vortex line is shown in Figure 6.9. Future studies could compare the 3D motion of a vortex line to the dynamics predicted by the Bio-Savart

and Local Induction Approximation filament models described in section [1.3.1](#) and [1.3.2](#).

6.5.1 First 3D Reconnection Observation

Following is the first observation of vortex reconnection in 3D. A single vortex line was observed with six tracer particles decorating the core, each separated by about $50 \mu\text{m}$. Another vortex (undecorated) approached and reconnected, leaving two particles on one retracting branch and four on the other. Three dimensional trajectories of all six particles are shown in the Figures [6.11](#) and [6.12](#). The particles are labeled 1-4 on one branch and A, B on the other branch. To clarify, a schematic of the presumed vortex and particle locations is shown in Figure [6.10](#). We emphasize that these trajectories are the specific locations of individual particles trapped on the vortex cores but do not trace out the entire core, unlike the reconstruction of the vortex filament in Figure [6.9](#). Helical motion of the retracting vortex is evident in the trajectories labeled A and B.

Previously in our group, Matt Paoletti characterized about 20,000 vortex reconnection events measuring the separation distance between two points on vortices following reconnection [[44](#)]. From dimensional arguments (the quantum of circulation κ has units of m^2/s), it was expected that the separation distance between them, $\delta(t)$, would obey the following scaling in time:

$$\delta(t) \propto t^{1/2}. \tag{6.4}$$

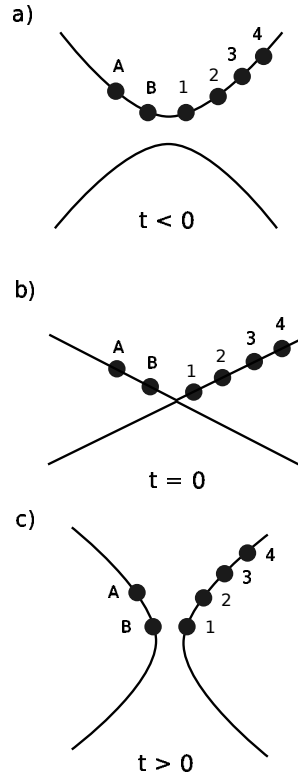


Figure 6.10: Schematic of the first observation of 3D vortex reconnection

This schematic shows the location of the tracer particles before and after the reconnection event. The trajectories for particles A, B and 1-4 are shown in Figures 6.11 and 6.12. Before the reconnection (a) there are six particles separated by about $50 \mu\text{m}$ decorating one vortex; the second vortex is invisible. The two vortices approach and cross at $t = 0$ (b). After the reconnection (c) the vortices retract having exchanged tails, leaving two particles on one vortex and four on the other. Figure 6.13 shows the separation distance versus time for the particles on the different branches, and Figure 6.14 shows the separation distance between particle B and 1 versus time on a log-log plot; a least-squares power-law fit is also shown.

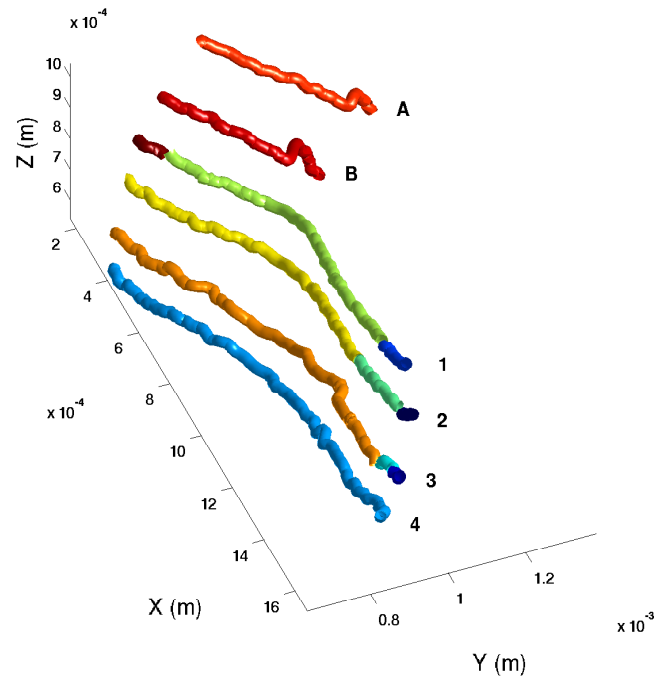


Figure 6.11: 3D vortex reconnection, first view

Trajectories of six particles trapped on a vortex core which reconnected. The second vortex was not decorated by tracer particles, but intersected between particle 1 and B labeled above. These trajectories indicate the locations of specific tracer particles on the vortex core, not the core itself. A second view of these trajectories is shown in Figure 6.12. Figure 6.10 shows a schematic of the vortex and particle configuration for clarity. We are grateful for the hand-tracked particle locations provided by Peter Megson.

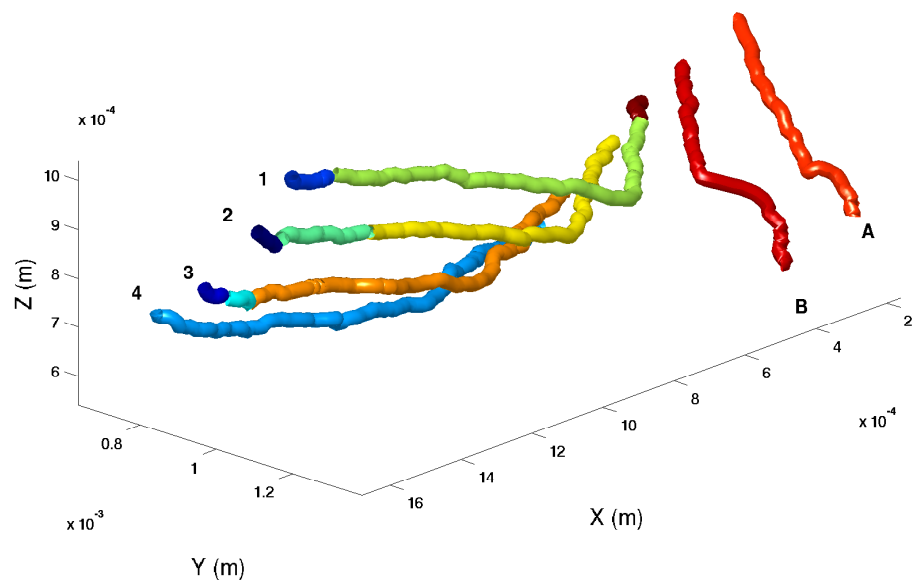


Figure 6.12: 3D vortex reconnection, second view
 Second view of the reconnection shown in Figure 6.11

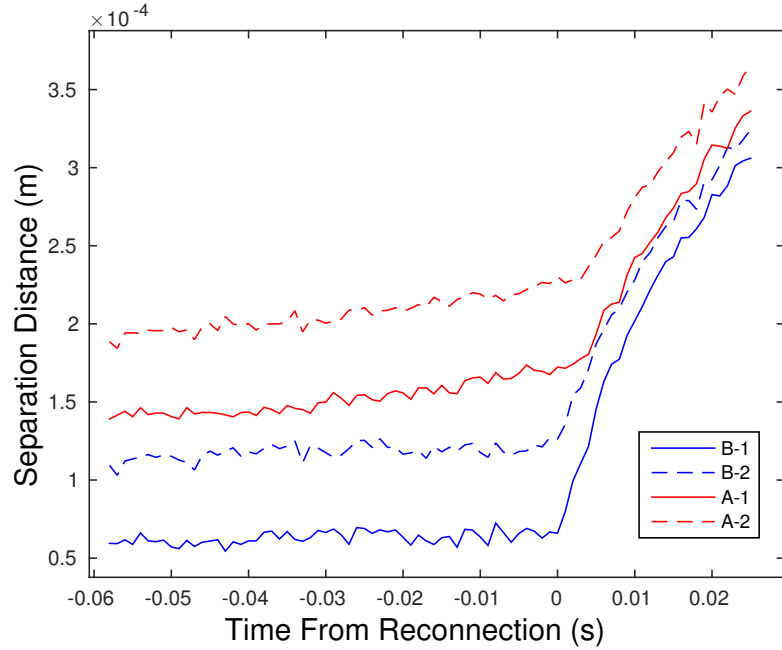


Figure 6.13: Separation distance δ versus time for 3D reconnection

Separation distance calculated in 3D between particle trajectories on the two branches. The time axis is shifted to place the reconnection event at $t=0$.

The analysis by Matt Paoletti found strong agreement with this scaling, but the measurements were made in a 2D projection. Figure 6.13 shows the computed distance between the trajectories on separate branches fully in 3D. To compare to the predicted scaling, we selected the two closest particle trajectories: B and 1. Figure 6.14 shows a log-log plot of the data, and a least-squares fit to the form

$$\delta(t) = A\sqrt{\kappa}(t - t_0)^{1/2}. \quad (6.5)$$

The time offset t_0 was adjusted to maximize the fit, and permitted to take continuous values between the discrete (separated by 10 ms) frames of the camera. The dimensionless prefactor A was measured to be ≈ 1.94 which is close to the

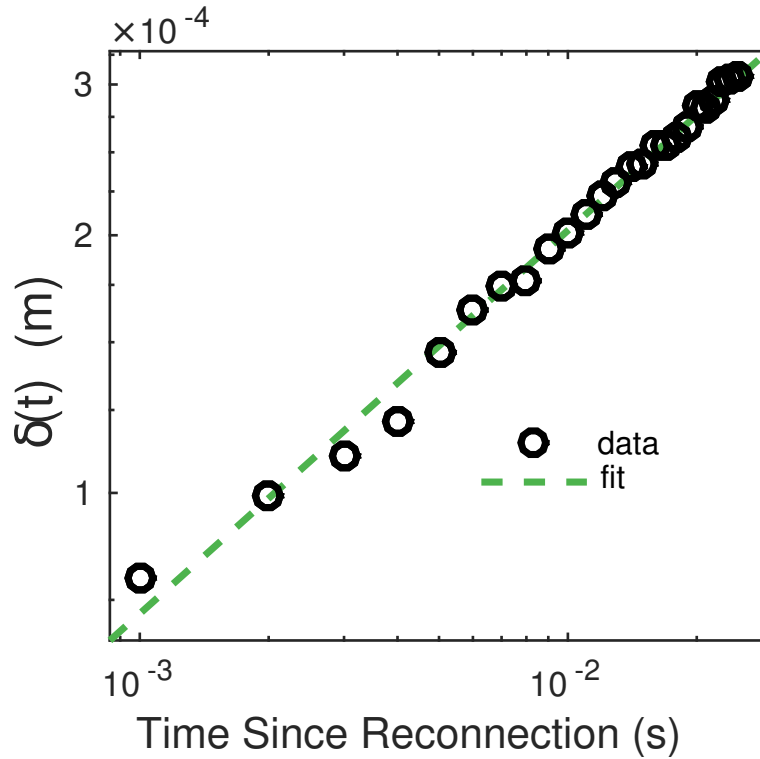


Figure 6.14: Separation distance δ on log-log plot with power-law fit
 Log-log plot of the separation distance versus time for the initially closest pair of particles, B and 1. A least-squares fit to the form given by Equation 6.5 shows excellent agreement with the predicted scaling $\delta \propto t^{1/2}$, and the measured value of the dimensionless prefactor A is close to the average value measured previously in projection.

average value of the prefactor measured in projection by Paoletti, which had a broad distribution around the value of $A \approx 1.25$. This data further corroborates the scaling suggested in Equation 6.4, measured here for the first time in 3D.

Chapter 7: Future Objectives

A significant fraction of this thesis describes contributions to the functionality of the experiment (robust dispersal of nanometer scale tracer particles, lower temperatures accessible) and additional, novel and unique metrology contributions (3D visualization and higher frame rates, faster speeds possible for particles to remain on vortices). We suggest that there are two main areas for future work, which are currently readily accessible but beyond the scope of this thesis. Section 7.1 describes some future directions concerning the nanoparticle dispersion, and section 7.2 describes some newly-enabled 3D measurements which would be interesting.

7.1 Future Nanoparticle Work

While the new capability to disperse nanometer scale fluorescent particles has been transformative for liquid helium experiments, there are some shortfalls of this technique and unknowns which should be further investigated. This section will describe some practical obstacles, offer some speculation about possible remedies, and summarize what has been tried so far but remains otherwise unpublished.

7.1.1 Tracer Particle Density

One primary difficulty with this technique is dispersing a high enough density of particles per volume to decorate the vortices. The current 3D setup images a 60 mm^3 volume. It has been found empirically that vortex lines do not become decorated with particles unless several hundred particles are dispersed in this volume. The amount of particles released from the dispersal apparatus can be controlled to some degree by how many are loaded onto the tube, however, it has not been possible to get the number of particles dispersed from sonication high enough to reliably decorate vortex lines. The number of particles loaded onto the tube can be over 10^{14} , however only order 10 are visible in the viewing volume. The sample volume holds about a third of a liter of helium, so this means only about 5×10^4 particles are released in total. It seems that increasing the efficiency of the dispersal is the key.

Perhaps some surface treatment of the dispersal tube, or chemical modification to the surface of the particles would help. The particles have charge embedded in them to prevent clumping in aqueous applications, and have a surface coating of a negatively charged carboxylate group. The particles' charge could be binding them quite strongly to the metal surface of the dispersal tube by forming image charges in the conductive steel. In one attempt, an approximately stoichiometrically equivalent amount of hydrochloric acid was added to the aqueous solution to act as a proton donor to neutralize the particle surface. This test did not make a significant difference in the dispersal efficiency in liquid nitrogen, however these tests were not

nearly exhaustive. A bench top air de-ionizer was also pointed at the tube and left for about 30 minutes after the particles were evaporated onto the tube at room temperature. It was hypothesized that the particle surfaces would capture ions and neutralize the charge, however this did not seem to have any effect.

In addition, some efforts that were made to mechanically increase the dispersal efficiency should be mentioned. Additional wraps of wire were silver-soldered onto the tube to increase surface area, however this had no significant effect on how many particles were released. Currently, there has been no specific effort made to match the acoustical impedance between the transducer, aluminum focusing cone, and the tube. More specific impedance matching would increase the energy delivered to the tube and could increase the number of particles released. The wavelength of the main transverse acoustic mode was measured at room temperature to be about 1 cm. The maximum shear occurs only at the anti-nodes of this wave, so perhaps increasing the driving frequency above 45 kHz to add anti-nodes along the tube's length would be beneficial.

One ad-hoc attempt was made during a liquid helium experiment to drive the ultrasound transducer over a range of frequencies from about 10 kHz to 150 kHz. This was done using a signal generator, an audio amplifier and a step-up transformer. However, this setup was unable to deliver high enough voltages to the transducer and did not drive enough power to disperse any particles. Several resonances were found both below and above the usual 45 kHz. A new MHz frequency transducer and electrical amplifier would be worth trying in future work, and ideally some ability to tune the driving frequency would be helpful to find resonances of the

tube (which will be slightly different in-situ from room temperature because of the steep temperature gradient from room to liquid helium temperatures over less than a meter).

Professor Seth Putterman conjectured that the particles are removed by the shock wave released during the collapse of cavitation bubbles generated from the ultrasound vibration. Indeed, it appears that the tube is surrounded by bubbles when sonicated, so cavitation could be involved and this mechanism should be further investigated.

Another explanation for the apparently small density of particles could be that the fluorescence mechanism may be modified or broken at such extreme temperatures. The fluorophore is a large organic molecule which is undergoing molecular fluorescent transitions, conceivably the absorption and emission wavelengths could be altered so that we cannot drive or observe the resulting fluorescence transitions with our current optical setup. The fluorescence spectra and intensity should be monitored as a sample of particles is cooled from room to cryogenic temperatures.

7.1.2 Particle Size & Clumping

Caution should be exercised in stating the tracer particle's radius in-situ. We have no guarantee that the nanoparticles are not clumping or forming aggregates, although they appear to be quite mono-disperse in brightness. The Life Technologies 20 nm particles have the equivalent of about 2×10^3 fundamental charges of net, negative charge. The Coulombic repulsion is sufficient to keep them mono-disperse in

aqueous solutions, but might not prevent particles from irreversibly sticking together when they are dried onto the tube.

7.1.3 Lifetime in Field of View

When dispersed in liquid helium, the nanoparticles disappear from the field of view on the order of a minute or two. This cannot be explained by free-fall due to gravity (unless the particles are in larger than 1 μm clumps). Coulombic repulsion from their overall net charge could push the particles apart, and this would be aided by the formation of opposite image charges on the inside aluminum walls of the cryostat. Keeping the particles suspended in the field of view longer would allow for much better measurements; currently the helium is quite agitated after activating the ultrasound transducer, making careful measurements of a quiescent state challenging. Future efforts should investigate why the particles disappear from the field of view so quickly and remedies should be sought.

7.1.4 Comparison to Particle Vortex Calculations

The calculations of Chapter 4 provide precise, testable predictions for the maximum speed which particles may remain trapped on vortex cores versus the particle radius. The technique described in Chapter 3 provides a reliable method for dispersing a wide range of particles from 5 nm to several microns in diameter. It is frequent that we observe particles (presumably trapped on vortex cores) accelerate to very high speeds and then suddenly stop after becoming untrapped. Qualitatively,

we observe nanoparticles moving significantly faster than the micron-sized snow particles. However, no quantitative studies have yet been performed to measure the speed at which particles become dislodged. We suggest that this study be completed, and note that the data needed to perform this study may already exist in our repository.

7.2 Future 3D Work

The technique described in Chapter 6 provides the world-first capability to dynamically measure the motion of tracer particles fully in 3D, and has already been used to characterize a vortex reconnection with the preliminary data presented in Section 6.5.1. Verifying all the historical measurements made in projection again in 3D would be of interest, especially the non-gaussian distribution of velocities found in thermally driven flows [9, 42].

A detailed study of the scaling of the separation distance between vortices in 3D would be a logical next step. Comparison to the historical measurements in 2D projection of [44], across a range of temperatures and particle sizes would be interesting. Perhaps the distribution of the pre-factor will collapse, or be found to have a straightforward temperature and geometric dependence which is otherwise obscured in projection.

Vortex reconnection is fundamentally a three dimensional process. Studying vortex reconnection in 3D is important for at least two specific reasons which are immediately apparent. Firstly, there currently are analytic theoretical predictions

relating the angles of the vortices before and after reconnection [86] which otherwise cannot be unambiguously tested without 3D observations. These calculations assume zero temperature, which may be a realistic approximation at the coldest temperatures currently achievable in experiment, and if not the discrepancies could shed light on the interaction of vortices with the viscous normal fluid in important ways. Secondly, the degree to which vortex reconnection is time-reversal symmetric also has consequences of fundamental importance, as the reversibility is related to the amount of energy which may be lost during reconnection. This energy loss is theorized to play an important role in the dissipation of quantum turbulence, which otherwise cannot be explained by the nearly vanishing viscosity in the system at temperatures approaching zero Kelvin. Characterizing vortex reconnection in 3D would allow for a detailed analysis of the approach to and retraction from a reconnection, and this data would allow study of the asymmetry before and after reconnection.

Lastly, Kelvin waves are also a fundamentally 3D phenomenon. Analysis of the data presented in Chapter 5 was confounded by projection effects. It would be interesting to study the excitation and propagation of kelvin waves fully in 3D, across a range of temperatures.

Chapter A: 2D Particle Tracking Tutorial

Liquid Helium flows and the dynamics of quantized vortices can be quantitatively studied by tracking the motion of tracer particles dispersed in the flow. Here we describe in detail the implementation in MATLAB of a Lagrangian particle tracking algorithm suitable for our experiments. The tracking algorithm follows a series of steps which are detailed below:

1. Spectral filtering of raw images
2. Finding approximate particle locations from peak-picking
3. Calculating sub-pixel accurate particle centers
4. Linking particle locations into specific tracks through time

Spectral filtering almost always improves the robustness of the automatic tracking. The sub-pixel sized particles are imaged as diffraction patterns with radii between 1 to 5 pixels generally. The size of the diffraction pattern depends on the $F\#$ of the imaging lens, and other factors such as the depth of the imaging volume and illumination laser position. Spatial band-pass filtering is useful to isolate the image data to spatial scales containing the particles. This helps to remove uncorrelated pixel noise on the small-wavelength side and large-scale variations due to the

Gaussian illumination beam profile, non-zero and non-uniform average background intensity, erroneous exterior light from the lab, and out-of-focus fluorescence from particles out of the imaging volume or stuck on the cryostat windows. A small wavelength cutoff of one or two pixels, and a large wavelength cutoff of as small as 4 pixels (for high-density movies) or as large as 12 pixels (for low F#, small depth of field images with sparse density) is generally appropriate. Our algorithm computes the bandpassed images by performing a real-space convolution with the appropriate Gaussian kernel. Optimal small and large wavelength cutoffs generally must be selected manually for each movie, but can easily be found by viewing the images qualitatively for a variety of values.

The next step in tracking is to find a preliminary guess of each particle's location. This is done with a simple peak-picking routine, which records a list of locations for all pixels above a threshold value specified by the user. The peak-picking also excludes adjacent centers within a certain radius. This radius should be about equal to the long-wavelength cutoff in the bandpass filtering to avoid several local maxima of one particle mistaken as several particles. Selection of an appropriate pixel threshold value must also be found manually, however a histogram of pixel values throughout a movie can be very helpful. Figure [A.1](#) shows a histogram of all pixel values for a movie after bandpass filtering. An appropriate peak-finding threshold value is shown as the vertical red line. Notice that to the left of the line, the distribution shows Gaussian noise, however the distribution changes abruptly at this value with a long tail including the pixels with actual particles. Empirically, it has been determined that setting the peak-finding threshold to the value where

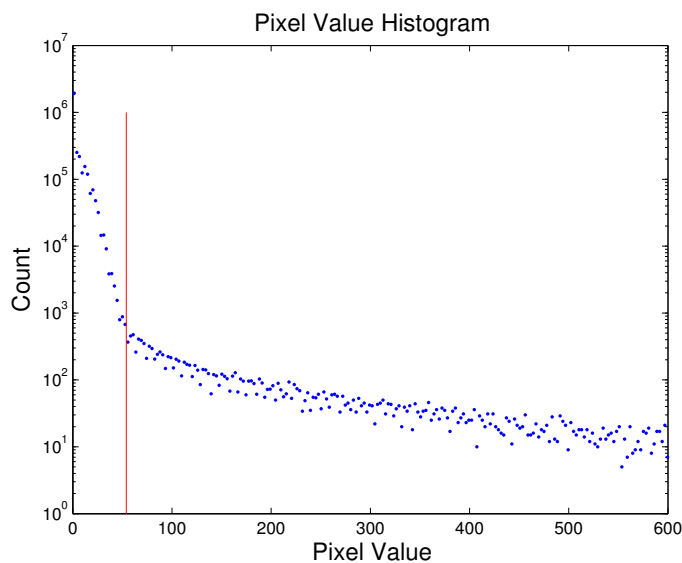


Figure A.1: Pixel value histogram for peakfinding threshold selection

Histogram of all pixel values in a bandpass filtered movie. There are two distributions present, Gaussian noise on the left and a long tail on the right. The tail includes pixels which actually have particles in them. The empirically optimal peak finding threshold value is found at the corner in this histogram (or slightly above) as shown by the vertical line.

this distribution changes (or slightly higher) is optimal, and results in almost all particles being identified and very few false-positives. Figure A.2 shows red circles identifying pixels selected by the peak-picking algorithm.

To calculate the exact particle centers, first a square section of the image is cut out around each pixel identified in the peak-picking. Another important parameter the user must specify is the size of this cut-out, generally the side length should be a little larger than twice the size of the long wavelength cutoff in the bandpass filtering. For each cut-out, the mean of the image is subtracted, and all pixel values less than some percentage (usually around 15%) of the peak value are set to zero. Zeroing these pixels helps prevent noise in pixels outside the particle contributing

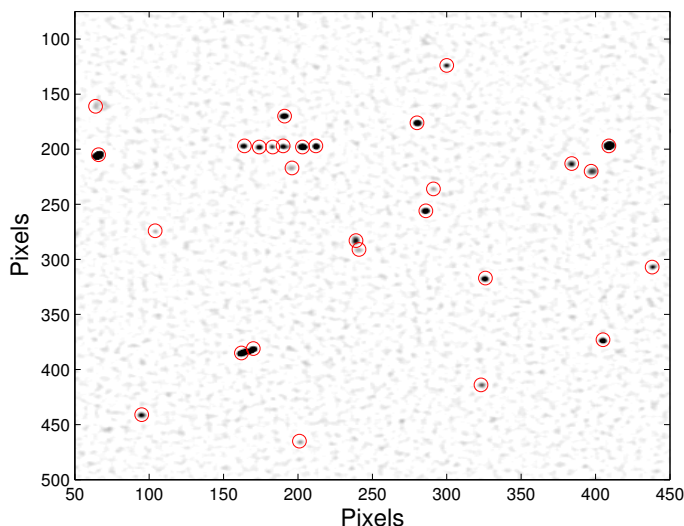


Figure A.2: Example of peak-picking for finding approximate particle locations

A single contrast-inverted frame from a movie, after bandpass filtering. Red circles show the pixels identified by the peak-finding algorithm, using the threshold value shown in Fig A.1.

to the particle center, especially when the cut-out is too large. The cut-out is then normalized to have total sum equal to unity. The particle location is then calculated as the “center of mass,” using the pixel intensity values as a density. The center of mass closely approximates the center of the diffraction pattern produced by the point-spread function of our imaging system; fitting a Gaussian or Airy disk pattern is computationally expensive and produces no noticeable improvement. For high signal-to-noise ratio movies (more than 1000 counts above the noise floor) this technique can localize particles to as little as a tenth or twentieth of the pixel size. Even for noisy images (25-100 counts above noise floor) this algorithm works to sub-pixel accuracy. An example of a processed cut-out is shown in Figure A.3

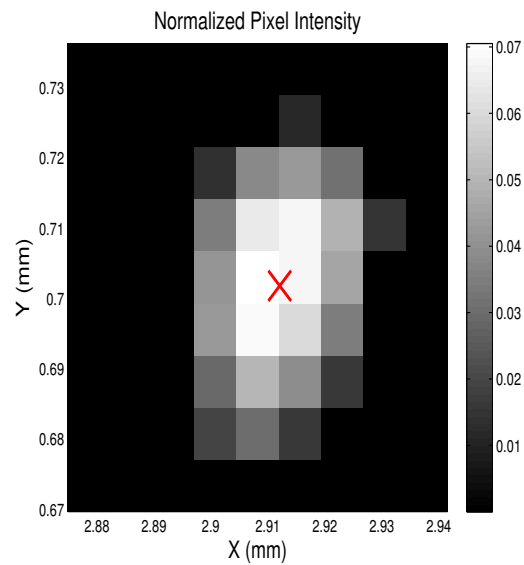


Figure A.3: Example center-of-mass calculation for sub-pixel accurate particle localization

An extracted cut-out of a movie around a peak. The particle location is found by computing the center of mass, using the normalized pixel values as density. These sub-pixel accurate locations are linked by the particle tracking algorithm into trajectories through time.

Below is an important section of the MATLAB code which calculates the sub-pixel particle locations:

```

%I(:,:,k) is image at k'th frame in time
PIXELSIZE = 7.4E-6 %(for Thorlabs cameras)
x = (1:size(I,1))*PIXELSIZE; %arrays to convert pixel locations to meters
y = (1:size(I,2))*PIXELSIZE;
meanI = mean(mean(I(:,:,k))); %calculate pixel mean of entire image
% finds peaks of k'th image
% in (bandpassed) movie sequence
pks = pkfnd(I(:,:,k), PKFINDTHRESHOLD,PKFINDMINSEPARATION);
%loop over all found peaks, calculating sub-pixel accurate centers
x0 = zeros([length(pks),1]); %arrays to store x and y coordinates (meters)
y0 = zeros([length(pks),1]);
for p = 1:size(pks,1) %loop over all found particles
    cx = pks(p,1); % x coordinate (pixels)
    cy = pks(p,2); % y coordinate (pixels)
    FITRNGX = (cx-MASKSIZE):(cx + MASKSIZE); % integer arrays of pixel indices
    FITRNGY = (cy-MASKSIZE):(cy + MASKSIZE); % around peak
    %extract mask from image
    f = double(I(FITRNGX,FITRNGY,k));
    %subtract mean of image
    f = abs( f - meanI);
    %calculate value to zero pixels below, generally CULLTHRESHOLD = .15
    cull = max(f(:))*CULLTHRESHOLD;
    %zero all pixels in mask below threshold
    f(f < cull) = 0.0;
    %normalize to have unit integral
    f = f ./ sum(f(:));
    %create 2D meshgrid of pixel locations in meters
    [xx,yy] = meshgrid( x(FITRNGX), y(FITRNGY) );
    %calculate x and y coordinates (meters) of center of mass
    x0(p) = sum(sum( xx.*f ));
    y0(p) = sum(sum( yy.*f ));
end

```

The final step for particle tracking is to assemble tracks through time from a list of all particle positions from each frame. Our implementation borrows from the widely-used nearest-neighbor based algorithm written by Crocker and Grier. This algorithm links particles into specific tracks by a simple nearest-neighbor criteria. Particles are linked to whichever track was closest to them in the previous frame. More complex, predictive algorithms for track assembly exist, however these assume the particle has non-negligible inertia and make assumptions about the particle's

kinematics which are not appropriate for superfluid flows. Figure A.4 shows a collection of particle coordinates found throughout a movie, but not yet assembled into trajectories. Figure A.5 shows the locations assembled into specific, uniquely identified tracks after running the nearest-neighbor based algorithm. There are two more important parameters which must be set. The nearest-neighbor algorithm requires an upper bound in distance across which a particle trajectory can be linked. Be aware that this imposes an upper bound speed-limit for tracking, its distance multiplied by the image sample rate in Hz is the fastest velocity the final tracks will have. Some manual optimization of this distance is required, because too large a distance can result in false links in the track and enormously increases the combinatorial size of the search. Finally, eliminating all tracks shorter than a specified number of frames long is very helpful, generally tracks less than 5-10 frames long are superfluous or artifacts. Tracks are automatically removed if shorter than a user-specified cutoff in frames.

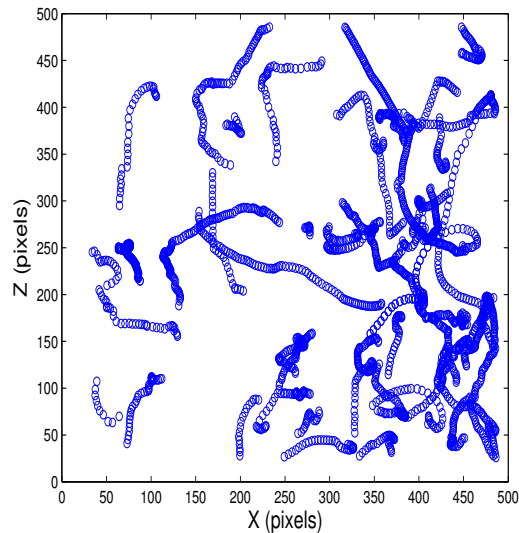


Figure A.4: Untracked particle locations throughout movie
 Scatter plot of particle locations throughout a movie. The locations have been found to sub-pixel accuracy, but not yet assembled into trajectories.

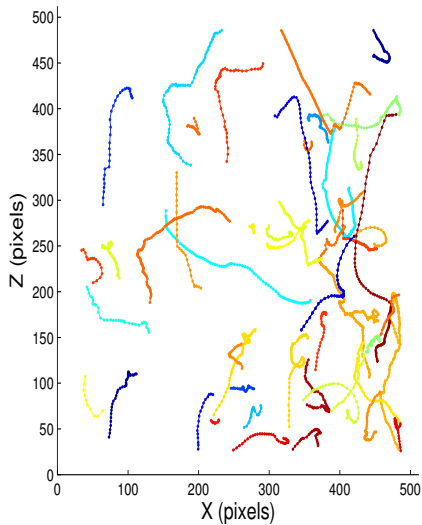


Figure A.5: Example of tracked particles
 Particle trajectories after assembling tracks using a nearest-neighbor based algorithm. Tracks are colored according to their unique ID number.

A.1 MATLAB Example

The following section provides a step-by-step walk through of the current MATLAB implementation of the 2D tracking code.

```
% add path to matlab code on wave.umd.edu
path(path, '/data/user_data/dpm314/matlab_scripts');
%filename for movie to read
fnameA = '/data/user_data/dpm314/12_21_14 ...
/camA/Untitled027/Image_0001_0001.raw'
nx = 640; ny = 480; numFrames = 10000;
%read raw movie data
Ia = readRaw(640, 480, 10000, fnameA, 'uint16');
%bandpass images
smallWavelength = 1;
largeWavelength = 5;
Ia = bandpassImageStack(Ia, smallWavelength, largeWavelength);
%(optional) play an animation of the bandpassed images
clims = [0, 150]; %pixel values for setting contrast level in animation
dpmflip(Ia,clims);
%display pixel value histogram for determining peakfind threshold
loghistdpm( double(Ia( 1:(nx*ny*10)) ), 1000);
%assign parameters for particle localization and tracking code:
PKFINDTHRESHOLD = 100; %threshold pixel value for peak-finding
MASKSIZE = 5; %one-half of side length of image cutout (in pixels)
%for center of mass calculation
PIXELSIZE = 7.4E-6; %physical size of pixels in meters
%Note, set this to 1.0
%to keep all output in terms of pixels not meters
CULLTHRESHOLD = .15; %percentage below maxium value to zero inside cut-out
MAX_DISP = 4*PIXELSIZE; %maximum displacement (meters) between adjacent
%frames to link in single track
MIN_LENGTH = 5; %minimum duration of a track in frames (time)
X = 1; Y = 2; FRAME = 3; ID = 4; %track matrix columns

%Actually perform particle localization and tracking:
A = track_dpm(Ia, PKFINDTHRESHOLD, MASKSIZE, PIXELSIZE, ...
    CULLTHRESHOLD, MAX_DISP,MIN_LENGTH, X, Y, FRAME,ID );
%A(:,1) are X coordinates (meters). A(:,2) are Y coordinates.
%A(:,3) are times in frames. A(:,4) are unique particle ID's
%(optional) plot linked tracks colored uniquely by ID and time
plotById(A)
%(optional) play animation of original movies with tracks overlaid
flipTracks(Ia, clims, A);
```

Chapter B: Standard Operation Procedure

B.1 Initial Setup

System Status: 1-2 Days before run.

Everything at STP, outer vacuum jacket (OVC) passes leak-checking.

- Verify all electronics are connected and working
- Verify Arduino and timestamp python code working
- Check illumination laser alignment
- Clear hard drive space on camera computers
- Clean test section (TS)
- Verify TS & Bath can be pumped to < 20 mTorr, and leak rate less than a few mTorr / second when pneumatic valve closed
- Rough pump OVC to < 100 mTorr, then activate turbo pump
- Verify 0.0 mTorr reading on OVC pressure gauge, can take a few hours to overnight to pump down

B.2 LN2 Pre-cool

System Status: OVC Pumped to < 1 mTorr, everything at Room Temp.

Goal: Bath full with LN2 and at 77 K, TS at room temp with N2 Gas or atmosphere only (capillary closed!).

- Pump TS and Bath to < 20 mTorr, all valves and capillary open
- Repeat 'Fill and Flush' with Nitrogen gas several times
- Close Capillarity valve to prevent LN2 getting into TS
- Pressurize with N2 Gas above 1 atm
- While streaming N2 out, insert LN2 transfer line connected to Dewar and begin filling
- Stop streaming N2 Gas in as soon as LN2 Dewar connected

- Continue filling LN2 until mist seen exiting Bath blowoff valve (≈ 10 minutes)
- Remove transfer line, isolate Bath from TS
- Leave overnight to cool Bath, radiation shields, OVC etc.

B.3 Day of Run Preparations

System Status: Bath full with LN2 at 77 K, TS at room temp.

Goal: System ready to start pre-cooling TS with LN2 from Bath.

- Verify TS is clean and clean TS insert if needed
- Load nanoparticles onto Ultrasound Tube per Chapter 3
- Align all three cameras per Chapter 6
- Verify Laser alignment
- Verify electrical connections to cell thermistor, counterflow heater, camera triggers etc.
- Install TS insert with nanoparticles dried on tube, make sure counterflow heater is flat and level
- ‘Fill and Flush’ TS to remove atmosphere **DO NOT pump on Bath, or else LN2 will freeze**
- leave TS with pressurized N2 gas

B.4 Pre Cool TS with LN2

System Status: Bath full of LN2 at 77 K, TS with pressurized N2 gas only.

Goal: TS and Bath at 90 K.

- Turn on cameras and start camera software, setup data folders, etc.
- Switch Flush line to He Gas, close N2 gas bottle
- Open capillary valve and valve between Bath and TS (must be isobaric for liquid to flow through capillary)
- Monitor TS temperature carefully as it cools to no lower than about 90 K, close capillary at 90 K
- Let TS equilibrate at 90 K for several minutes, reopening the capillary as needed to keep temperature at 90 K

B.5 Liquid Helium Transfer

System Status: TS at 90 K with N₂ gas, Bath partially full of LN₂ at 77 K.

Goal: TS and Bath full of liquid He at 4.2 K.

- Prepare for Helium transfer: get transfer line ready, clear any obstacles, set Helium Dewar on forklift and tie down, attach (clear plastic) He gas line to pressurize Dewar and open ball valve. Verify He gas is ready to pressure Dewar
- Eject LN₂ (Wearing safety glasses & gloves!): Pressurize TS and Bath with He gas (at quite high pressure), block Bath blow off valve with glove, quickly insert L-Tube into Bath and eject all LN₂
- As soon as no more LN₂ is flowing out, remove L-Tube, cap Bath port, stop He flush asap to keep system as cold as possible
- Complete several ‘fill and flush’ cycles with He Gas to remove all N₂ gas and liquid¹
- When all N₂ is removed system is ready for liquid Helium transfer
- Stream He gas to both TS and Bath, insert one end of transfer line into Bath port and the other into the Dewar. This usually takes two people.
- Ensure the brass gasket seals the transfer line on the Dewar side
- Keep the transfer line level, inserting it to the bottom of the Bath then raising a half-inch to keep the flow unobstructed
- Lift the He Dewar with the forklift as needed to keep the transfer line level and inserted deep enough into the Dewar
- Pressurize the Dewar with He Gas as needed to maintain a reasonable flow rate out the Bath exhaust valve. Do not over pressurize the Dewar or transfer too quickly.
- **Maintain higher pressure in the Dewar than the cryostat Bath** always, or else Helium will flow back into Dewar
- When TS temperature starts falling (approximately when liquid in the Bath) close OVC valve and shut down turbo pump, after at least 10 minutes also shut down OVC rough pump
- Keep capillary valve open and fill until you see the He free surface rise above the TS windows. Keep TS and Bath isobaric by opening KF ball valve between them.

¹If there is residual LN₂ left anywhere you will not be able to pump it below a few Torr, if this happens consider heating the L-Tube and reinserting (while streaming He gas out to prevent any atmosphere from getting in) to boil residual LN₂ in Bath.

- After free surface rises above TS windows, close capillary then and continue to fill Bath until slight spray seen out bath exhaust valve. The transfer should take 20-40 minutes, not any less.
- **Continuously** Monitor the cryostat by checking OVC pressure and if the jacket feels cold - it should remain at room temperature. If OVC loses vacuum or cryostat suddenly gets cold, abort immediately, open all valves including KF90 on TS and evacuate lab.
- When TS and Bath full of liquid He and at 4.2 K, remove transfer line and cap bath port
- Remove Helium gas line for pressuring Dewar, close the line ball valve, move Dewar away from working area

B.6 Cool to Below T_λ

System Status: TS and Bath at 4.2 K, transfer line removed.

Goal: TS Below 2.172 K.

- Slowly open Pneumatic Valve and pump on both Bath and TS, cooling at 1-10 mK / sec
- Keep capillary open until near 2.172 K, then close capillary and stop pumping on Bath
- Continue pumping on TS and cool below 2.172 K
- When ready, open laser shutter, sonicate to release particles and record movies
- Replenish He from Bath by opening capillary valve as needed. When particles start to get 'shaky' the free surface is probably right above the windows and refilling from the Bath is necessary

B.7 Shutdown Procedure

System Status: Done taking data, no liquid Helium left in TS or Bath.

- Close pneumatic valve and shut of TS pump
- Shutdown laser
- If system must be back to room temperature the following day (for starting another run or doing repairs): Open valves between TS and bath. Flush with clean Helium gas to above 1 atm. Remove bath blowoff valve to ensure system is isobaric with lab. Open TS KF90 port and remove TS insert, leave open to lab to heat faster. Keep OVC valve closed and turbo and rough pumps off.

- If planning to run the next day starting with system as cold as possible (i.e. not opening the TS to the lab before running again): Open valves between TS and bath. Restart the OVC roughing pump, pump down line, open OVC valve, wait for OVC pressure < 100 mTorr, start turbo pump, pump OVC to 0.0 mTorr reading. Keep valve between bath and TS open and pneumatic valve closed, do not open KF90 TS port. If system is below 150 K upon return, one can resume the run starting with a He gas fill and flush (to remove any leaked atmosphere) and then proceed directly to the liquid Helium fill.
- Close all gas bottles
- Shut down cameras
- Back up movie files, shut down camera computers
- Back up temperature and time stamp log files: ArduinoLog.txt, TempLog.txt, counterFlowLog.txt
- Unplug Arduino, 24 VDC power supply, ultrasound amplifier power
- Shut down counterflow heater (Agilent), counterflow volt meter (Fluke 45), cell thermister Lockin (SR830)

Chapter C: Experiment Control Software

Following are all the source codes for running the experiment. These codes were developed to replace the previous apparatus control software running in MATLAB. This collection of python codes run on a control PC and interface with an Arduino. The Arduino is controlled by a hand-held controller with buttons and a potentiometer to control the ultrasound amplifier/transducer, trigger the movie cameras to start synchronously, open the solenoid flush valve for gas injection, and adjust the variable pneumatic-air controlled valve on the test section and bath. Schematics of the electronics are provided in Appendix D.

C.1 Arduino Code

Filename: Rig_Arduino_Code.ino

/ By David P Meichle 7/10/2014*

Combined camera trigger and Ultrasound S.S.R. controller arduino code for Helium experiment.

Ultrasound Solid-State Relay can be activated by three pushbuttons for short, medium and long sonications. After sonicating the program holds for a delay specified by RESETDELAY to avoid accepting a new US trigger. Note, when the Arduino boots the TTL level is not known, therefore for safety there should be a manual disable/enable switch which holds the SSR control to Ground until after the Arduino has booted.

The camera trigger sends a TTL low to signal the simultaneous start of a movie to the three Thorlabs 340GE-M cameras. The cameras should be set in 'trigger each' mode.

Note about Camera trigger: in 'trigger each' mode the trigger is blocked during readout to the PC. This takes about 5 ms with 2 Tap readout (its about 10 with 1 Tap readout), and can be seen on the Aux connector Pin 12 FVAL_OUT. Stable trigger-each operation worked with a 16ms or longer period square wave, but not faster as the trigger is ignored during readout. At 100 fps with 10msec exposure trigger-first mode has a jitter of about 2ms on each frame, and a cumulative offset around 10-20 ms (ie 1-2 frames) per 1000 images. I reccomend trigger-first mode for movies less than several thousand frames. For many minute long movies, it would be best to use trigger each with a framrate of 62.5 fps (1/16ms) or lower. timing_analysis.py has some useful python code. Goodluck. DPM

```

*/

//camera output pins
const int CAMERA = 8;

//camera input pins
const int GOBUTTON = 9;

//camera globals
const int TRIGGERPULSE = 100; //trigger-first pulse length in ms
int goButtonState = 0;

// ultrasound input pins
//short Sonication pushbutton pin (orange)
const int shortPin = 2;
//medium Sonication pushbutton pin (yellow)
const int mediumPin = 3;
//long Sonication pushbutton pin (blue)
const int longPin = 4;
//ultrasound SSR control voltage (red)
const int USPin = 5;

//PValve Pins
const int PValveOutPin = 10; //PWM Analouge Out pin
const int PValveReadPin = 0; //Analouge Read Pin

//PValve constants
const float VHigh = 5.0;
const float maxReadVoltage = 4.4; //should be about maxReadVoltage =
    VHigh*(RPot / (RPot + RLim));
const float VFullyClosed = 0.15;
unsigned long lastPValveStamp = 0; //milliseconds since writing last
    PValve to Serial
const unsigned long PVALVEINTERVAL = 500;
int PWMOut = 0;

// timing constants in ms
// ms for short sonication
const int SHORTSONICATION = 100;
// ms for short sonication
const int MEDIUMSONICATION = 500;
// ms for long sonication
const int LONGSONICATION = 1000;
// 1 sec delay after firing US
const int RESETDELAY = 100;

//ultrasound globals
// variable for reading the pushbutton status
int buttonState = 0;
//negative value indicates no button pressed
int theDelay = -1;
//pushbutton state variables
int shortState = 0;

```

```

int mediumState = 0;
int longState = 0;

void setup() {
    //initialize ultrasound pins
    pinMode(USPin, OUTPUT);
    pinMode(shortPin, INPUT);
    pinMode(mediumPin, INPUT);
    pinMode(longPin, INPUT);

    // initialize camera pins
    pinMode(CAMERA, OUTPUT);
    pinMode(GOBUTTON, INPUT);
    digitalWrite(CAMERA, HIGH); // High is hold for 340M-GE

    //initialize PValve Pins
    pinMode(PValveOutPin, OUTPUT);
    // pinMode(PValveReadPin, INPUT);

    //initialize serial communication
    Serial.begin(9600);
    Serial.println('Hello World!');
}

void triggerCamera() {
    Serial.print("MM");
    Serial.print("\r\n");
    digitalWrite(CAMERA, LOW); //send signal to begin movie
    delay(TRIGGERPULSE);
    digitalWrite(CAMERA, HIGH); // reset trigger
    delay(RESETDELAY);
}

void activateUltrasound(int duration) {
    Serial.print("US");
    Serial.print(duration, DEC);
    Serial.print("\r\n");
    digitalWrite(USPin, HIGH);
    delay(duration);
    digitalWrite(USPin, LOW);
    delay(RESETDELAY);
}

void pValveStamp()
{
    unsigned long now = millis();
    if( (now - lastPValveStamp) > PVALVEINTERVAL) {
        Serial.print("PV");
        Serial.print(PWMOut, DEC);
        Serial.print("\r\n");
        lastPValveStamp = now;
    }
}
}

```

```

void pValve() {
    int pValveIn = 0;
    float voltageIn = 0.0;
    float voltageOut = 0.0;

    pValveIn = analogRead(PValveReadPin); //integer ADC, reads from
    0-1023
    voltageIn = ((float)pValveIn / 1023.0) * (VHigh);
    voltageOut = (voltageIn - VFullyClosed)*(VHigh / (maxReadVoltage -
    VFullyClosed));
    PWMOut = (int)(255.0*voltageOut/VHigh);
    PWMOut = min( PWMOut, 255);
    PWMOut = max( PWMOut, 0 );

    analogWrite(PValveOutPin , PWMOut);
}

void loop() {

    //PWM Out for Pneumatic Valve Controller
    pValve();
    pValveStamp();

    //read camera button
    goButtonState = digitalRead(GOBUTTON);
    //read ultrasound buttons
    shortState = digitalRead(shortPin);
    mediumState = digitalRead(mediumPin);
    longState = digitalRead(longPin);

    //trigger camera if pressed
    if(goButtonState == HIGH) {
        triggerCamera();
        goButtonState = 0;
    }

    //activate ultrasound if pressed
    if(shortState == HIGH) {
        theDelay = SHORTSONICATION;
    } else if (mediumState == HIGH) {
        theDelay = MEDIUMSONICATION;
    } else if (longState == HIGH) {
        theDelay = LONGSONICATION;
    } else {
        theDelay = -1;
    }

    if( theDelay > 0 ) {
        activateUltrasound(theDelay);
        theDelay = -1;
    }
}

```

C.2 TimeStamp Logger

Filename: timeStampLogger.py

```
import serial as pys
import time
import datetime
import sys
import string

RS232_PAUSE = .05
ARDUINO_PORT = string.upper( sys.argv[1] )
arduino = pys.Serial(ARDUINO_PORT,baudrate=9600, timeout = .05);

today = datetime.datetime.now()
fileName = str(today)[:10] + '_ArduinoLog.txt'

f = open(fileName, "a")
print "Opened Log File", fileName
loopCounter = 0
while True:
    try:
        arduinoResponse = ""
        now = datetime.datetime.now()
        arduinoResponse = arduino.readline()
        while(arduinoResponse != ""):
            f.write( '{}, {}'.format(now, arduinoResponse))
            print datetime.datetime.now(), arduinoResponse
            now = datetime.datetime.now()
            arduinoResponse = arduino.readline()
        time.sleep(RS232_PAUSE)
    except KeyboardInterrupt:
        f.close()
        print '\n***\n***\n***'
        print 'Stopping TimeStampLogger'
        print '\n***\n***\n***'
        sys.exit()
```

C.3 Temperature Logger

Filename: tempLogger2.py

```
#lockin connected to StarTech USB-rs232 adapter, on StarTech plug 1
# REDONE FOR NEW THERMISTER IN TS 165-327 Ohms
import serial as pys
import numpy as np
import datetime
import time
import sys
import string
PRINT_TO_CONSOLE = 0
#approximate time (sec) between temperature reads.
# note read takes about 1 sec, so total wait is about INTERVAL + 1.0
seconds
INTERVAL = 0.25

#New thermister curves
tCal = np.array([1.19991873483008E+00,1.30007356739173E
+00,1.40043151153279E+00,1.59970265560516E+00,1.80000304298424E
+00,2.00006014064677E+00,2.19946078151283E+00,2.39983640650264E
+00,2.60007246388945E+00,2.80091602354104E+00,2.99948183731607E
+00,3.20014172513869E+00,3.40047052876845E+00,3.60094596615655E
+00,3.80133614194087E+00,4.00905207009381E+00,4.19547168239773E
+00,4.67012903369792E+00,5.07806285098528E+00,5.59080881320261E
+00,6.30622263561598E+00,1.52480127250625E+01,2.93448935092120E
+01,5.02864580458319E+01,7.52545548145316E+01,9.02346251325849E
+01,1.20203319267077E+02])
rCal = np.array([3.63219339929596E+02,3.44116603732669E
+02,3.27607960196617E+02,3.01011395887214E+02,2.8013259624092E
+02,2.63387395861894E+02,2.49634837358302E+02,2.37952923529789E
+02,2.27961980715978E+02,2.19294218615577E+02,2.11782643695261E
+02,2.05057354557073E+02,1.99051927163671E+02,1.93655640262620E
+02,1.88762163833946E+02,1.84138255922510E+02,1.80333260778425E
+02,1.71864419780933E+02,1.65649026311637E+02,1.58983024368616E
+02,1.51204371663796E+02,1.08002266945373E+02,8.46098891338343E
+01,6.78937930714879E+01,5.69023762253860E+01,5.23701797221295E
+01,4.56829753055278E+01])

#np.interp requires x values in increasing order, reverse both arrays:
tCal = tCal[::-1]
rCal = rCal[::-1]

#globals for estimaging dTemp/dTime
lastTemp = 100.0
lastTime = datetime.datetime.now()

def initializeSR830(lockin):
    #specify internal reference
    lockin.write('FMOD_1' + '\r')
    #set reference frequency 1000Hz
    lockin.write('FREQ_1000' + '\r')
    #specify sine reference (not TTL)
```

```

lockin.write('RSLP_0' + '\r')
#set reference voltage
lockin.write('SLVL_0.15' + '\r')
#set time constant to 1 sec
lockin.write('OFLT_10' + '\r')
#set phase to zero
lockin.write('PHAS_0' + '\r')
print('Done_Initializing_SR830_Lockin')

def kelvinFromVoltage(voltage):
    global lastTime
    global lastTemp
    #Assumes reference voltage of .15 VAC
    #Lockin measures voltage across 150kOhm resistor
    rThermister = float(voltage) * 149400.0 / ( 0.15 - float(voltage))
    #print 'ohms: ', rThermister
    #compute temperature by interpolating from calibration curves
    kelvin = np.interp(rThermister, rCal, tCal, left = 100)
    rightNow = datetime.datetime.now()
    elapsed = (rightNow - lastTime).total_seconds()
    Dtdt = (kelvin - lastTemp) / elapsed
    lastTemp = kelvin
    lastTime = rightNow
    print('_', kelvin, kelvin - 2.172, Dtdt*1000)
    return kelvin

def readTemp(lockin, logFileName):
    lockin.write('OUTP?_1' + '\r')
    #gives a string formatted like '2014-04-07 16:10:54.790000'
    now = str(datetime.datetime.now())
    voltage = lockin.readline() #reads voltage as a string
    voltage = voltage.rstrip() #removes '\r' from string
    kelvin = kelvinFromVoltage(voltage)
    f = open(logFileName, "a")
    f.write('{} , {} , {} \n'.format(now, voltage, kelvin))
    f.close()
    if PRINT_TO_CONSOLE:
        print '{} , {} , {}'.format(now, voltage, kelvin)

#create lockin object
theport = string.upper( sys.argv[1] )

lockin = pys.Serial(theport, baudrate=9600, bytesize=pys.EIGHTBITS,
    parity=pys.PARITY_NONE, stopbits=pys.STOPBITS.ONE, timeout=1)
try:
    lockin.close()
    lockin.open()
except:
    print 'FATAL_Error_opening_lockin_on_port:', theport
    sys.exit()

#set RS232 mode

```

```

lockin.write('OUTX\r' + '\r')
#query for identity
lockin.write('*IDN?' + '\r')
response = lockin.readline()
if response[:8] == 'Stanford':
    print('\nSUCCESSFULLY opened SR830 Confirmed *IDN? Query')
else:
    print('FATAL Did not return correct *IDN? response\n')
    print('FATAL Error opening lockin on port:', theport)
    print('Response Given:', response)
    sys.exit()

initializeSR830(lockin)
today = datetime.datetime.now()
fileName = str(today)[:10] + '_TempLog.txt'
print('Starting!')
print('Temperature log file:', fileName)

#RUN, catching Cntrl-C to close program
try:
    while True:
        readTemp(lockin, fileName)
        time.sleep(INTERVAL)
except KeyboardInterrupt:
    lockin.close()
    print('!!! Closing Program !!!')
    sys.exit()

```

C.4 CounterFlow Controller

Filename: counterflowController.py

```
import serial as pys
import string
import datetime
import time
import sys

RS232_PAUSE = .5

CF_Voltage = 1.0 #Default Counterflow Voltage
CF_Time = 1.0 #Default Counterflow Time
CF_CurrentLimit = 5.0 #Default (fixed) current limit 5 Amps
R_Ref = 1.97 #Reference Resistor 1.97 Ohms (measured with microOhm
meter 11/06/2014)
LINUX = 1
def checkPortStrings():
    if len(sys.argv) != 3:
        print 'Error must specify two ports for voltmeter and heater in
            argv[1] and argv[2]'
        sys.exit()
    voltmeterPort = string.upper( sys.argv[1] )
    heaterPort = string.upper( sys.argv[2] )
    if not LINUX:
        print "Assuming this is Windows"
        if voltmeterPort not in ['COM1', 'COM2', 'COM3', 'COM4', 'COM5', '
            COM6', 'COM7']:
            print 'Error must specify two ports for voltmeter and heater in
                argv[1] and argv[2]'
            sys.exit()
        if heaterPort not in ['COM1', 'COM2', 'COM3', 'COM4', 'COM5', 'COM6
            ', 'COM7']:
            print 'Error must specify two ports for voltmeter and heater in
                argv[1] and argv[2]'
            sys.exit()
    else:
        print "Assuming this is LINUX"
        #good to go, return port strings:
        return (voltmeterPort, heaterPort)

def setupHeater(heaterPort):
    heater = pys.Serial(heaterPort,baudrate=9600, bytesize=pys.EIGHTBITS,
        parity=pys.PARITY_NONE, stopbits=pys.STOPBITS_TWO, timeout=2)
    try:
        heater.close()
        heater.open()
        #heater.write('*IDN?' + '\r')
        #response = heater.read()
        #print "Heater *IDN? returns: ", response
        time.sleep(RS232_PAUSE)
        heater.write("*RST\n")
        time.sleep(RS232_PAUSE)
```

```

heater.write("Output_on\n")
time.sleep(RS232_PAUSE)
heater.write("APPL_3.1415,_0.0\n")
time.sleep(RS232_PAUSE)
heater.write("VOLT?\n")
time.sleep(RS232_PAUSE)
response = heater.readline()
time.sleep(RS232_PAUSE)
heater.write("APPL_0.0,_0.0\n")
if response[:7] == '+3.1415':
    print 'Powersupply successfully opened on port: ', heaterPort
else:
    print 'FATAL_Error, Powersupply on port: ', heaterPort, ' did not
        confirm test voltage 3.1415'
    sys.exit()
except:
    print 'FATAL_Error opening Heater on port: ', heaterPort
    sys.exit()

#completed heater setup and communication verification:
return heater

def setupVoltmeter(voltmeterPort):
    voltmeter = pys.Serial(voltmeterPort, baudrate=9600, bytesize=pys.
        EIGHTBITS, parity=pys.PARITY_NONE, stopbits=pys.STOPBITS.ONE,
        timeout=2)
    try:
        voltmeter.close()
        voltmeter.open()
        voltmeter.write('*IDN?\r\n')
        time.sleep(RS232_PAUSE)
        response = voltmeter.readline()
        if response[:5] != 'FLUKE':
            print 'FATAL_did_not_confirm_Voltmeter_*IDN?_on_port: ',
                voltmeterPort
            print 'Do_you_Have_Echo_Mode_Off?(check_Fluke_45_manual)'
            sys.exit()
    except:
        print 'FATAL_Error opening Voltmeter on port: ', voltmeterPort
        sys.exit()

    voltmeter.write('*RST\r\n')
    voltmeter.write('AUTO\r\n')

    inLine = voltmeter.readline()
    counter = 0
    while inLine == '=>\r\n' and counter < 10:
        inLine = voltmeter.readline()
        counter = counter + 1
    if counter >= 10:
        print 'FATAL_Failed_to_clear_voltmeter_outputbuffer_after:',
            counter, ' tries!'
        sys.exit()

```

```

print 'FLUKE_Voltmeter_Successfully_Opened_on_port: ', voltmeterPort
return voltmeter

def readVoltmeter(voltmeter):
    #read blank line to clear output buffer

    voltmeter.write('VAL?\r\n')
    time.sleep(RS232_PAUSE)

    inLine = voltmeter.readline()
    counter = 0
    while inLine == '=>\r\n' and counter < 10:
        inLine = voltmeter.readline()
        print inLine
        counter = counter + 1
    if counter >= 10:
        print 'FATAL_Failed_to_read_voltmeter_after: ', counter, ' tries!'
        inLine = '0.0'

    try:
        volts = str(float( inLine.rstrip() ))
        done = True
    except ValueError:
        print 'ERROR_Invalid_read_from_Voltmeter!'
        volts = 0.0

    return volts

def setHeater(heater, voltage, current):
    #Set heater voltage and current limit
    #Returns datetime object when time set
    #on Fail, returns 'FAIL'
    timeSet = 'FAIL'
    try:
        outString = 'APPL' + str(voltage) + ', ' + str(current) + '\n'
        heater.write(outString)
        timeSet = datetime.datetime.now()
        print 'Set_heater_voltage: ', voltage, ' and current limit: ',
            current
    except ValueError:
        print 'Error_converting_strings_voltage: ', voltage, ' and current:
            ', current
        print 'Did_NOT_set_heater_output_to_requested_values'
        print 'Setting_output_to_0.0V'
        heater.write("APPL_0.0,0.0\n")
        timeSet = 'FAIL'
    return timeSet

def doCounterFlow(heater, voltmeter, fileName):
    print 'Executing_Counterflow'
    print 'Duration: ', CF_Time, ' Voltage: ', CF_Voltage
    CFStart = setHeater(heater, CF_Voltage, CF_CurrentLimit)
    print 'CFStart: ', CFStart
    time.sleep(RS232_PAUSE)

```

```

volts = readVoltmeter(voltmeter)
print '└read└CF└shunt└voltage:└', volts
time.sleep(CF_Time)
CFStop = setHeater(heater, 0.0, CF_CurrentLimit)
#
#add error handling code if setHeater returns 'FAIL' here...
#
print '└CFStop:└', CFStop
print '└Stop└└Start', CFStop - CFStart

I = float(volts) / R_Ref
power = (float(CF_Voltage) - float(volts)) * I
print '└CF└Heater└Power└', power
print 'Counterflow└Completed'
print ''
print ''
f = open(fileName, 'a')
f.write('\n')
f.write('CFStart:└{ }\n'.format(str(CFStart)))
f.write('CFStop:└{ }\n'.format(str(CFStop)))
f.write('Applied└Voltage:└{ }\n'.format(CF_Voltage))
f.write('Measured└Shunt└Voltage:└{ }\n'.format(volts))
#note Shunt is 1.5 Ohms
f.write('Measured└CF└Power:└{ }\n'.format(power))
f.close()

if __name__ == "__main__":
    voltmeterPort, heaterPort = checkPortStrings()

    heater = setupHeater(heaterPort)
    voltmeter = setupVoltmeter(voltmeterPort)

    today = datetime.datetime.now()
    fileName = str(today)[:10] + '└CounterflowLog.txt'
    #main loop
    print ''
    print ''
    print '└└└Program└Running└'
    print '└└└Log└File:└', fileName
    print '└└└press└t└to└change└counterflow└duration'
    print '└└└press└v└to└change└counterflow└voltage└'
    print '└└└press└c└to└execute└counterflow'
    print '└└└pres└CTRL└C└to└close'
    print ''
    while True:
        try:
            userIn = raw_input()
            if string.upper(userIn) == 'T':
                newTime = raw_input('└Enter└New└Counterflow└Duration:└')
                CF_Time = (float(newTime))
                print 'Set└Counterflow└Duration:└', CF_Time, '└Counterflow└
                    Voltage:└', CF_Voltage
            elif string.upper(userIn) == 'V':
                newVoltage = raw_input('└└Enter└New└Counterflow└Voltage:└')

```

```

    CF_Voltage = str(float(newVoltage))
    print 'Set Counterflow Duration:', CF_Time, ' Counterflow _
        Voltage:', CF_Voltage
elif string.upper(userIn) == 'C':
    doCounterFlow(heater, voltmeter, fileName)

except KeyboardInterrupt:
    print 'Halting counterflow program, shutting heater off'
    heater.write("APPL_0.0, 0.0\n")
    heater.close()
    sys.exit()
except ValueError:
    print 'Error converting String, input ignored'

```

C.5 Bath Temperature

Filename: bathTemp.py

```
import sys
import numpy as np
#extended calibration curves:
tCal = np.array([1.696, 1.702, 1.707, 1.713, 1.718, 1.724, 1.729,
 1.735, 1.741, 1.746, 1.752, 1.758, 1.763, 1.769, 1.775, 1.781,
 1.787, 1.793, 1.7989, 1.800300002,1.825049996, 1.850149989,
 1.87529999, 1.899199963, 1.924499989, 1.949799955, 1.97359997,
 1.998400033, 2.024950027, 2.049649954, 2.075049996, 2.09920001,
 2.124599934, 2.148300052, 2.174200058, 2.20025003, 2.225999951,
 2.250150084, 2.276499987, 2.299299955, 2.399649978, 2.498350024,
 2.600000024, 2.700399995, 2.79974997, 2.898350000, 3.000050068,
 3.100150108, 3.20025003, 3.300049901, 3.401650071, 3.500050068,
 3.597750068, 3.706599951, 3.801400065, 3.898849964, 3.998700023,
 4.10014987, 4.199800014, 4.299749851, 4.399649858, 4.500849962,
 4.999499798, 5.497499943, 6.000200033, 6.501349926, 7.006900072,
 7.501100063, 7.999600172, 8.498399734, 8.999300003, 9.499549866,
 9.999300003, 15.00329971, 20.00139999, 25.0, 29.99835014,
 34.99995041, 40.00014877, 45.00105095, 49.99979973,
 55.00174904,60.00094986, 65.0014534, 70.00124741, 75.00090027,
 80.00219727, 85.0027504, 90.00284958, 95.00250244, 100.0016975,
 150.0240021, 200.0272446, 250.0323486,300.0477905])
rCal = np.array([8989, 8939, 8888, 8838, 8787, 8737, 8686, 8636, 8585,
8535, 8484, 8434, 8383, 8333, 8282, 8232, 8181, 8131, 8080,
8072.55998, 7862.677129, 7664.535781, 7473.027109, 7291.78334,
7119.815859, 6952.30832, 6794.911855, 6650.839531, 6503.725,
6354.258691, 6217.476191, 6087.396309, 5960.873809, 5843.206738,
5722.037949, 5609.416719, 5503.337129, 5396.935195, 5294.59502,
5197.700918, 4842.040098, 4532.586836, 4260.749922, 4019.612676,
3804.92917, 3611.965762, 3436.598633, 3279.08293, 3135.242705,
3002.996465, 2882.870586, 2771.296182, 2673.941113, 2569.893887,
2488.492051, 2407.517256, 2331.509541, 2259.982393, 2192.751523,
2130.458213, 2071.630635, 2016.927378, 1785.242959, 1605.918066,
1462.983594, 1346.336016, 1247.984604, 1167.28792, 1097.337813,
1036.367891, 983.2316699, 935.9788281, 894.0801343, 632.0136621,
500.5533069, 418.798894, 362.06172, 320.109989, 287.6628088,
261.7299915, 240.5499414, 222.8740015, 207.8785101, 194.9755261,
183.7570465, 173.8747992, 165.1155725, 157.2766211, 150.2006915,
143.7938147, 137.9665094, 99.19679352, 78.20579163, 65.09776489,
56.1993222] )

#np.interp requires x values in increasing order, reverse both arrays:
tCal = tCal[::-1]
rCal = rCal[::-1]

def kelvinFromOhms(rThermister):
    kelvin = np.interp(rThermister, rCal, tCal, left = 1000.0)
    return kelvin

ohms = float(sys.argv[1])
print kelvinFromOhms( ohms )
```

Chapter D: Circuit Diagrams

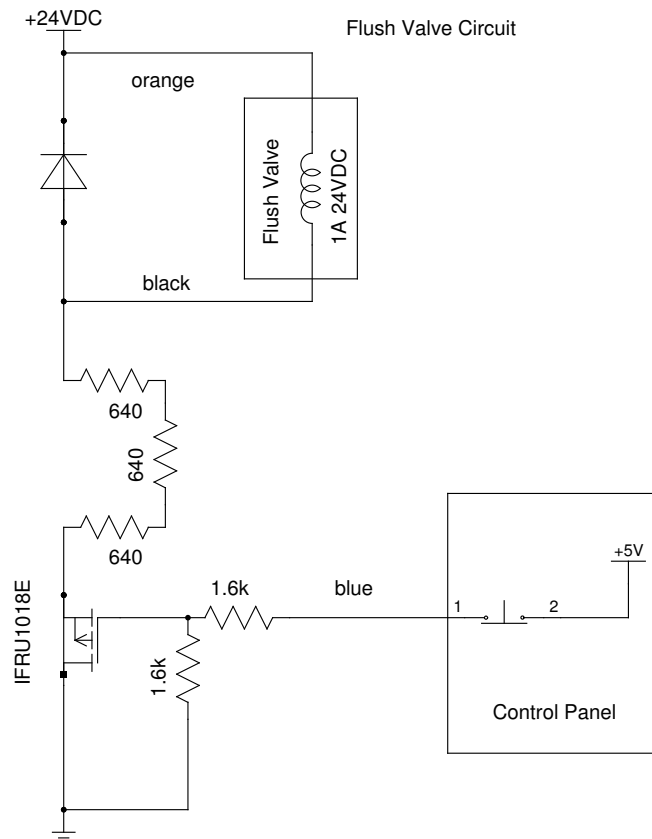


Figure D.1: Solenoid valve circuit diagram

Circuit diagram for solenoid valve controller. The solenoid coil requires about 1 Amp at 24 Volts to open. A button on the hand-held control panel provides manual control, activating a MOSFET transistor to provide the current for the Solenoid.

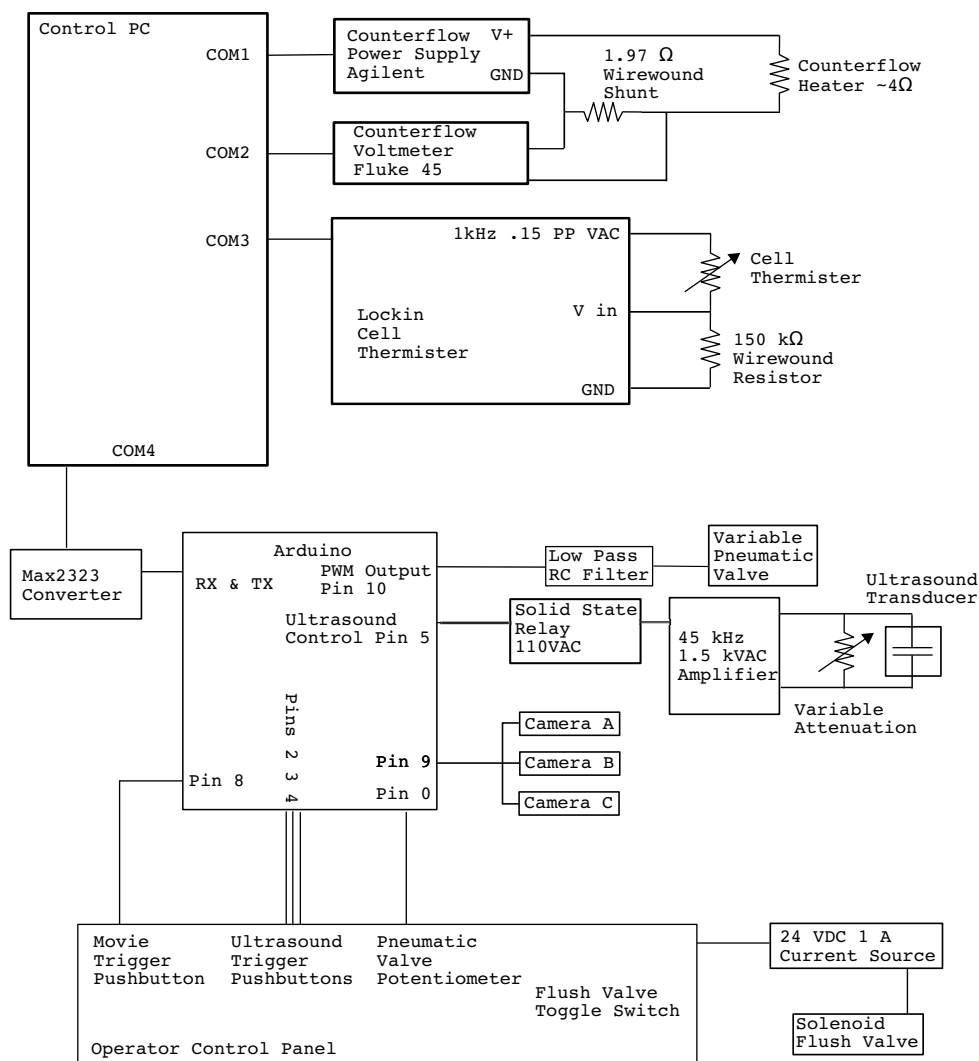


Figure D.2: Control electronics overview

Overview of all electronics controlling the experiment. Software written in Python which runs on a PC controls the counterflow heater and voltmeter, records and displays temperature measurements from the Lockin, and records timestamps of the movie triggers and ultrasound activations from the Arduino. The Arduino controls the ultrasound amplifier via a Solid State Relay, provides a variable voltage between 0 and 5VDC to the adjustable pneumatic valve via a low-pass filtered pulse width modulated output, and sends a trigger signal to all three cameras for synchronously starting the movies. Timestamps are communicated to the control PC and saved in a ASCII text files. The solenoid flush valve is controlled by a toggle switch on the operators' control panel. Details of the solenoid power circuit are given in Figure D.1.

Bibliography

- [1] W.H. Zurek. Cosmological experiments in superfluid helium? *Nature*, 317:505-508, 1985.
- [2] <http://hyperphysics.phy-astr.gsu.edu/hbase/lhel.html>, Georgia State University Dept. Physics & Astronomy.
- [3] <https://wiki.umn.edu/MXP/HelmholtzResonatorinSuperfluidHelium>, University of Minnesota Dept. of Physics.
- [4] J. R. Abo-Shaeer, C. Raman, J. M. Vogels, and W. Ketterle. *Science*, 292:5516, 2001.
- [5] Y. Shin, M. Saba, M. Vengalattore, T. A. Pasquini, C. Sanner, A. E. Leanhardt, M. Prentiss, D. E. Pritchard, and W. Ketterle. Dynamical Instability of a Doubly Quantized Vortex in a Bose-Einstein Condensate. *Phys. Rev. Lett.*, 93:160406, 2004.
- [6] E. Fonda, D.P. Meichle, N.T. Ouellette, S. Hormoz, and D.P. Lathrop. Direct observation of Kelvin waves excited by quantized vortex reconnection. *Proc. Natl. Acad. of Sci. USA*, 111 (Supplement 1):4707-4710, 2014.
- [7] D. Kleckner and W.T.M. Irvine. *Nature Phys.*, 9:253-258, 2013.
- [8] G.P. Bewley, M.S. Paoletti, K.R. Sreenivasan, and D.P. Lathrop. Characterization of reconnecting vortices in superfluid helium. *Proc. Natl. Acad. of Sci. USA*, 105 (37):13707-13710, 2007.
- [9] M. Paoletti, M. Fisher, K. Sreenivasan, and D.P. Lathrop. Velocity Statistics Distinguish Quantum Turbulence from Classical Turbulence. *Phys. Rev. Lett.*, 101.15:154501, 2008.

- [10] B. Svistunov. Superfluid turbulence in the low-temperature limit. *Phys. Rev. B*, 52:3647-3653, 1995.
- [11] P.C. Hendry, N.S. Lawson, R.A.M. Lee, P.V.E. McClintock, and C.D.H. Williams. Generation of defects in superfluid ^4He as an analogue of the formation of cosmic strings. *Nature*, 368:315-317, 1994.
- [12] M. Leadbeater, T. Winiecki, D. C. Samuels, C. F. Barenghi, and C. S. Adams. *Phys. Rev. Lett.*, 86:1410, 2001.
- [13] D. Kivotides, J. Vassilicos, D. Samuels, and C. Barenghi. Kelvin Waves Cascade in Superfluid Turbulence. *Phys. Rev. Lett.*, 86:3080-3083, 2001.
- [14] E.V. Kozik and B.V. Svistunov. Theory of Decay of Superfluid Turbulence in the Low-Temperature Limit. *J. Low Temp. Phys.*, 156:215-267, 2009.
- [15] V. L'vov, S. Nazarenko, and O. Rudenko. Bottleneck crossover between classical and quantum superfluid turbulence. *Phys. Rev. B*, 76:5-7, 2007.
- [16] C. Nore, M. Abid, and M. Brachet. Kolmogorov Turbulence in Low-Temperature Superflows. *Phys. Rev. Lett.*, 78:3896-3899, 1997.
- [17] M. Leadbeater, T. Winiecki, D. Samuels, C. Barenghi, and C. Adams. Sound Emission due to Superfluid Vortex Reconnections. *Phys. Rev. Lett.*, 86:1410-141, 2001.
- [18] W. Vinen, M. Tsubota, and A. Mitani. Kelvin-Wave Cascade on a Vortex in Superfluid He^4 at a Very Low Temperature. *Phys. Rev. Lett.*, 91:1-4, 2003.
- [19] K. Schwarz. Three-dimensional vortex dynamics in superfluid ^4He : Line-line and line-boundary interactions. *Phys. Rev. B.*, 31:5782-5804, 1985.
- [20] T. Lipniacki. Shape-preserving solutions for quantum vortex motion under localized induction approximation. *Phys. Fluids*, 15:1381-1395, 2003.
- [21] S. Gutiérrez, J. Rivas, and L. Vega. Formation of Singularities and Self-Similar Vortex Motion Under the Localized Induction Approximation. *Comm. Part. Diff. Eq.*, 28:927-968, 2003.
- [22] H. E. Hall and W. F. Vinen. The rotation of liquid helium II. The theory of mutual friction in uniformly rotating helium II. *Proc. R. Soc. of London. Series A: Math. and Phys. Sci.*, 238.1213:215-234, 1956.

- [23] D. Meichle, and D.P. Lathrop. Nanoparticle Dispersion in Superfluid Helium. *Rev. Sci. Inst.*, 85:073705, 2014.
- [24] D.P. Meichle, C. Rorai, M.E. Fisher, and D.P. Lathrop. Quantized Vortex Reconnection: Fixed points and initial conditions. *Phys. Rev. B*, 86.1:014509, 2012.
- [25] A.D. Waele and R. Aarts. Route to Vortex Reconnection. *Phys. Rev. Lett.*, 72:482-485, 1994.
- [26] R. Tebbs, A.J. Youd, and C. Barenghi. *J. Low Temp. Phys.* 162:314, 2011.
- [27] F. Dalfovo and S. Stringari. *Phys. Rev. A.*, 53:2477, 1996.
- [28] L. Lehtovaara, J. Toivanen, and J. Eloranta. Solution of time-independent Schrödinger equation by the imaginary time propagation method. *J. Comp. Phys.*, 221.1:148-157, 2007.
- [29] V.L. Ginzburg and L.P. Pitaevskii. *Sov. Phys. JETP*, 7:858, 1958.
- [30] C.A. Jones and P.H. Roberts. *J. Phys. A: Math. Gen.*, 15:2599, 1982.
- [31] J. Koplik and H. Levine. Vortex reconnection in superfluid helium. *Phys. Rev. Lett.*, 71:13751378, 1993.
- [32] J. Koplik and H. Levine. *Phys. Rev. Lett.*, 76:4745, 1996.
- [33] I.A. Ivonin. *Sov. Phys. JETP*, 85:1233, 1997.
- [34] S. Ogawa, M. Tsubota, and Y. Hattori. *J. Phys. Soc. Jpn.*, 71:813, 2002.
- [35] N.G. Berloff. *J. Phys. A: Math. Gen.*, 37:1617, 2004.
- [36] R.M. Kerr, *Phys. Rev. Lett.*, 106:224501, 2011.
- [37] S. Nazarenko and R. West. Analytical solution for nonlinear Schrödinger vortex reconnection, *J. Low Temp. Phys.*, 132:1-10, 2003.
- [38] M.V. Berry and M.R. Dennis, *Eur. J. Phys.*, 33:723, 2012.
- [39] M.V. Berry and M.R. Dennis, *J. Phys. A: Math. Theor.*, 40:65-74, 2007.
- [40] J. Adachi and G. Ishikawa, *Nonlinearity*, 20:1907, 2007.

- [41] G.P. Bewley, D.P. Lathrop, and K.R. Sreenivasan. Superfluid Helium: Visualization of quantized vortices. *Nature*, 441 (7093):588-588, 2006.
- [42] M. Paoletti, R. Fiorito, K.R. Sreenivasan, and D.P. Lathrop. Visualization of Superfluid Helium Flow. *J. Phys. Soci. Japan.*, 77/11, 2008.
- [43] G.P. Bewley, K.R. Sreenivasan, and D.P. Lathrop. Particles for tracing turbulent liquid helium. *Exp. Fluids.*, 44 (6):887-896, 2008.
- [44] M.S. Paoletti, M.E. Fisher, and D.P. Lathrop. Reconnection dynamics for quantized vortices. *Physica D*, 239 (14):1367-1377, 2010.
- [45] R. Feynman. *Progress in Low Temperature Physics*, ed. C.J. Gorter. (Amsterdam: North-Holland), pp17-53, 1955.
- [46] M. La Mantia, T. V. Chagovets, M. Rotter, and L. Skrbek. Testing the performance of a cryogenic visualization system on thermal counterflow by using hydrogen and deuterium solid tracers. *Rev. Sci. Inst.*, 83:055109, 2012.
- [47] M. La Mantia, D. Duda, M. Rotter, and L. Skrbek. Lagrangian accelerations of particles in superfluid turbulence. *J. of Fluid Mech.*, R9:717, 2013.
- [48] T.V. Chagovets, and S.W. Van Sciver. Visualization of He II counterflow around a cylinder. *Phys. Fluids*, 25.10:105104, 2013.
- [49] D. Grier, J.C. Crocker, and E.R. Weeks. <http://www.physics.emory.edu/weeks/idl/index.html>
- [50] T.V. Chagovets, and S.W. Van Sciver. A study of thermal counterflow using particle tracking velocimetry. *Phys. of Fluids*, 23.10:107102, 2011.
- [51] Y. Mineda, M. Tsubota, Y.A. Sergeev, C.F. Barenghi, and W.F. Vinen. Velocity Distributions of Tracer Particles in Thermal Counterflow in Superfluid ^4He . *Phys. Rev. B*, 87:174508, 2013.
- [52] C.F. Barenghi, Y.A. Sergeev. Motion of vortex ring with tracer particles in superfluid helium. *Phys. Rev. B*, 80.2:024514, 2009.
- [53] The Observed Properties of Liquid Helium at the Saturated Vapor Pressure. R.J. Donnelly and C.F. Barenghi. <http://pages.uoregon.edu/rjd/vapor1.html>
- [54] C.F. Barenghi, R. J. Donnelly, and W. F. Vinen. Friction on quantized vortices in helium II. A review. *J. Low Temp. Phys.* 52(3-4):189-247, 1983.

- [55] P.E. Parks and R. J. Donnelly. Radii of Positive and Negative Ions in Helium II. *Phys. Rev. Lett.*, 16(2):45, 1966.
- [56] G.P. Bewley and J. Vollmer. The journey of hydrogen to quantized vortex cores. *Physica Scripta*, 2013:014055, 2013.
- [57] D. Mateo, E. Jussi, G.A. Williams. Interaction of ions, atoms, and small molecules with quantized vortex lines in superfluid ^4He . *J. Chem. Phys.*, 142:064510, 2015.
- [58] G.P. Bewley, Ph.D. Thesis Ch 6, Yale University, 2006.
- [59] W. Thomson. Vibrations of a columnar vortex. *Phil. Mag.*, 10:155-168, 1880.
- [60] S.C. Crow. Stability theory for a pair of trailing vortices. *AIAA. J.*, 8:2172-2179, 1970.
- [61] T. Maxworthy. A Vorticity Source for Large-Scale Dust Devils and Other Comments on Naturally Occurring Columnar Vortices. *J. Atmos. Sci.*, 30:1717-1722, 1973.
- [62] R.I. Epstein, and G. Baym. Vortex drag and the spin-up time scale for pulsar glitches. *Astrophys. J.*, 387:276, 1992.
- [63] R.A. Helliwell. *Whistlers and Related Ionospheric Phenomena*. (Dover Publications), 2006.
- [64] T. Maxworthy, E.J. Hopfinger, and L.G. Redekopp. Wave motions on vortex cores. *J. Fluid Mech.*, 151:141, 1985.
- [65] E.J. Hopfinger and F.K. Browand. Vortex solitary waves in a rotating, turbulent flow. *Nature*, 295:393-395, 1982.
- [66] D. Kleckner and W.T.M. Irvine. Creation and dynamics of knotted vortices. *Nature Phys.*, 9:1-7, 2013.
- [67] R.J. Donnelly. *Quantized vortices in helium II*. (Cambridge University Press), 1991.
- [68] E. Sonin. Vortex oscillations and hydrodynamics of rotating superfluids. *Rev. Mod. Phys.*, 59:87-155, 1987.

- [69] H.E. Hall. An Experimental and Theoretical Study of Torsional Oscillations in Uniformly Rotating Liquid Helium II. *Proc. Roy. Soc. A*, 245:546-561, 1958.
- [70] E. Raja Gopal. Oscillations of quantized vortices in rotating liquid helium II. *Ann. Phys.*, 29:350-365, 1964.
- [71] R. Ashton and W. Glaberson. Vortex Waves in Superfluid ^4He . *Phys. Rev. Lett.*, 42:1062-1064, 1979.
- [72] V. Bretin, P. Rosenbusch, F. Chevy, G. Shlyapnikov, and J Dalibard. Quadrupole Oscillation of a Single-Vortex Bose-Einstein Condensate: Evidence for Kelvin Modes. *Phys. Rev. Lett.*, 90:1-4, 2003.
- [73] G.P. Bewley, K.R. Sreenivasan, and D.P. Lathrop. Superfluid helium: visualization of quantized vortices. *Nature*, 441:588, 2006.
- [74] M.S. Paoletti, M.E. Fisher, and D.P. Lathrop. Reconnection dynamics for quantized vortices. *Physica D* 239:1367-1377, 2009.
- [75] T. Lipniacki. Evolution of quantum vortices following reconnection. *Eur. J. Mech. B Fluid*, 19:361-378, 2000.
- [76] G.P. Bewley, M.S. Paoletti, K.R. Sreenivasan, and D.P. Lathrop. Characterization of reconnecting vortices in superfluid helium. *Proc. Natl. Acad. of Sci. USA*, 105:13707-10, 2008.
- [77] H.C. Pocklington. The Complete System of the Periods of a Hollow Vortex Ring, *Phil. Trans. R. Soc. London A*, 186:603, 1895.
- [78] R.J. Arms, F.R. Hama. Localized-Induction Concept on a Curved Vortex and Motion of an Elliptic Vortex Ring. *Phys. Fluids*, 8:553, 1965
- [79] R.L. Ricca. Rediscovery of Da Rios equations. *Nature*, 352:561-562, 1991.
- [80] L.S. Rios. Sul moto d'un liquido indefinito con un filetto vorticoso di forma qualunque. *Rendiconti del Circolo Matematico di Palermo*, 22:117-135, 1906.
- [81] G. Krstulovic. Kelvin-wave cascade and dissipation in low-temperature superfluid vortices. *Phys. Rev. E*, 86:055301, 2012.
- [82] D. Proment, C.F. Barenghi, and M. Onorato. Interaction and decay of Kelvin waves in the Gross-Pitaevskii model. *ArXiv*, 1308.0852, 2013.

- [83] C.F. Barenghi, R.J. Donnelly, and W.F. Vinen. Friction on quantized vortices in helium II. A review. *J. Low. Temp Phys.*, 52:189-247, 1983.
- [84] S. Hormoz, and M.P. Brenner. Absence of singular stretching of interacting vortex filaments. *J. Fluid Mech.*, 707:191-204, 2012.
- [85] H. Adachi, and M. Tsubota. Numerical Studies of Counterflow Turbulence. *J. Low. Temp Phys.*, 158:422-427, 2009.
- [86] L. Bou, D. Khomenko, V.S. L'vov, and I. Procaccia. Analytic solution of the approach of quantum vortices towards reconnection. *Phys. Rev. Lett.*, 111.14:145302, 2013.